



저작자표시-비영리-변경금지 2.0 대한민국

이용자는 아래의 조건을 따르는 경우에 한하여 자유롭게

- 이 저작물을 복제, 배포, 전송, 전시, 공연 및 방송할 수 있습니다.

다음과 같은 조건을 따라야 합니다:



저작자표시. 귀하는 원저작자를 표시하여야 합니다.



비영리. 귀하는 이 저작물을 영리 목적으로 이용할 수 없습니다.



변경금지. 귀하는 이 저작물을 개작, 변형 또는 가공할 수 없습니다.

- 귀하는, 이 저작물의 재이용이나 배포의 경우, 이 저작물에 적용된 이용허락조건을 명확하게 나타내어야 합니다.
- 저작권자로부터 별도의 허가를 받으면 이러한 조건들은 적용되지 않습니다.

저작권법에 따른 이용자의 권리는 위의 내용에 의하여 영향을 받지 않습니다.

이것은 [이용허락규약\(Legal Code\)](#)을 이해하기 쉽게 요약한 것입니다.

[Disclaimer](#)

M.S. THESIS

NANOELECTROKINETIC SELECTIVE
PRECONCENTRATION OF CHARGED
MOLECULES AND ITS DYNAMICS

전하를 띤 입자의 나노전기동역학적 선택적 농축 및
역학 관계

BY

JIHYE CHOI

FEBRUARY 2016

DEPARTMENT OF ELECTRICAL AND COMPUTER ENGINEERING
COLLEGE OF ENGINEERING
SEOUL NATIONAL UNIVERSITY

NANOELECTROKINETIC
SELECTIVE PRECONCENTRATION
OF CHARGED MOLECULES AND ITS
DYNAMICS

지도교수 김 성 재

이 논문을 공학석사 학위논문으로 제출함

2015 년 11 월

서울대학교 대학원

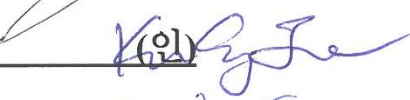
전기정보 공학부

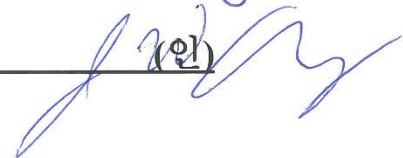
최 지 혜

최지혜의 공학석사 학위논문을 인준함

2016 년 2 월

위 원 장 이 종 호 (인) 

부위원장 김 성 재 (인) 

위 원 홍 종 욱 (인) 

Abstract

NANOELECTROKINETIC SELECTIVE PRECONCENTRATION OF CHARGED MOLECULES AND ITS DYNAMICS

JIHYE CHOI

DEPARTMENT OF ELECTRICAL AND
COMPUTER ENGINEERING

COLLEGE OF ENGINEERING

SEOUL NATIONAL UNIVERSITY

A multilayer micro/nanofluidic device was presented for the selective preconcentration and online collection of charged molecules with different physicochemical properties based on ion concentration polarization phenomena (ICP). With a balance of electroosmotic drag force and electrophoretic force on the molecules, a sample mixture of sulforhodamine B and Alexa Fluor 488 could be highly preconcentrated and separated simultaneously. A repeated microchamber structure was employed to capture each dye at a desirable position. For subsequent on-chip or off-chip application, pneumatic microvalves were integrated and selectively collected the target dyes with cyclic valve operations. Using the integrated system, Alexa Fluor 488 was solely collected (with a separation resolution of 1.75) out of the mixture at a 30-fold preconcentration ratio. Furthermore,

investigating the mechanism of preconcentration under ICP revealed that molecular interactions affected the location of preconcentrated plugs for satisfying local electroneutrality depending on their mobility. This integrated device would be a key component for lab on a chip applications.

Keywords : selective preconcentration, permselective membrane, ion concentration polarization, micro pneumatic valve, nanoelectrokinetics

Student Number : 2014-21644

Contents

Abstract	i
Contents	iii
List of Tables	v
List of Figures	vi
Chapter 1. Introduction	1
Chapter 2. Theoretical background	8
2.1 Characteristics of ICP phenomenon	8
2.2 Conventional models for ion concentration polarization	10
2.3 Simple model for preconcentration based on force balance	16
2.3.1 Preconcentration at the boundary of depletion zone	16
2.3.2 Simultaneous separation and preconcentration	19
Chapter 3. Selective preconcentration with micro pneumatic valve system	21
3.1 Experimental setup	21

3.1.1 Strategies for selective preconcentration and online collection	21
3.1.2 Preparation of PDMS microchips	26
3.1.3 Materials and reagents	29
3.1.4 System operation method	32
3.2 Results and discussions	34
3.2.1 Demonstration of selective preconcentration	34
3.2.2 Stabilization of selective preconcentration	37
3.2.3 Quantitative analysis for separation and preconcentration efficiency	37
3.2.4 Collection of preconcentrated plugs by valve system	40
3.2.5 Three kinds of analyte	46
3.2.6 Correlation between voltage configuration and separation time	52
3.2.7 Mobility-dependent preconcentration dynamics	57
Chapter 4. Conclusion and Future Work	63
Bibliography	65
Abstract in Korean	70

List of Tables

Table 3.1 Chemical and physical properties of Sulforhodamine B, Alexa Fluor 488, Alexa Fluor 532, and CoroNa Green.	22
Table 3.2 Separation time values of Alexa 488 from Alexa 532 in a repeated-chamber channel with different voltage configuration.	22

List of Figures

- Figure 1.1** (A) Capillary electrophoresis chip design¹ and (B) Schematic of on-chip Field-amplified sample stacking in the absence of Electroosmotic force. Gray shading is used to show conductivity field, with lighter shading corresponding to low-conductivity buffer.⁹.....22
- Figure 1.2** (A) Schematic of isotachopheresis and capillary electrophoresis assay protocol.² (B) Free-flow zone electrophoresis of fluorescein and rhodamine B. Potential was not applied in a) and 250 V cm⁻¹ across the separation area.¹⁰.....22
- Figure 1.3** (A) Fluorescence snapshots of DNA versus time. The fluorescence intensity increases with time, indicating concentration of the DNA sample. The exclusion zone moves away from the Nafion film interface (shown in dashed white lines) due to the dynamic equilibration process of ICP.⁵ (B) The phosphorylated substrates and the unphosphorylated substrates are simultaneously preconcentrated and separated.¹¹.....22
- Figure 1.4** (A) Schematic representation of the integrated nanofluidic biomolecule concentrator and microfluidic droplet generator chip. The enzyme molecules were accumulated by a concentrator into a plug that was mixed with the substrate and then encapsulated into monodisperse microdroplets for time-dependent observation. The reaction to turn over the fluorogenic substrate was monitored as a function of time in the

droplets.⁸ (B) Immunosensing using preconcentration under ion concentration polarization procedure. One can locally increase the sample concentration and facilitate the binding kinetics and the sensitivity without changing the binding pair or detection system.¹²...22

Figure 2.1 (A) Schematic configuration of micro-nano hybrid device for ion concentration polarization phenomenon and (B) Schematic diagram of ion concentration distribution near cation-selective membrane.....22

Figure 2.2 (A) The basic ion-enrichment and ion-depletion behavior and (B) characteristic curve of voltage against ionic current of a cation-exchange membrane, showing ohmic, limiting, and overlimiting regime⁶.....22

Figure 2.3 In situ measurement of local electric field inside an outside the ion depletion zone using microelectrodes integrated along the microchannel.⁴.....22

Figure 2.4 (A) The linear velocity and angular velocity of the vortex as a function of applied voltage. (B) Fast vortex at steady state in single gate device. (C) Four independent strong vortices in double gate device.⁶.....22

Figure 2.5 Schematic diagrams of the concentration profile inside ICP layer and ohmic/limiting/overlimiting current behavior when (A) only diffusion and drift were considered, (b) electroconvection was added to (A) and (C) multiple vortices were formed (inducing step-wise discrete concentration distribution).⁷.....22

Figure 2.6 The effect of bulk charge.³ (A) Calculated voltage against current curves for different values of parameter e where i_L is each limiting current. The zero value of e corresponds to the classical theory. (B) Calculated ion concentration profiles at different voltages V for $e = 10^{-4}$. Solid lines represents cation concentration at dimensionless voltage V while dashed lines do anion concentration.....22

Figure 2.7 (A) Preconcentration at the boundary of depletion zone and (B) schematic

of microchannel and nanojunction represented by resistors, where I denotes current, c denotes ion concentration, σ denotes conductance, and E denotes electric field.22

Figure 2.8 Schematic diagram of selective preconcentration mechanism with different mobility. The separation was drawn by the equilibrium between electroosmotic drag force and electrophoretic force exerted on molecules.22

Figure 3.1 Preconcentration operation in (A) straight microchannel, (B) funnel microchannel and (C) narrow microchannel.22

Figure 3.2 Numerically simulated ICP layer for (A) concentration distribution, (B) electrical field and (C) flow field. (D) Schematic illustration for electric potential near the microchamber.22

Figure 3.3 (A) Microscopic view of the selective preconcentration device. The microchannels in the ICP layer were indicated with blue and the microchannels in the valve layer were indicated red. (B) An exploded view of the device with (i) a valve layer, (ii) an ICP layer and (iii) a Nafion patterned slide glass. (C) Assembled multilayered online selective preconcentration device.22

Figure 3.4 Chemical structure of (A) Sulforhodamine B, (B) Alexa Fluor 488, (C) Alexa Fluor 532, and (D) CoroNa Green.22

Figure 3.5 Microscopic images of 3-step valve control sequence: Step1 - ICP preconcentration to form a highly concentration plug, Step 2 - isolation of a highly preconcentrated plug at specific microchamber, and Step 3 - collection of the highly preconcentrated plug into upward channel.22

Figure 3.6 Time-lapse images of selective preconcentration of SRB and Alexa 488. High Concentration ratio was represented by the brightness of fluorescence. Since the physicochemical properties of two dyes were different, they were preconcentrated at different locations.22

- Figure 3.7** Overall fluorescence intensity tracked in each microchamber as a function of time. Dotted line, dashed line and solid line represented the mixture of SRB with Alexa 488, only SRB and only Alexa 488, respectively. Three different colors indicated the pixel intensity of each microchamber (black for microchamber 1, red for microchamber 2 and blue for microchamber 3). The concentration ratio of selectively preconcentrated Alexa 488 in microchamber 3 exceeded 100-fold, maintaining the preconcentration factor high enough in repeated valve operations.22
- Figure 3.8** Red/green color profile in microchamber 3, showing the microchamber 3 only had Alexa 488.....22
- Figure 3.9** Red/green color profile in microchamber 1, showing the microchamber 1 only had SRB. Fluctuations after 30 minutes in all plots showed that the preconcentration factor maintains over 50-fold along the cyclic valve operations. While the error bars were omitted for clear visibility, the tests were conducted at least 10 times with different devices for the repeatability and reliability.....22
- Figure 3.10** Time-lapse images showing the dispersion of isolated plug when the valves were (A) OFF and (B) ON.22
- Figure 3.11** (A) Snapshots of repeated valve operations collecting selectively preconcentrated plugs. Compared to the initial state, the measurement window was being filled with green dye (Alexa 488) over several valve operations. (B) Average intensity change in the measurement window over number of repetition of valve operations. The average intensity exceeded 10-fold in a single valve operation, and 30-fold after nine operations. Note that there was no SRB in the measurement window. 22
- Figure 3.12** Time-lapse images showing the selective preconcentration of SRB, Alexa 532 and Alexa 488. Three different dyes were simultaneously

preconcentrated and separated.	22
Figure 3.13 Green pixel intensity tracked in each microchamber as a function of time with the intensity reference line of Alexa 532. A triangular marker, a rectangular marker, and a diamond marker, and x marker represent the green pixel intensity in microchamber 2, microchamber 3, microchamber 4, and microchamber 5, respectively.	22
Figure 3.14 Red pixel intensity tracked in each microchamber as a function of time with the intensity reference line of SRB. A circular marker, a triangular marker, a rectangular marker, and a diamond marker represent the red pixel intensity in microchamber 1, microchamber 2, microchamber 3, and microchamber 4, respectively.	22
Figure 3.15 Green pixel intensity tracked in each microchamber as a function of time with the intensity reference line of Alexa 488. A triangular marker, a rectangular marker, and a diamond marker, and x marker represent the green pixel intensity in microchamber 2, microchamber 3, microchamber 4, and microchamber 5, respectively.	22
Figure 3.16 Time-lapse images of selective preconcentration of Alexa 488 and Alexa 532 with the voltage configuration of (A) V_{LOW} for 20 V, V_{HIGH} for 120 V, (B) V_{LOW} for 20 V, V_{HIGH} for 100 V and V_{LOW} for 30 V, V_{HIGH} for 110 V, respectively. The separation time of Alexa 488 from Alexa 532 takes longer in order of (A) to (C), respectively.	22
Figure 3.17 Operation map of the time for Alexa 532 to separate from Alexa 488 under each V_{LOW} and V_{HIGH} . There exists the maximum point and the minimum point.	22
Figure 3.18 (A) Schematic of device with straight channel. The length of main channel is ~6 mm. (B) Microscopic view of the device with straight channel.	22
Figure 3.19 (A) Time-lapse images of selective preconcentration of (A) SRB, (B)	

Alexa 532 and (C) SRB and Alexa 532 together as a function of time. The location of each plug along time scale in (C) differs from that of single kind plug in (A) and (B).22

Figure 3.20 Time-lapse images of selective preconcentration of (A) CoroNa Green and (B) CoroNa Green and SRB together as a function of time. The location of each plug along time scale in (C) differs from that of single kind plug in (A) and (B).22

Chapter 1

Introduction

Recently, the micro Total Analysis System (mTAS) has been tremendously researched in the fields of analytical chemistry, diagnosis, environmental and nuclear engineering.¹³ The major components in such systems are a separator for multi-component analytes, a preconcentrator for the detection of low abundant molecules, and a sample collector for post processing. These on-chip preconcentration methods have been developed in order to detecting low-abundant analytes, particularly those in bio-samples. Although off-chip sample can solve this this problem prior to analysis, the amount of sample loss and contamination in sample cannot be ignored. Furthermore, the additional preparation steps before analysis are often labor-intensive and time-consuming. In this light, many on-chip sample preconcentration techniques based on different working principles for improving the detection sensitivity have been introduced and implemented in microchips for achieving the goals of automation, enhancement in analytical efficiency, and reductions in sample loss and contamination.¹⁴

A number of researches have been performed on preconcentration or separation of molecules using capillary electrophoresis,¹ microfluidic field-amplified sample stacking,⁹ isoelectric focusing,¹⁰ and isotachopheresis² as shown in Figure 1.1 and

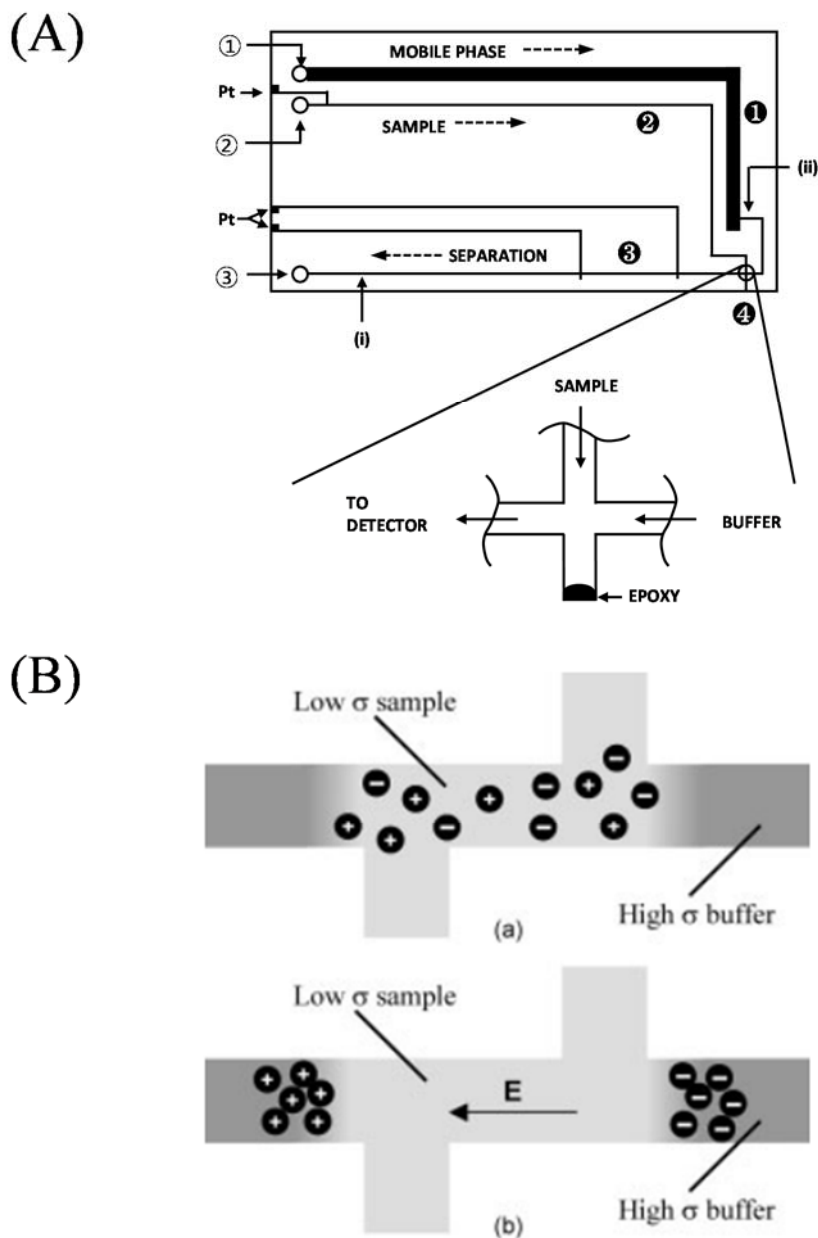


Figure 1.1 (A) Capillary electrophoresis chip design¹ and (B) Schematic of on-chip Field-amplified sample stacking in the absence of Electroosmotic force. Gray shading is used to show conductivity field, with lighter shading corresponding to low-conductivity buffer.⁹

Figure 1.2.² In practical processes, these methods have several difficulties; (1) these methods require the additional extraction system of pre-concentrated and separated molecules because they employ free flow concept (i.e. the target compounds are migrating and concentrating simultaneously along the specific path where the background fluid is flowing.), limiting subsequent processes. (2) Alternating injection of samples that should be isolated one another causes considerable cross contaminations. (3) While the reliability of detection level is enhanced by increasing the concentration of samples, intricate channel geometries or specific chemicals are often demanded for an experimental setting. (4) Even after successful separation and pre-concentration, online detection followed by these operations can still cause an inevitable dispersion. These problems tend to increase complexity of operations or produce false negative and false positive, resulting in unfeasible on-chip processes. Therefore, a new design with simple structure and easy fabrication is demanded for performing fast and accurate separation and pre-concentration. Furthermore, a connection to conventional off-chip analysis systems or an integration with on-chip analysis parts is expected for the ideal platform of mTAS.

As a method to pre-concentrate analytes, nanoscale electrokinetic phenomenon caused by the selective transportation of counter-ions in the electrolyte near a nanoporous membrane, called ion concentration polarization (ICP), has been suggested and the pre-concentration factor reached up to million-fold.¹⁵ The target analytes are concentrated at pinned position, while background fluid is still flowing in ICP operation. Recently, simultaneous separation and pre-concentration (or selective pre-concentration) was successfully performed using ICP, demonstrating the separation of phosphorylated and unphosphorylated substrates¹¹ or tagged and untagged DNA molecules as shown in Figure 1.3.⁵ It indirectly proved that one can utilize the ICP concept not only to pre-concentrate low abundant molecules but also to separate molecules depending on different physicochemical properties. However, these ICP demonstrations still have several limitations. (1) First of all, the

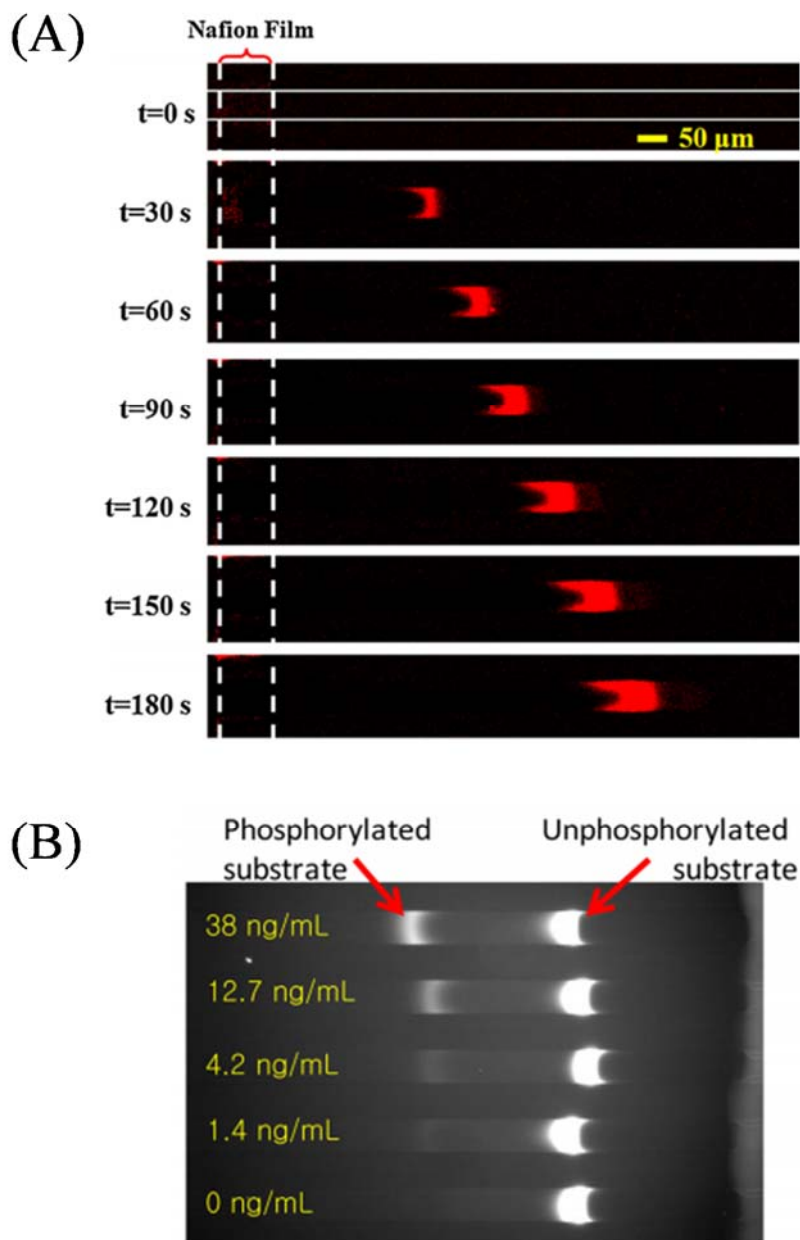


Figure 1.3 (A) Fluorescence snapshots of DNA versus time. The fluorescence intensity increases with time, indicating concentration of the DNA sample. The exclusion zone moves away from the Nafion film interface (shown in dashed white lines) due to the dynamic equilibration process of ICP.⁵ (B) The phosphorylated substrates and the unphosphorylated substrates are simultaneously preconcentrated and separated.¹¹

identification of the location where reactions occur becomes labor-intensive and time-consuming tasks since the location of preconcentrated sample plug keeps uncontrollably fluctuating by the strong instability of electrokinetic flow inside ICP layer.^{7, 16} (2) The extraction of the preconcentrated analytes for post processing without irresistible dispersion still has not been accomplished. Turning off an applied electric field let the highly preconcentrated plugs disperse quickly since there is a huge concentration gradient at the boundary. To resolve this problem, an integration with two-phase droplet generator⁸ or pre-binding on-site reaction¹² were reported as in Figure 1.4, but an additional recovery processes is needed or aggressive washing steps should be excluded, respectively. These factors significantly hinder the commercialization of further engineering developments.

To evolve ICP concept as a practical tool to selectively preconcentrate charged molecules, the integral mechanism is unprecedentedly required of (1) the stable formation of the highly preconcentrated single analyte and (2) on-demand extraction to external systems without undesirable dispersion. In this work, by designing narrow channels between repeated microchambers, the fluidic instability due to amplified electric field inside ICP was able to be suppressed. Limiting the ever-expanding ICP zone by microstructures¹⁷ or by external hydrodynamic flow injection¹⁸ have been reported to restrict the hydrodynamic instability and the role of vortices near the membrane.¹⁹ These narrow microchannels between repeated microchambers presented in this work are expected to perform in the same manner. Subsequently, pneumatic microvalve system²⁰ was employed to isolate the highly concentrated sample from the original sample mixture without further dispersion, and also to collect sample plugs so that they can be further used in conventional analytical systems in either on-chip or off- chip formats.

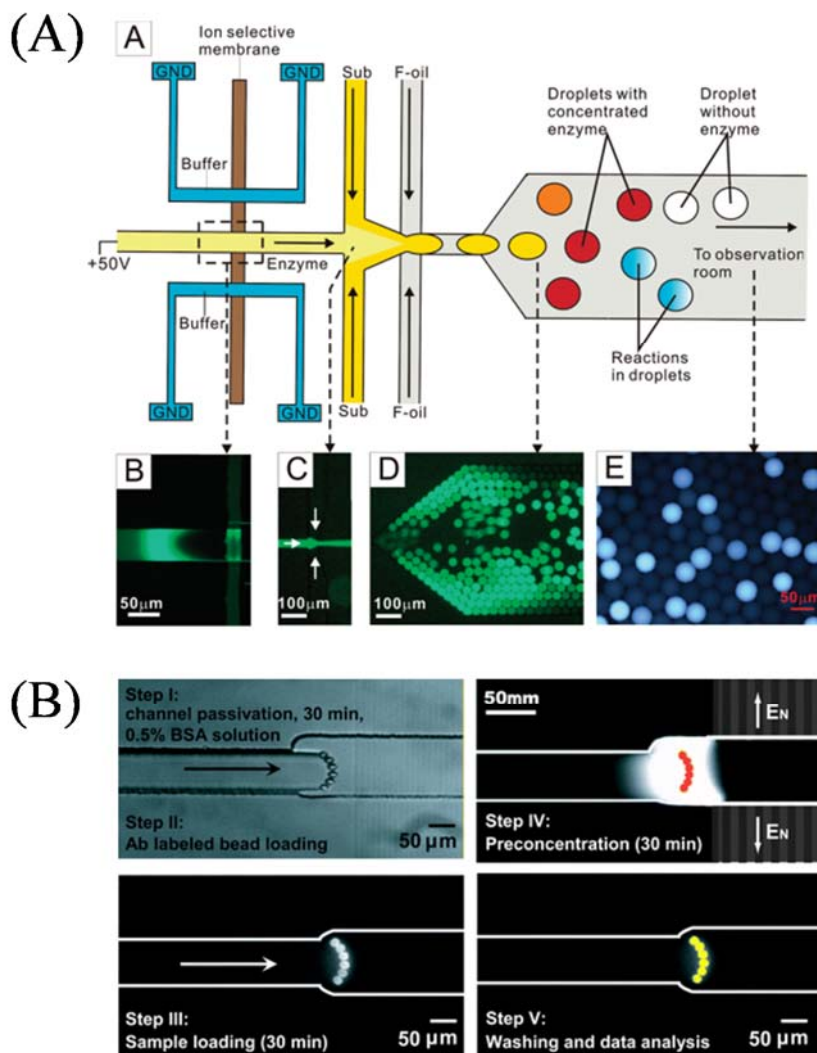


Figure 1.4 (A) Schematic representation of the integrated nanofluidic biomolecule concentrator and microfluidic droplet generator chip. The enzyme molecules were accumulated by a concentrator into a plug that was mixed with the substrate and then encapsulated into monodisperse microdroplets for time-dependent observation. The reaction to turn over the fluorogenic substrate was monitored as a function of time in the droplets.⁸ (B) Immunosensing using preconcentration under ion concentration polarization procedure. One can locally increase the sample concentration and facilitate the binding kinetics and the sensitivity without changing the binding pair or detection system.¹²

Chapter 2

Theoretical background

2.1 Characteristics of ICP phenomenon

When it comes to permselective system in ion concentration polarization phenomenon, micro-nano hybrid platform is considered as shown in Figure 2.1(A). In the platform, two microchannels are connected only with nanojunction which operates as a permselective membrane. In this work, only cation-selective membrane is discussed below under microchannel surface with negative zeta potential.

A nanochannel thinner than $O(100)$ nm has permselectivity since in that scale the thickness of Debye layer should be non-negligible and the layer even can be overlapped.²¹ As shown in Figure 2.1(B), only cations pass through cation-selective membrane towards cathodic side while anions cannot under electric field. Due to this preferential cation transport through the nanoporous membrane, ion concentration decreased in anodic side, which is called ion depletion zone, and ion concentration increased in cathodic side, which is called ion enrichment zone. The phenomenon of concentration polarization in either sides of permselective media is called as ion concentration polarization (ICP).^{6, 15} Kim *et al.* observed this phenomenon of nonlinear characteristics in current according to the applied voltage

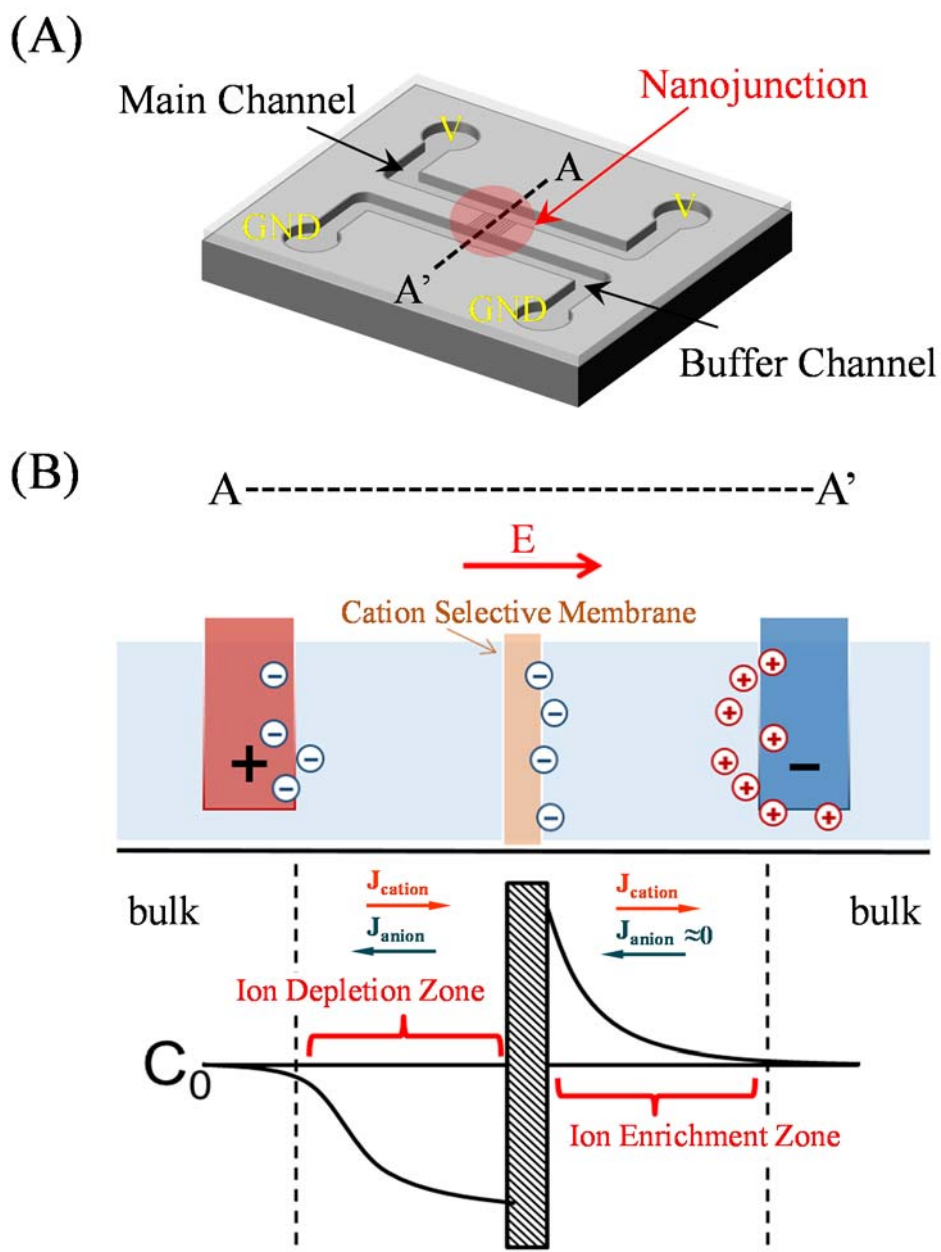


Figure 2.1 (A) Schematic configuration of micro-nano hybrid device for ion concentration polarization phenomenon and (B) Schematic diagram of ion concentration distribution near cation-selective membrane.

as shown in Figure 2.2(A) and (B). As applied voltage increases, there exists three regimes: ohmic regime in low current followed by limiting regime of a plateau with much lower slope, and overlimiting regime where the slope of current increased again but still lower than that of ohmic regime.⁶

The depletion zone, which is unique region adjacent to permselective membrane, has three distinctive properties: low ion concentrations,^{3,22} strengthened electric field intensity,⁴ and strong vortices^{6, 15, 22a} adjacent to the nanoporous membrane. As the cation selective membrane is impermeable for anions, only cations are permitted to pass through the membrane when voltage is applied. Locally broken electroneutrality in anodic side of the membrane lets anions repulse each other, forming depletion zone with ion concentration even below one hundredth of bulk concentration.^{3, 23} Due to depletion of ions as charge carriers, electrical conductivity in ion depletion zone becomes very small. Since current density should be uniform through the longitudinal direction along the microchannel, the magnitude of electric field happens to become extremely amplified. This was experimentally confirmed as denoted in Figure 2.3.⁴ In addition, strong and fast vortices are generated in depletion zone near the membrane.¹⁵ Rubinstein *et al.* theoretically suggested nonequilibrium electro-osmotic slip, at a flat permselective membrane, proportional to the square of electric field.^{22a} This relationship denotes the formation of vortices is nonlinear phenomenon. Figure 2.4(A) shows the velocity of the vortices which is at least $O(10)$ times faster than that of primary electroosmotic flow under the same electric potential. At steady state, Kim *et al.* observed fast vortices in each single and double gate device as shown in Figure 2.4(B).⁶

2.2 Conventional models for ion concentration polarization

As described in Figure 2.5(A),⁷ classical models based on Nernst-Planck equations considering ion transport only due to diffusion and electromigration predict the linear concentration profile inside the ion depletion zone.²⁴

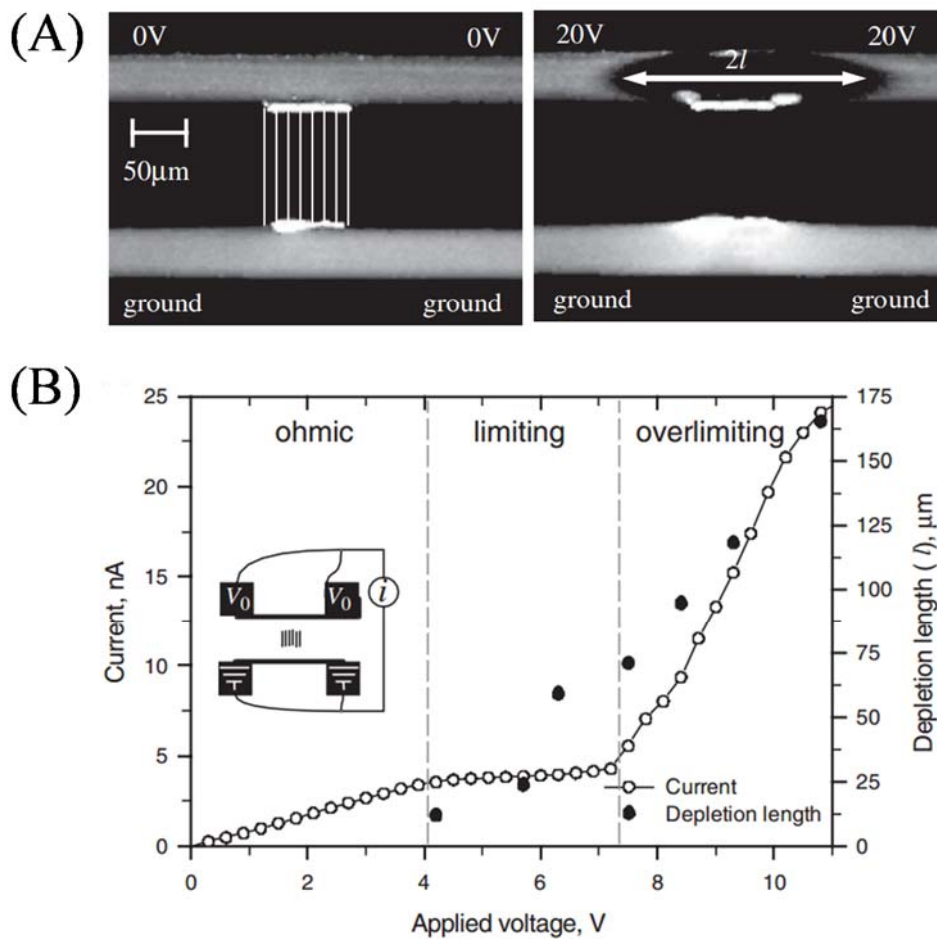


Figure 2.2 (A) The basic ion-enrichment and ion-depletion behavior and (B) characteristic curve of voltage against ionic current of a cation-exchange membrane, showing ohmic, limiting, and overlimiting regime⁶

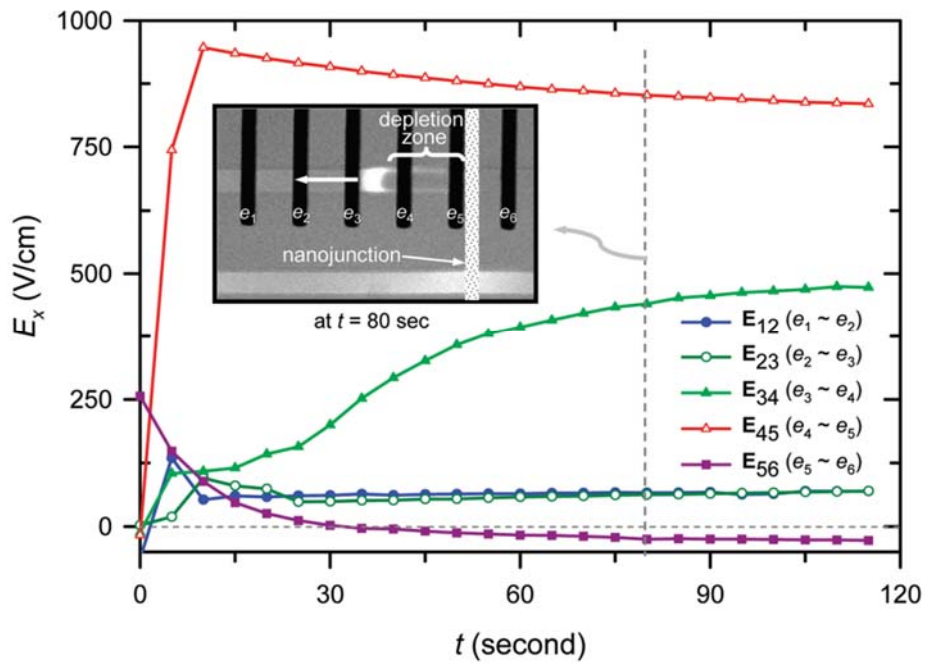


Figure 2.3 In situ measurement of local electric field inside and outside the ion depletion zone using microelectrodes integrated along the microchannel.⁴

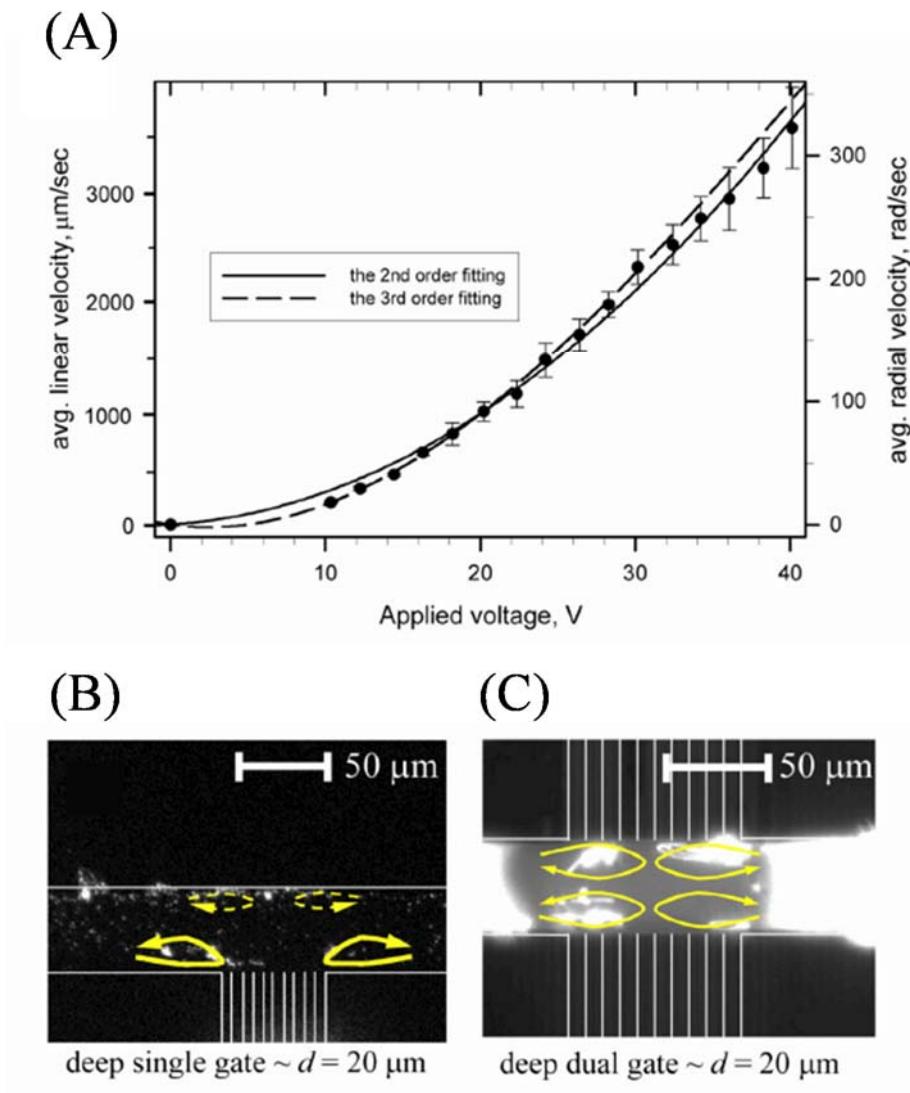


Figure 2.4 (A) The linear velocity and angular velocity of the vortex as a function of applied voltage. (B) Fast vortex at steady state in single gate device. (C) Four independent strong vortices in double gate device.⁶

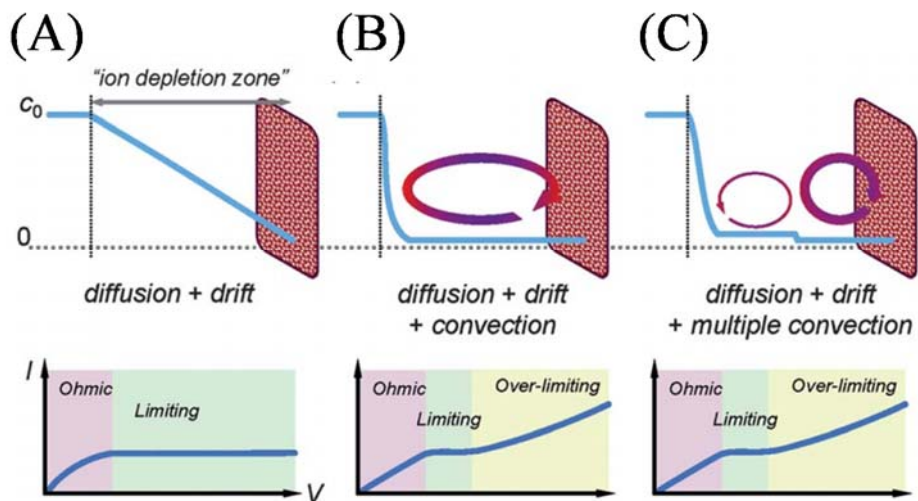


Figure 2.5 Schematic diagrams of the concentration profile inside ICP layer and ohmic/limiting/overlimiting current behavior when (A) only diffusion and drift were considered, (b) electroconvection was added to (A) and (C) multiple vortices were formed (inducing step-wise discrete concentration distribution).⁷

Tracing the connection with the classical model, Rubinstein *et al.*³ developed a model expressing overlimiting current as in Figure 2.5(B) by considering the role of bulk charge. A steady current was considered to pass through an ideally permselective membrane immersed in a stirred solution of 1:1 valent electrolyte. They assumed there is an ‘unstirred’ layer of thickness δ near the membrane, which does not depend on the magnitude of applied voltage V . Also, it was assumed that the ions within the unstirred layer are distributed by means of electrodiffusion only. Identifying the x-axis where $x = 0$ with the outer boundary of the ‘unstirred’ layer, governing equations and boundary conditions are as in the following.

$$\frac{d^2\psi}{dx^2} = -\frac{4\pi F}{\varepsilon} (c_+ - c_-) \quad (2.1)$$

$$\frac{d}{dx} \left(\frac{dc_+}{dx} + \frac{Fc_+}{RT} \frac{d\psi}{dx} \right) = 0 \quad (2.2)$$

$$\frac{d}{dx} \left(\frac{dc_-}{dx} - \frac{Fc_-}{RT} \frac{d\psi}{dx} \right) = 0 \quad (2.3)$$

$$\psi|_{x=0} = 0, \quad c_+|_{x=0} = c_-|_{x=0} = c_0 \quad (2.4)$$

$$\psi|_{x=\delta} = -V, \quad c_+|_{x=\delta} = N, \quad \left(\frac{dc_-}{dx} - \frac{Fc_-}{RT} \frac{d\psi}{dx} \right)|_{x=\delta} = 0 \quad (2.5)$$

where ψ is the electric potential, F is the Faraday constant, ε is the dielectric permittivity, c_+ and c_- is the ion concentration of each ionic species, R is the gas constant, c_0 is the bulk concentration, and N is the fixed charge concentration within the membrane. The Poisson equation is represented by equation (2.1). The Nernst-Planck equations (2.2) and (2.3) describe the mass transport of charged species under consideration of the diffusion and the electromigration. Since they assumed an ‘unstirred’ layer near the membrane, Stokes equations and continuity equation were not solved. Equation (2.4) represents the boundary condition of bulk reservoir and equation (2.5) represents the boundary condition near the cation selective membrane.

Due to the equations, the effect of bulk charge of ICP layer could be described in the overlimiting regime. In their definition, parameter δ is dimensionlessly defined by

$$\varepsilon = \frac{\lambda_D^2}{\delta^2} \quad (2.6)$$

where λ_D is the Debye length. In the Levich's model, ε is zero due to the assumption of local electroneutrality. With this zero value, ionic current becomes saturated to the limiting value as denoted in Figure 2.5(A). Considering the effect of bulk charge, ionic current could be increased beyond limiting current with different conductance comparing with ohmic regime as shown in Figure 2.6(A) and (B).

2.3 Simple model for preconcentration based on force balance

2.3.1 Preconcentration at the boundary of depletion zone

It has been known that nanofluidic channels can support ion-selective ion currents. When an electric field is applied across the nanojunction, the electrical double layer began to be overlapped in each nanojunction, letting counterions migrate across the nanojunction. This results in decrease of ion concentrations at the anodic side, generating the ion depletion zone. The ion depletion near the nanoporous membrane will thicken the Debye layer, and thus, make the layer overlap more significantly in the nanofluidic channel. This enhances ion concentration polarization. Above a certain threshold value of electric field, the ion transport across the nanojunction enters a new, nonlinear regime. In this regime, the counterions are depleted from the nanofluidic channel, and the extended space charge layer is formed near the nanojunction in the anodic bulk side. Within this induced layer, electroneutrality is locally broken and co-ions or other charged molecules are rejected to pass the depletion zone.²⁵ Meanwhile, electroosmotic flow generated by applying different voltage at each reservoir can extend the depletion zone to one side of the reservoir as shown in Figure 2.7(A). Due to electroosmotic flow, depletion zone is stretched to the reservoir with low voltage.

Negatively charged molecules are preconcentrated at the boundary of the depletion zone. As denoted in Figure 2.7(B), each part of the solution in the

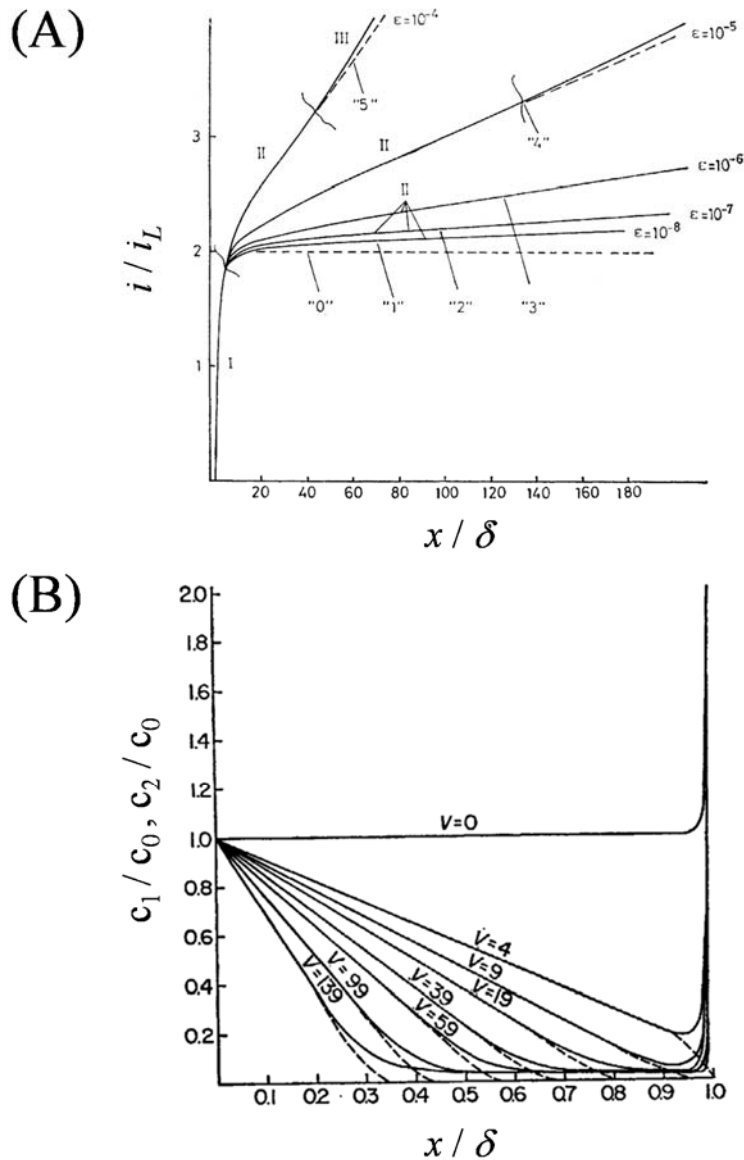


Figure 2.6 The effect of bulk charge.³ (A) Calculated voltage against current curves for different values of parameter ϵ where i_L is each limiting current. The zero value of ϵ corresponds to the classical theory. (B) Calculated ion concentration profiles at different voltages V for $\epsilon = 10^{-4}$. Solid lines represents cation concentration at dimensionless voltage V while dashed lines do anion concentration.

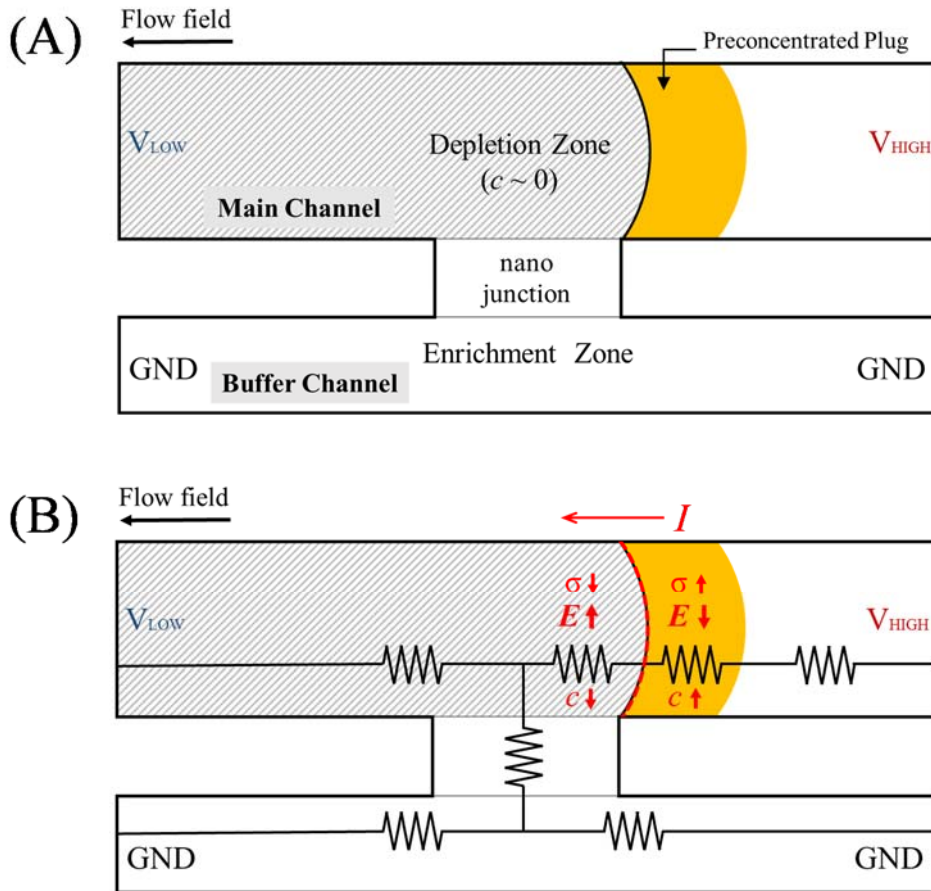


Figure 2.7 (A) Preconcentration at the boundary of depletion zone and (B) schematic of microchannel and nanojunction represented by resistors, where I denotes current, c denotes ion concentration, σ denotes conductance, and E denotes electric field.

microchannel and nanojunction can be interpreted as a connected resistor. Since current along the vicinity of the boundary of depletion zone should be uniform in a microchannel, different value of conductance leads different magnitude of electric field. Conductance is low on the depletion side of the boundary due to low concentration of electrolytes, and high on the other side of the boundary due to high concentration of electrolytes as that in the bulk side. This results in relatively higher magnitude of electric field in the depletion side of the boundary than that in the other side of the boundary. As far as negatively charged molecules are concerned, this electric barrier makes them preconcentrated at the vicinity of the boundary.

2.3.2 Strategies for selective preconcentration and online collection

In an environment with low Reynolds number, the flow in the microchannel is described as Stokes flow where inertia is ignored. Charged molecules in the microchannel are influenced by two different forces: electroosmotic force and electrophoretic force. Since the molecules are in the Stokes flow, electroosmotic force is equal to Stokes drag force, $6\pi\mu\mathbf{u}_{EO}R$, where μ is the dynamic viscosity, \mathbf{u}_{EO} is the electroosmotic velocity of bulk which is independent from molecule's properties, and R is the radius of the spherical object. Therefore, the electroosmotic force does not dominantly affect the separation of the preconcentrated molecules since the size of the molecules in this work is similar (~ 1 nm). On the other hand, electrophoretic force by electrostatic drift exerted on the molecules can be expressed as qE where q is a net electric charge and E is an electric field. Corresponding to the electrophoretic force, another drag force is formed with the magnitude of $6\pi\mu\mathbf{u}_{EPH}R$ where \mathbf{u}_{EPH} is the electrophoretic velocity, in the opposite direction of the electrophoretic force. Since the electrophoretic drag force and electrophoretic force by electrostatic drift should be the same, electrophoretic velocity, \mathbf{u}_{EPH} , is proportional to the net electric charge and electric field. Considering the electric field is almost the same along the area where molecules are preconcentrated, electric

charge places a key role in the separation of the molecules. As denoted in Figure 2.8, two different kinds of molecules have different equilibrium points due to their electrophoretic mobility. The molecules with higher electrophoretic mobility are preconcentrated towards the reservoir with high voltage while the preconcentrated molecules with low mobility stay near the nanojunction.

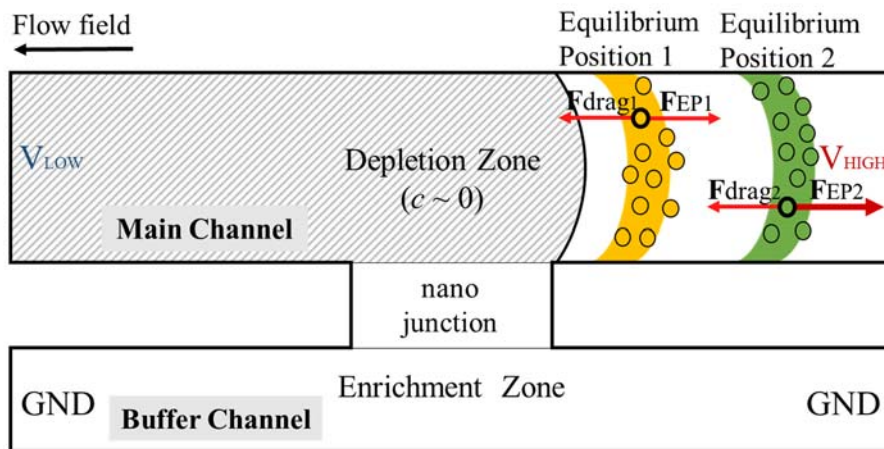


Figure 2.8 Schematic diagram of selective preconcentration mechanism with different mobility. The separation was drawn by the equilibrium between electroosmotic drag force and electrophoretic force exerted on molecules.

Chapter 3

Selective preconcentration with micro pneumatic valve system

3.1 Experimental setup

3.1.1 Strategies for selective preconcentration and online collection

In this work, repeated microchamber structures have been employed, since (1) they can suppress unexpected expansion of the ion depletion zone and vortices, (2) the electric field varies strong/weak repeatedly for easy trapping and (3) they can cut the tail of preconcentrated plugs for clear visualization. Both experimental and numerical analysis for supporting this structure are as following.

We analyzed the preconcentration behavior for various microchannel geometries. As shown in Figure 3.1(A), molecules were highly preconcentrated near the boundary of the ion depletion zone in a straight channel, while the preconcentrated plug kept propagating toward the reservoir along the boundary of the depletion zone. Because of the following extraction system, pinning the location of plugs was critical issue in our system and we had tried to resolve this by manipulating the strength of electrical field using various microchannel geometries such as funnel and narrow

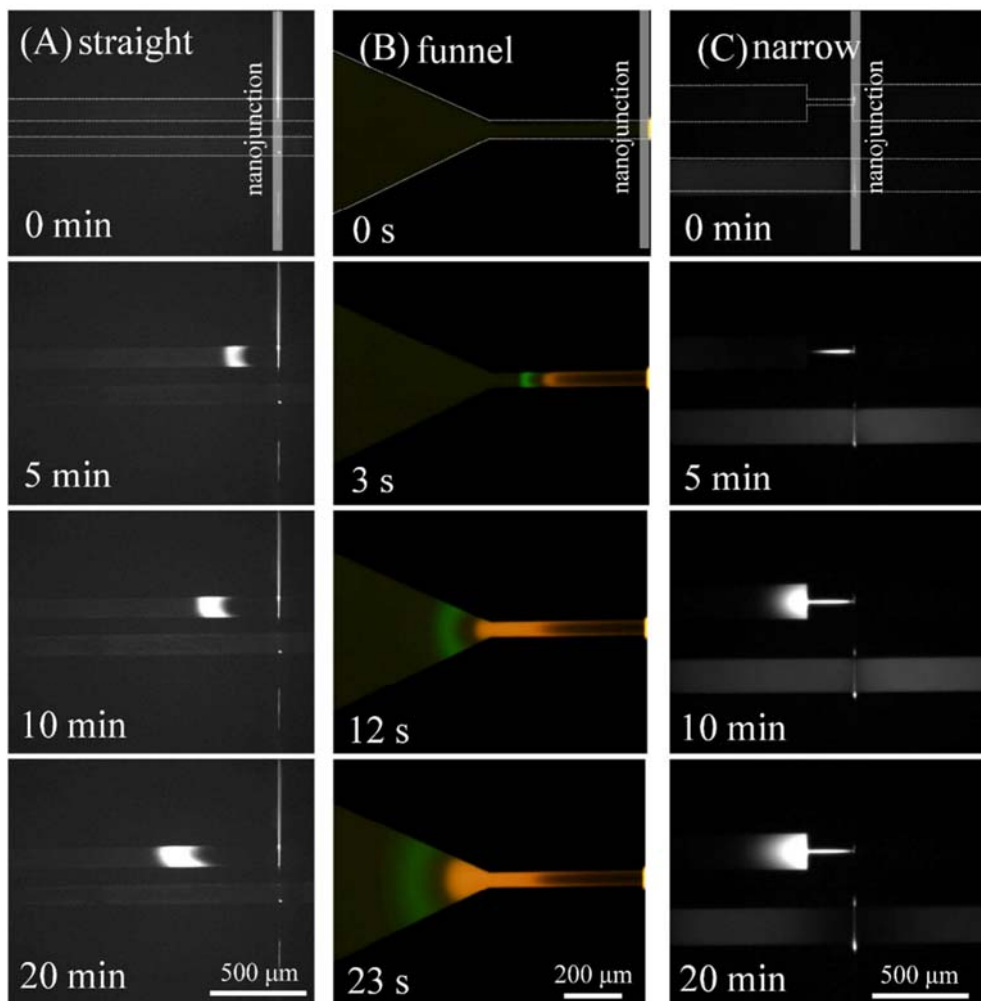


Figure 3.1 Preconcentration operation in (A) straight microchannel, (B) funnel microchannel and (C) narrow microchannel.

shape. In a funnel channel, a pre-concentrated plug was arrested at the boundary of the depletion zone which stopped expanding at the site where the channel starts to diverge. However, the second pre-concentrated plug dispersed significantly as shown in Figure 3.1(B).

In order to obtain steeper gradient an electric field,²⁶ a narrow structure was designed as shown in Figure 3.1(C). It was found that a narrow channel close to the nanojunction curbed the ever-expanding depletion zone, i.e. stabilizing (or pinning) the depletion zone. Therefore the pre-concentrated plug, which moved along the expanding depletion zone otherwise, pinned at each balanced site since the depletion zone was confined. Also, repeating narrow and wide channels impeded the dispersion and diffusion of the pre-concentrated plug. To be specific, the difference of electric field in a narrow and a wide channel engendered the difference of velocity in each channel, which facilitated the efficiency of separation.

Therefore the repeated chamber structure is supposed to have superior performance in terms of stability, cutting off tails out of Gaussian distributed plugs and helping extraction strategy. Following theoretical analysis showed that the electrical field formed at narrow section was significantly amplified so that it can act as an energy barrier to distinguish dyes. In addition, the chamber structure can effectively prohibit the expanding depletion zone by restricting vortices in the chamber.

For investigating the effect of repeated chamber structures, numerical simulations were conducted by COMSOL Multiphysics 4.4 as a commercial FEM (finite element method) tool. Because the ICP layer is highly nonlinear region, it is difficult to ensure the convergence and the stability of numerical solutions. To resolve the critical problem, the local electroneutrality (cation concentration is equal to anion concentration in whole domain) was adopted.^{22a} Namely, thin double layer approximation and ideally cation-selective membrane were chosen to reduce the computational cost. Under the local electroneutrality constraint, independent

variables such as ion concentration (c), electric potential (ψ), pressure (p), and flow fields (\mathbf{u}) were governed by the diffusion-convection equation, the current conservation, the continuity equation, and the Stokes equations.^{22b} ICP phenomena in a straight channel (4 mm in length and 150 μm in height) and a repeated chamber structure (using same geometry of experiments) were analyzed by the governing equations. For the numerical stability, the voltage configurations at inlet and outlet were set to be 5 V and 3.3 V which were enough to generate the ICP phenomena inside the microchannels. The concentrations at inlet and outlet were fixed to the bulk concentration. The flow conditions at the boundaries were set to be a zero-flow rate due to pressure balance between two reservoirs.²⁷ We assumed that the microchannel walls have uniform zeta potential of -100 mV of which value is usual condition on PDMS surface.²⁸

The simulation results were depicted in Figure 3.2. First of all, the repeated chamber structures are able to effectively confine the ion depletion zone (dark blue region) in comparison to the straight channel as shown in Figure 3.2(A). This means that the ICP layer in the repeated chamber would be stabilized because the flow instability generated by concentration fluctuation⁴ occurs only inside the first chamber where nanojunction was installed. This is helpful to obtain the stable preconcentrated plug after the first chamber. As depicted in Figure 3.2(B), the strength of electric field was changed monotonically in the longitudinal direction of the straight channel while the strength was altered pseudo-periodically for the repeated chambers. Electric potentials obtained from the electrical field strength were schematically illustrated in Figure 3.2(D). While monotonically increased electric potentials were observed in straight microchannel (red line), there was a (almost) plateau inside microchamber with steep changes in narrow regions (blue line). A charged species would be immobilized in this plateau region. Due to the pseudo-periodic electric field and the plateau of electric potential, the preconcentrated plug would be easily trapped in each chamber. Lastly, fast vortices

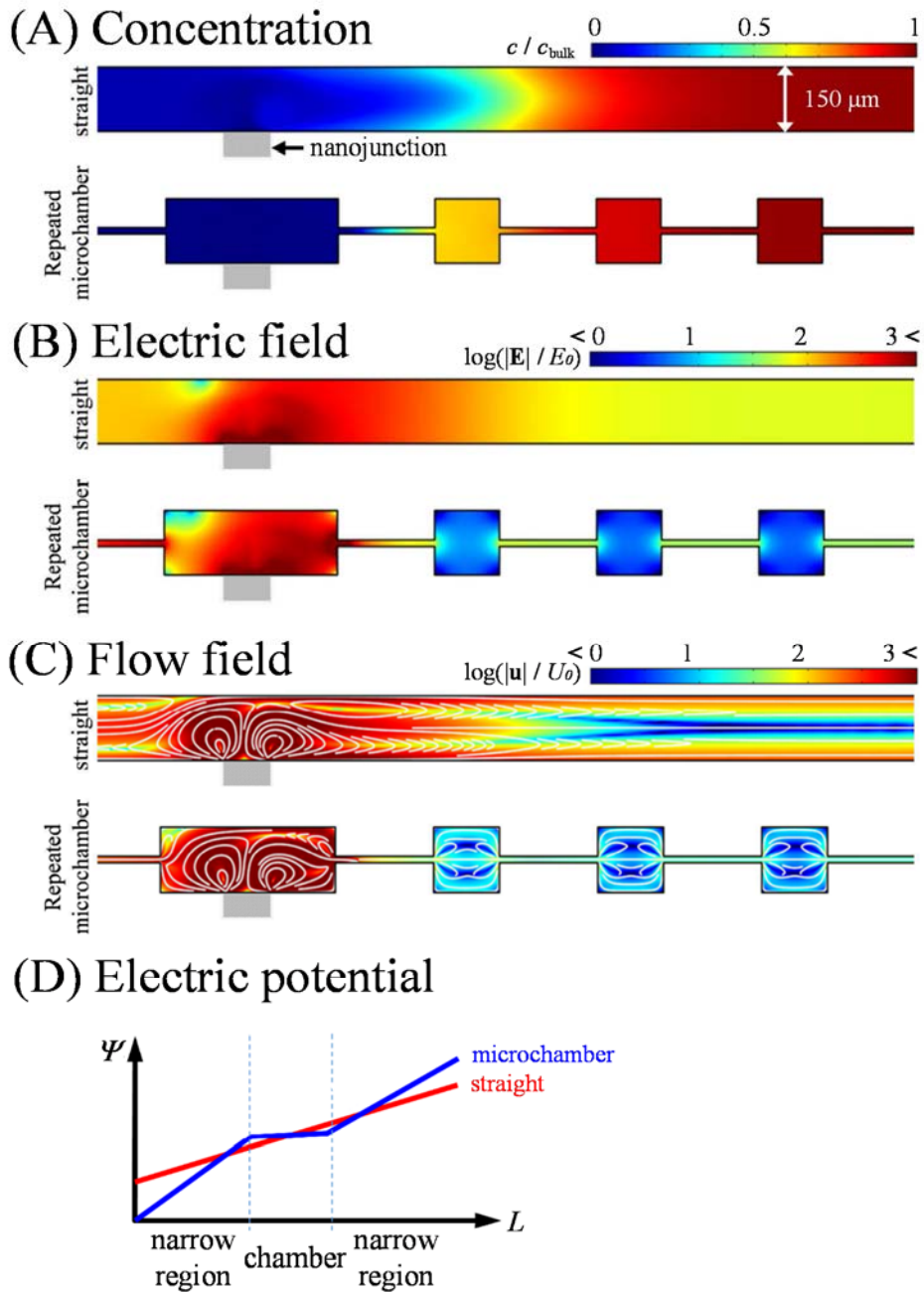


Figure 3.2 Numerically simulated ICP layer for (A) concentration distribution, (B) electrical field and (C) flow field. (D) Schematic illustration for electric potential near the microchamber.

were confined in the first chamber so that stable flow fields were generated beyond the chamber (Figure 3.2(C)). Thus, the alterations of ICP layer by the repeated chambers would provide effective mechanisms for a stable selective preconcentration.

3.1.2 Preparation of PDMS microchips

Figure 3.3(A) showed the microscopic image of the multilayered selective preconcentration device with pneumatic valve system. We implemented microchamber structures repeatedly to suppress fluidic instability and differentiate the flow velocity within a single channel. Buffer channel was connected to the main channel with a perm-selective Nafion membrane. The depth of all microchannels was fixed to 15 μm and three microchambers (150 μm X 150 μm) were connected by 15 μm X 225 μm microchannel as shown in Figure 3.3(A). At the right most microchamber, a microchamber with the same size was upwardly connected to collect isolated preconcentration plugs. There were fundamental and practical reasons to set the narrow height as 15 μm . In current design, the microchamber structure has the repeated height of 150 μm (wide height) and 15 μm (narrow height) in order to keep 10 : 1 ratio. The numerical simulation taught us that 10 : 1 was enough to focus the electric field and keep the position of the plug. Here, the wide height over 150 μm would give disperse preconcentrated plug so that we set the maximum wide height as 150 μm . The practical reason was that a mask resolution under 15 μm cost 5 times more expensive than the mask resolution over 15 μm , leading to a hurdle for commercialization. By both reasons, we kept 150 μm : 15 μm in current design. A rib-shaped channel was also subsequently connected to be used as a measurement window. Microvalves (the width and height were 290 μm each) were designed to cover 4 locations as indicated with red ink in Figure 3.3(A). Note that each microchamber could have its own collection channel depending on the

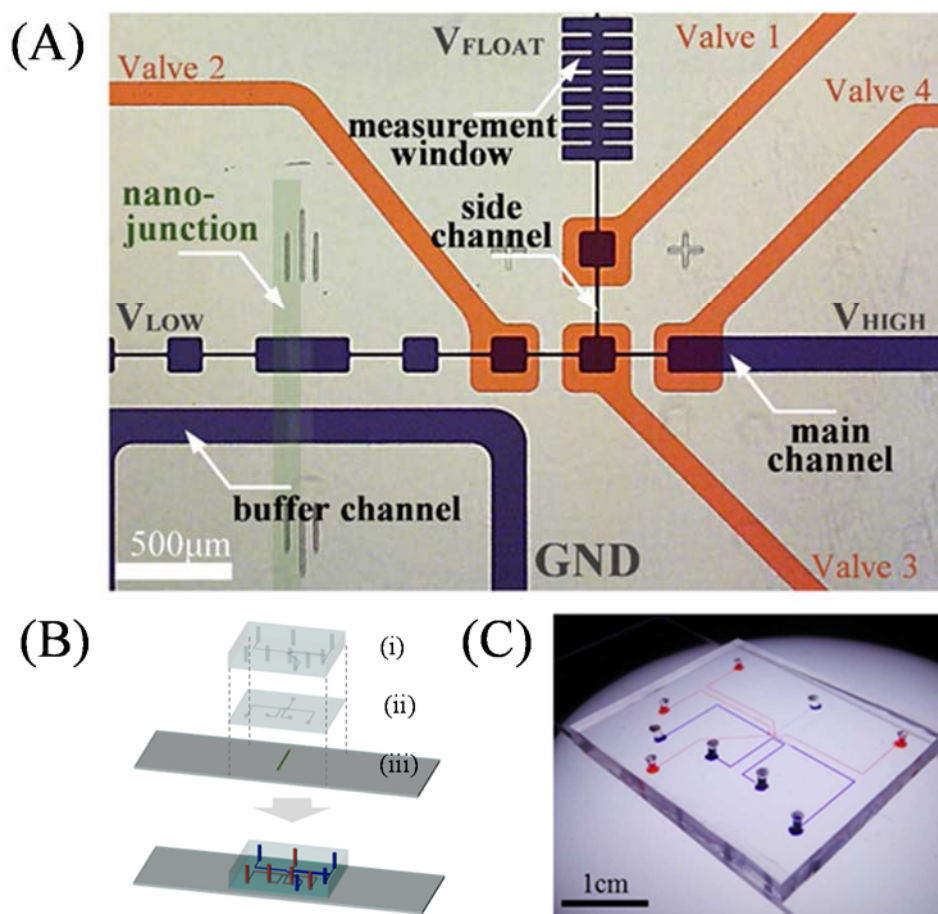


Figure 3.3 (A) Microscopic view of the selective preconcentration device. The microchannels in the ICP layer were indicated with blue and the microchannels in the valve layer were indicated red. (B) An exploded view of the device with (i) a valve layer, (ii) an ICP layer and (iii) a Nafion patterned slide glass. (C) Assembled multilayered online selective preconcentration device.

location where target analytes were preconcentrated. However, in this work, we designed the device with only one collection channel to show the possibility of achieving the collection of selectively preconcentrated dyes. If one would like to collect dyes from different microchambers, one could install additional collection channels to the microchamber.

The first layer as shown in Figure 3.3(B)-(ii) is an ICP layer where selective preconcentration occurred. This thin layer is followed by valve layer as shown in Figure 3.3(B)-(i) which blocks the ICP layer pneumatically. The thickness of the layer between an ICP channel and a valve channel is 10 μ m and it is thin and elastic enough to block the ICP layer when air comes in. Fabrication methods were described as follows. A 4-inch wafer was spun to coat 15 μ m layer of SU-8 2015 photoresist (MicroChem. Inc, USA) at 500 rpm of 10 seconds (pre-spinning) and at 3250 rpm for 30 seconds (spinning). After 3 minutes of soft bake at 95 °C, the layer was exposed two times to ultraviolet (UV) of 365 nm wavelength for 23.3 seconds (400 mW) using a mask aligner. Post bake was for 4 minutes at 95 °C, then was soaked in isopropyl alcohol (IPA) for 3 minutes. For easy detachment of the PDMS device, trichloro(1,1,2,2- perfluorooctyl)silane was applied to the master wafer with a vacuum assisted deposition desiccator. PDMS base and curing agent (Sylgard 184 Silicone elastomer kit, Dow Corning, USA) were mixed at 10 : 1 ratio and desiccated in a vacuum pump for 1 hour to remove air bubbles. The mixed solution was poured onto the master and cured in room temperature overnight for the valve layer (Figure 3.3(B)-(i)), preventing alignment error due to thermal shrinkage. For the ICP layer, the mixed solution was poured onto the patterned 4-inch wafer and spun at 1500 rpm for 300 seconds (JSP4A, JD Tech, Korea) to coat 25 μ m PDMS layer (Figure 3.3(B)-(ii)). Then, the coated wafer was placed on a hot plate for 30 minutes at 95 °C. The PDMS replicas were peeled off from the master and the inlet and outlet holes were punched out. A polymeric nanoporous material, Nafion (20 wt% resin, Sigma Aldrich, USA), was used for the nanojunction between the microchannels. A single

strip of Nafion (100 μm wide and 1 cm long) was patterned on a slide glass using a PDMS piece that has a single straight microchannel and was heated at 95 $^{\circ}\text{C}$ for evaporating solvent after removing the PDMS piece (Figure 3.3(B)-(iii)).¹⁸ Then, each layer was bonded to the Nafion patterned slide glass by oxygen plasma bonder (Femto Science, Korea) under an alignment through the stereo microscope (SZ61, Olympus, Japan) creating a multilayer device. Final assembled micro/nanofluidic device is shown in Figure 3.3(C).

3.1.3 Materials and reagents

Fluorescent dyes were used for observing preconcentration efficiently, which is Sulforhodamine B (Sigma Aldrich, USA), Alexa Fluor 488 (Invitrogen, USA), Alexa Fluor 532 (Invitrogen, USA), and CoroNa Green (Invitrogen, USA). Figure 3.4 describes chemical structure of each molecule. As shown in Table 3.1, sulforhodamine B (SRB) has -1 net charge, and its color is orange color because its maximum absorption wavelength is 565 nm and its maximum emission wavelength is 586 nm. In the case of Alexa Fluor 488 (Alexa 488) and Alexa Fluor 532 (Alexa 532), they have the same -2 net charge but each color is different since they have different absorption wavelength (~ 495 nm and ~ 532 nm for each) and emission wavelength (~ 519 nm and 554 nm for each). CoroNa Green has zero net charge and it absorbs light near 492 nm wavelength and emits cyan-green color light with 516 nm wavelength.

In the experiment of selective preconcentration and online collection, 5 mM KCl solution (Sigma Aldrich, USA) was used with addition of fluorescent dyes for a main channel solution. Their separation and preconcentration dynamics were able to be measured and identified with two different fluorescent colors of orange (SRB) and green (Alexa 488). The concentration of sulforhodamine B was 24.14 nM and that of Alexa 488 was 0.90 μM . For a buffer channel solution, 100 mM KCl was used to minimize a voltage drop in the buffer channel. The ICP operation has been

Dye	Color	Absorb [nm]	Emit [nm]	Net charge
Sulforhodamine B	orange	565	586	-1
Alexa Flour 488	cyan-green	495	519	-2
Alexa Fluor 532	green	532	554	-1
CoroNa Green	cyan-green	492	516	0

Table 3.1 Chemical and physical properties of Sulforhodamine B, Alexa Fluor 488, Alexa Fluor 532, and CoroNa Green.

well performed in high salinity samples over 100 mM.^{23,29} In this work, 5 mM KCl was chosen under assumption that the real sample could be post-processed such as removing large molecules and cells (dilution). In such case, the solution of 5 mM concentration would be a proper standard model.

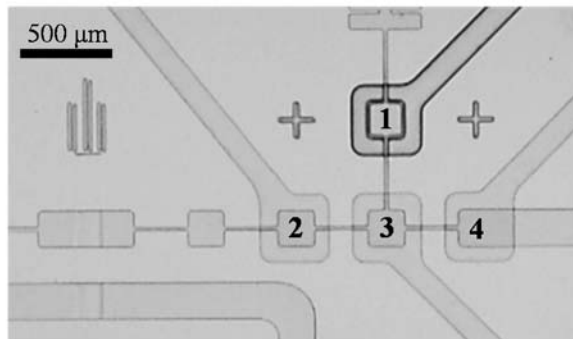
In the experiment of dynamics in preconcentration mechanism, 1 mM KCl solution was used for each main channel and buffer channel. The concentration of sulforhodamine B, Alexa 532, and CoroNa Green was 25 nM, 0.5 μ M, and 34 μ M for each.

3.1.4 System operation method

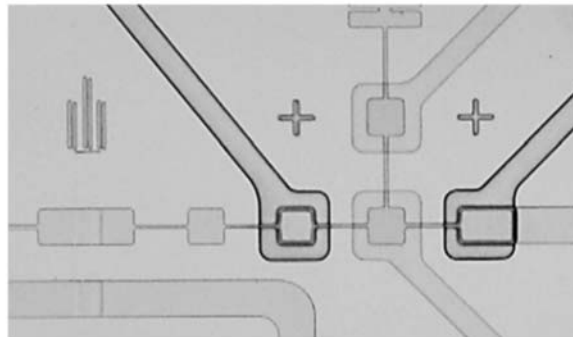
Chemical samples were loaded into the main and buffer microchannel by applying positive pressure from each inlet reservoir. Ag/AgCl electrodes were inserted into the inlet and buffer reservoirs on the device and connected to a power supply (Keithley 6517 and Keithley 238, Keithley Instruments, USA). For applying the electric field, an independent voltage control was required on each of the four reservoirs. For the continuation on separation and preconcentration, 60 V and 90 V were applied to the left and the right reservoir of the main channel, respectively, while the reservoir of the buffer channel was grounded. The motions of fluorescent dyes were tracked by an inverted fluorescence microscope (IX53, Olympus, Japan) and recorded by CellSens (Olympus, Japan) computer program.

A compressor (Gfrog, Stylex, Korea) as a pressure source was connected to 4 mini solenoid valves (SY 3120, SMC pneumatic, Korea) and a polystyrene tube connected a solenoid valve and an inlet of valve layer in the PDMS device. Before the connection, DI water was filled into the microchannels of valve layer to reject air bubbles into the ICP layer. In order to manipulate the pneumatic microvalves automatically, a customized LabVIEW code (National Instrument, USA) and a DAQ board (USB-DAQ 6341, National Instrument, USA) were used. The valve operation consisted 3 steps as shown in Figure 3.5. Step 1 (ICP preconcentration): valve 1 was

(A) Step1 : ICP precon.



(B) Step2 : Isolate



(C) Step3 : Collect

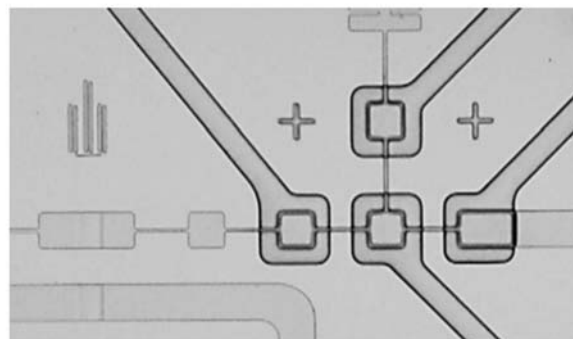


Figure 3.5 Microscopic images of 3-step valve control sequence: Step1 - ICP preconcentration to form a highly concentration plug, Step 2 - isolation of a highly preconcentrated plug at specific microchamber, and Step 3 - collection of the highly preconcentrated plug into upward channel.

closed when selective preconcentration was in process. Step 2 (isolation): when the targeted preconcentration plug reached the microchamber which was connected to the side channel, valve 1 was opened and valve 2 and 4 were closed to isolate the sample plug from the main channel. Step 3 (collection): then, by closing valve 1 and 3 while valve 2 and 4 were still closed, the isolated plug was squeezed into the measurement window. Fluorescent dyes diffused into a larger area and the fluorescence intensity was analyzed without being saturated. By leaving valve 1 closed and others opened, the whole 3-step process cyclically repeated for further collections. One can control the duration of Step 1 to obtain a different preconcentration ratio. Three microchambers with valves were basic building blocks under our current system. If more than 2 analytes are needed to be preconcentrated and separated, the number of microchambers and valves could be added. To do this, the number of microchamber should be larger than the number of analyte. For a different kind of dyes rather than SRB and Alexa, one can tune the electric field to fill targeted microchamber at one's discretion. Here the three-microchamber system was enough for selective preconcentration of 2 dyes regardless of the types of dye.

3.2. Experimental setup

3.2.1 Demonstration of selective preconcentration

Figure 3.6 demonstrated that two different dyes were simultaneously preconcentrated and separated over time. Without electric field along the nanojunction, no fluorescent dyes were observed in the channel because the initial concentrations of dyes were too low to be detected. As we applied 90 V for V_{HIGH} and 60 V for V_{LOW} on each end of the main channel with grounded buffer channel, ICP was triggered nearby the membrane. Micro air bubbles could be generated at the electrode surface with $O(10)$ nA operation currents. Even with these relatively high applied voltages, most of electrical potential was dropped inside the ion depletion zone. In addition, because the electrodes were inserted at the reservoirs

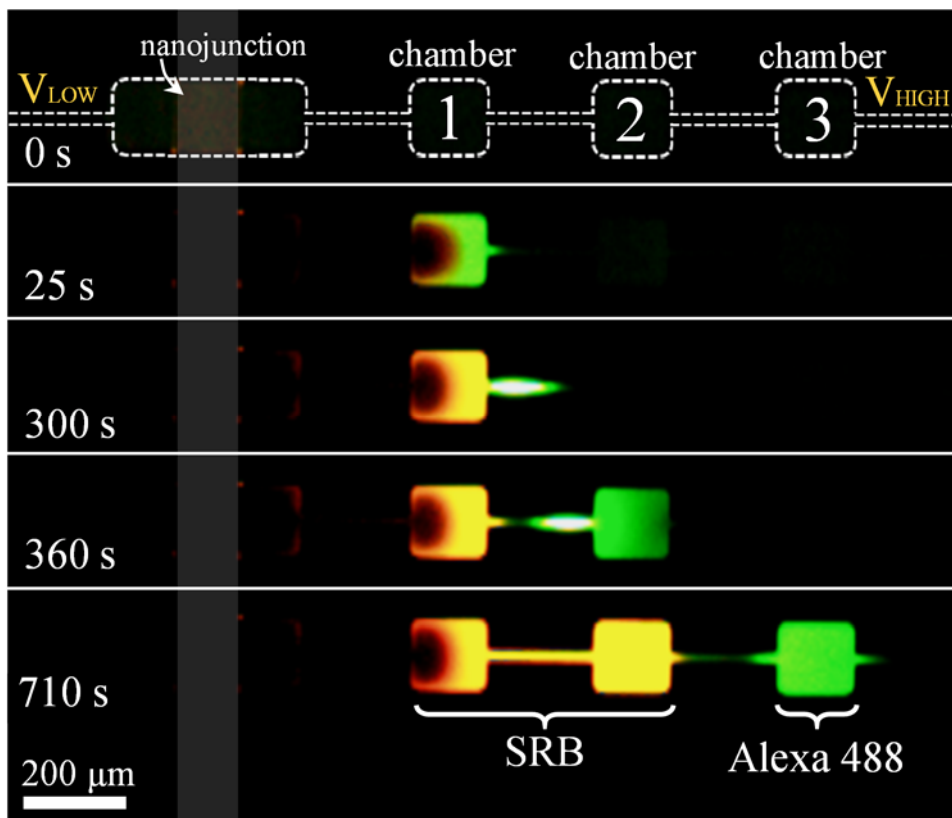


Figure 3.6 Time-lapse images of selective pre-concentration of SRB and Alexa 488. High Concentration ratio was represented by the brightness of fluorescence. Since the physicochemical properties of two dyes were different, they were pre-concentrated at different locations.

which located far from the nanojunction and the reservoirs were opened to ambient atmospheric pressure, the bubble at the electrode surface can float and disappear into the air so that the selective preconcentration operation was not interfered by the bubbles. As reported in previous researches,⁴ the ion depletion zone caused significant and dynamic perturbation in a local ion concentration and in an amplified electric field near the membrane along with the generation of strong electrokinetic flow. The high electric field gradient at the boundary of depletion zone rejected the penetration of charged molecules into the ion depletion zone so that both dyes stacked and detected at the boundary.¹⁵ At the beginning of selective preconcentration, both dyes were preconcentrated in the microchamber 1. After the ion depletion zone became stabilized over time, the preconcentrated plugs of two dyes with different mobility were separated with a separation resolution³⁰ of 1.75. We have adopted the definition of the separation resolution as $R_s = (\text{peak to peak distance})/(\text{average width of bands})$ leading to R_s of 1.75 ($525 \text{ nm}/((450 \text{ nm} + 150 \text{ nm})/2)$). This number indicates a perfect separation (i.e. no overlap) in case of Gaussian distribution. While there has been no exhaustive theoretical analysis on this selective preconcentration process, the mechanism of selective preconcentration was empirically analyzed using force balance.^{11, 31} The force is mobility times particle velocity³² so that we would like to discuss the balance in terms of force rather than mobility, since the size of molecules ($\sim 1 \text{ nm}$) were similar. This separation was drawn by the equilibrium between an electroosmotic drag force and an electrophoretic force as described in Figure 5.¹¹ According to an experimental observation shown in Figure 3.6, Alexa 488 (green) moved toward the right reservoir, while SRB (orange) stayed near the depletion zone boundary. Since F_{drag} is mainly determined by R which is almost the same for SRB and Alexa 488, the value of net charge played a key role in determining the equilibrium positions balanced by F_{drag} and F_{EP} . This argument was in line with the experimental result since the net charge of SRB and Alexa 488 is -1 and -2, respectively.

3.2.2 Stabilization of selective preconcentration

While the phenomenon of different equilibrium positions of molecules with different mobility has been already reported in previous researches,^{11, 31} one strong plug and one smaller plug in parabolic shape were reported and the locations of preconcentrated plugs were always unpredictable due to the strong instability by local amplified electric field near the nanojunction,⁴ instead of stably generated plugs with high concentration. Therefore, it was important to control the positions of the concentrated sample plugs and to stabilize the ion depletion zone. In our system, the repeated narrow and wide channels were able to stabilize the depletion zone by restricting the expansion of vortices and strong electrokinetic flows in the ion depletion zone,^{17b-d, 19, 26} thereby forming a plug at desirable positions. The repeated microchamber structures were able to effectively confine the ion depletion zone in comparison to the straight channel. This meant that the ICP layer in the repeated chamber would be stabilized since the flow instability was generated by concentration fluctuation³³ only inside the first chamber nearby nanojunction. Also, due to the pseudo-periodic electric field and the plateau of electric potential, the preconcentrated plug would be easily trapped in each chamber. Consequently the control of each accumulated molecules' location became simple and tailing effect was reduced. This alternating geometry also differentiated the velocity of the fluidic flow at the boundary between the narrow and the wide channel, and therefore, it increased the efficiency of separation and helped the membrane microvalve system for further blocking and squeezing of the analytes.

3.2.3 Quantitative analysis for separation and preconcentration efficiency

The selective preconcentration was quantitatively analyzed by measuring pixel intensity with fixed exposure time. The intensities of the original sample and reference solutions at different concentrations were compared to accurately measure

the preconcentration ratio, since the pixel intensity was not linearly proportional to the concentration of dyes. As shown in Figure 3.7, the average pixel intensities of dyes increased in each microchamber in order. The both dyes (Alexa 488 + SRB) were rapidly preconcentrated in the microchamber 1 from the initial to 10 minutes. From 10 minutes to 25 minutes, the green plug (Alexa 488) moved to the microchamber 2 while the intensities of the plugs simultaneously increased. This agreed with the microscopic image in Figure 3.6 that the orange plug (SRB) stayed in the microchamber 1, while the green plug (Alexa 488) moved to the microchamber 2. After 25 minutes, the green plug (Alexa 488) moved to the microchamber 3, while the average pixel intensity of the microchamber 2 sharply diminished. In this point, the average pixel intensity of the microchamber 2 did not decrease to zero. This was because the orange plug (SRB) was saturated in the first microchamber so that it went on to the microchamber 2. In the microchamber 3, the average pixel intensity reached up to 98.2, which denoted that the green plug (Alexa 488) was preconcentrated above 100-fold since the average pixel intensities of 10X, 50X, and 100X concentrations of Alexa Fluor 488 were 12.9, 58.9, and 95.3 respectively. After 30 minutes, the repeated microvalve operations were started, showing severe fluctuations and this part will be discussed later. In previous researches, the two separated plugs have been distinguished only by their positions since only one dye was tagged for two or more different kinds of molecules.^{11, 31} Compared to these works, RGB color profile was rigorously investigated to validate the separation of two molecules. Since the emission from SRB has both red and green color, it was efficient to measure color intensities from microchamber 3 as the indicator of separation, where only Alexa 488 dye was preconcentrated. Since the pixel intensities of blue and red were almost the same, only red and green colors were discussed. The color profile of 100-fold reference solution of Alexa 488 at 0.90 mM was 33.28 in red and 219.76 in green under the exposure time of 300 ms. As shown

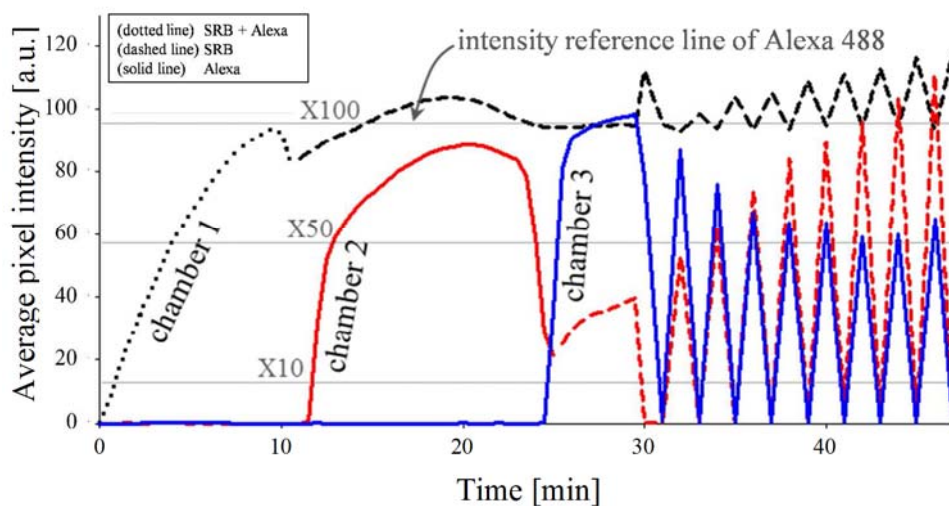


Figure 3.7 Overall fluorescence intensity tracked in each microchamber as a function of time. Dotted line, dashed line and solid line represented the mixture of SRB with Alexa 488, only SRB and only Alexa 488, respectively. Three different colors indicated the pixel intensity of each microchamber (black for microchamber 1, red for microchamber 2 and blue for microchamber 3). The concentration ratio of selectively preconcentrated Alexa 488 in microchamber 3 exceeded 100-fold, maintaining the preconcentration factor high enough in repeated valve operations.

in Figure 3.8, the pixel intensity of the microchamber 3 in the main channel was 223.20 in green and 31.17 in red at the operation time from 25 minutes to 30 minutes, which agreed with the reference values of the 100-fold, meaning that the majority occupying the microchamber 3 was only Alexa 488 dye. In addition to this, the color profile of the microchamber 1 (Figure 3.9) contained high value of red color which was not found in the microchamber 3 as shown in Figure 3.8. The ratio of red and green color was reversed at 10 minutes and maintained around 2 : 1 from 25 minutes to 30 minutes in the microchamber 1. Since SRB was dominant in the original solution (SRB at 24.14 nM + Alexa 488 at 0.90 μ M) and its red/green ratio was 2 : 1, we concluded that the microchamber 1 was solely occupied by SRB after 25 minutes. This color profile measurement provided an accurate platform to measure the separation efficiency between two dyes with different mobility.

3.2.4 Collection of preconcentrated plugs by valve system

As the operation continued further, the preconcentration factor increased accordingly. However, subsequent process using selectively preconcentrated analytes was difficult since the selective preconcentration was performed while the background solution freely flows in a single channel. Besides, a subsequent on-chip process which should exclude electrical operation was inapplicable because the plug drastically dispersed as shown in Figure 3.10(A) when the applied voltage was turned off. To resolve this problem, a plug was required to be isolated and transported to another site, while the preconcentration ratio maintained without loss for either on-chip or off-chip applications. This was able to be realized using pneumatic microvalve system. To guarantee the role of valves to block the plug from the original sample channel, the extent of dispersion was compared between the cases of valve OFF and valve ON as described in Figure 3.10(A) and (B).

The valves were operated in a repeated cycle as described in Figure 3.5 to collect the selectively preconcentrated plug into the side channel. In a cycle, the plug was

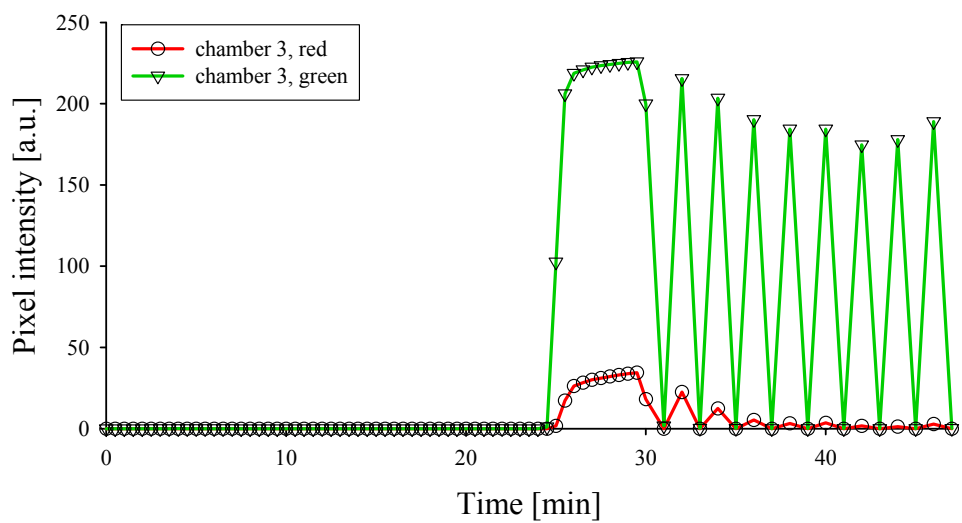


Figure 3.8 Red/green color profile in microchamber 3, showing the microchamber 3 only had Alexa 488.

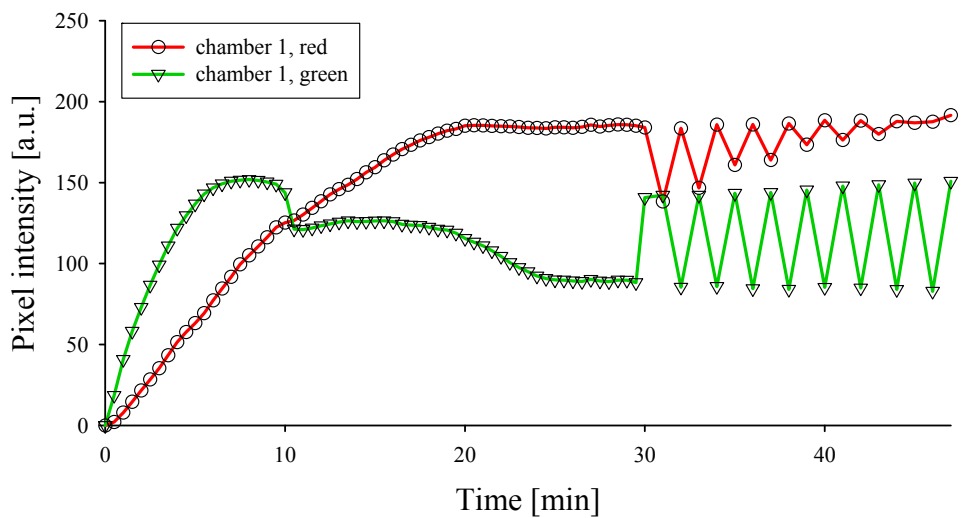


Figure 3.9 Red/green color profile in microchamber 1, showing the microchamber 1 only had SRB. Fluctuations after 30 minutes in all plots showed that the preconcentration factor maintains over 50-fold along the cyclic valve operations. While the error bars were omitted for clear visibility, the tests were conducted at least 10 times with different devices for the repeatability and reliability.

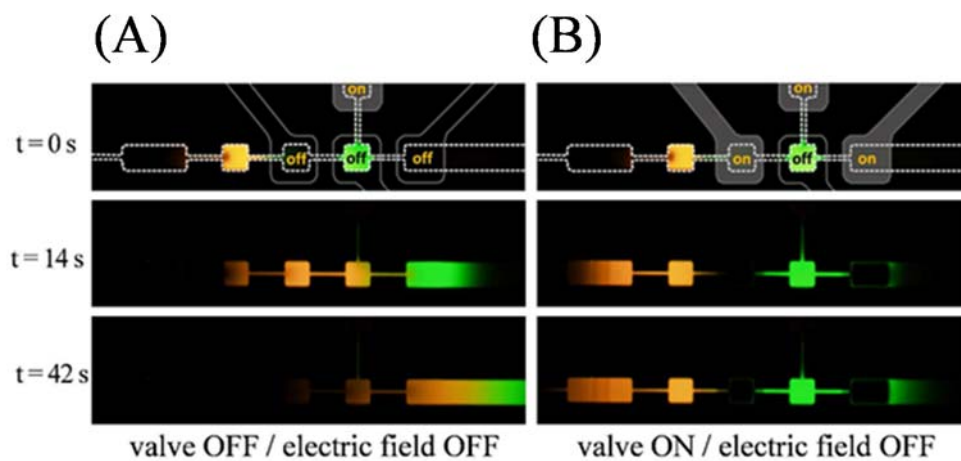


Figure 3.10 Time-lapse images showing the dispersion of isolated plug when the valves were (A) OFF and (B) ON.

isolated from the original sample solution and squeezed up into the side channel. To analyze the preconcentration factor achieved from the process, a rib-shaped measurement window was installed in the middle of the side channel. This measurement window was designed for metering how high the preconcentration ratio would be achieved through the process. In the meantime, the measurement window had larger area than the side channel itself so that it had low fluidic resistance and the side channel connected to an open reservoir to atmospheric pressure, allowing subsequent processes without any disturbance. As shown in Figure 3.11(A), no fluorescence intensity was observed in the measurement window at $t = 0$, because the measurement window was initially filled with sample solution. By the first valve operation, the pixel intensity of measurement window already exceeded 10-fold of the initial concentration of Alexa 488 as plotted in Figure 3.11(B). With repeated valve operations, the concentration of collected plugs in the measurement window continuously increased so that the concentration reached over 30 times of the initial concentration after the sixth operation. After the ninth collection, it was observed that the measurement window was fully filled with green dyes. After this point, a diffusive mixing would not occur anymore. The error bars decreased and the signal saturated according to the number of valve operation, since we measured area averaged fluorescent intensity in whole measurement window. It led largest error bar at the 1st collection because the window was not fully filled with the dye.

The preconcentration factors of each Step 1 in repeated cycles were maintained high enough to continuously increase the pixel intensity of the measurement window. Figure 3.7 also supported this result. In the Figure, the valves were repeatedly operated in the same cycle with the interval of 2 minutes after 30 minutes of selectively preconcentrating operation. When the analytes in the microchamber 3 were isolated by valves and moved up into the side channel, the pixel intensity of the microchamber 3 was zero. The intensity of microchamber 3 increased again with the

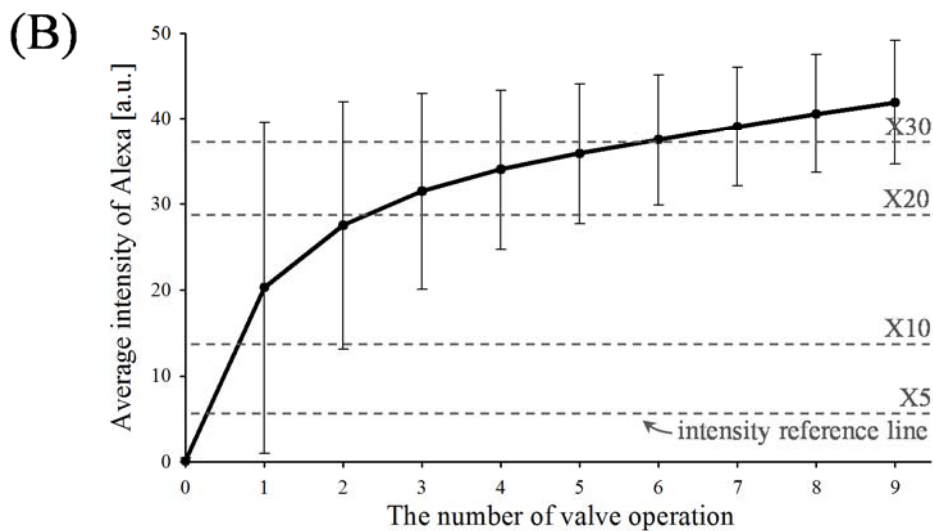
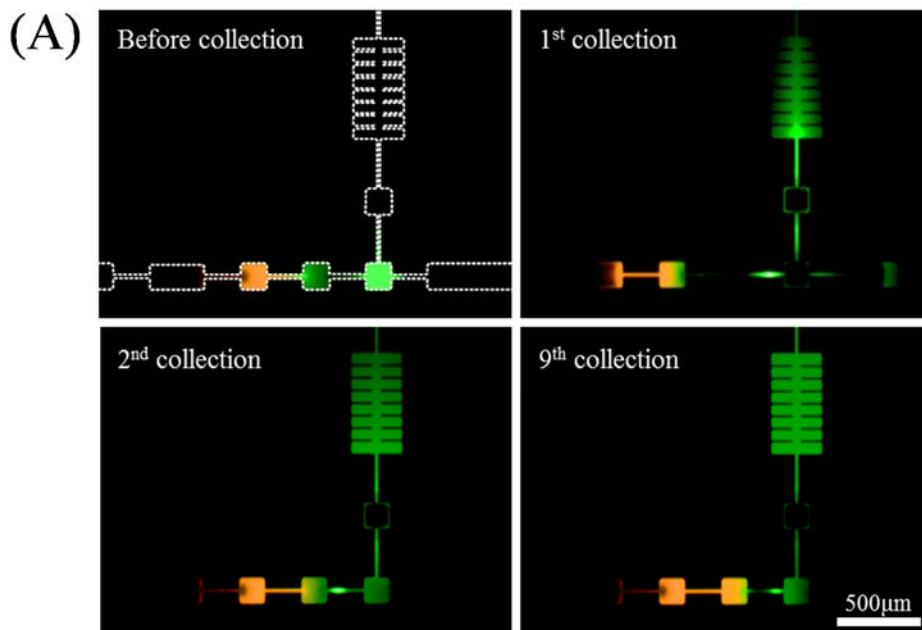


Figure 3.11 (A) Snapshots of repeated valve operations collecting selectively preconcentrated plugs. Compared to the initial state, the measurement window was being filled with green dye (Alexa 488) over several valve operations. (B) Average intensity change in the measurement window over number of repetition of valve operations. The average intensity exceeded 10-fold in a single valve operation, and 30-fold after nine operations. Note that there was no SRB in the measurement window.

next preconcentration operation for 2 minutes. The concentration of Alexa in the microchamber 3 was maintained over 50-fold for all valve operations. The upheld high preconcentration ratio of collected sample was led by stable and reproducible valve operations. Since microvalve systems squeezed the preconcentrated plugs by mechanical force, the mechanism of the collection process barely agitated the external electric field.

3.2.5 Three kinds of analyte

For being used in practical applications, solutions mixed with various kinds of molecules should be considered. Therefore, it is need to confirm that multiple components with different physicochemical properties in solution can be simultaneously preconcentrated and separated under ion concentration polarization. Note that molecules dealt with in this experiment are negatively charged since only cation-selective membrane was used. In conventional methods using ion concentration polarization, there are few demonstrations reported which selectively preconcentrated more than two kinds of analyte.^{5, 11} However, in the studies, separated plugs were observed but it is not confirmed whether each plug is composed of single kind and the order is from high mobility to low mobility. Thus, it is need to investigate more in to confirm that multiple components can be simultaneously preconcentrated and separated under ion concentration polarization in order of the magnitude of mobility.

Figure 3.12 shows simultaneous preconcentration and separation of three different kinds of analyte, which are SRB, Alexa 488, and Alexa 532. Tangential electric field was generated with 45 V and 70 V for each low voltage and high voltage. This voltage configuration was empirically adjusted for effective selective preconcentration. When the voltage was applied, ion depletion zone was developed and three dyes were preconcentrated at chamber 1. After 70 s, only the preconcentrated plug of Alexa 488 propagates to chamber 2. After 160 s, Alexa 532

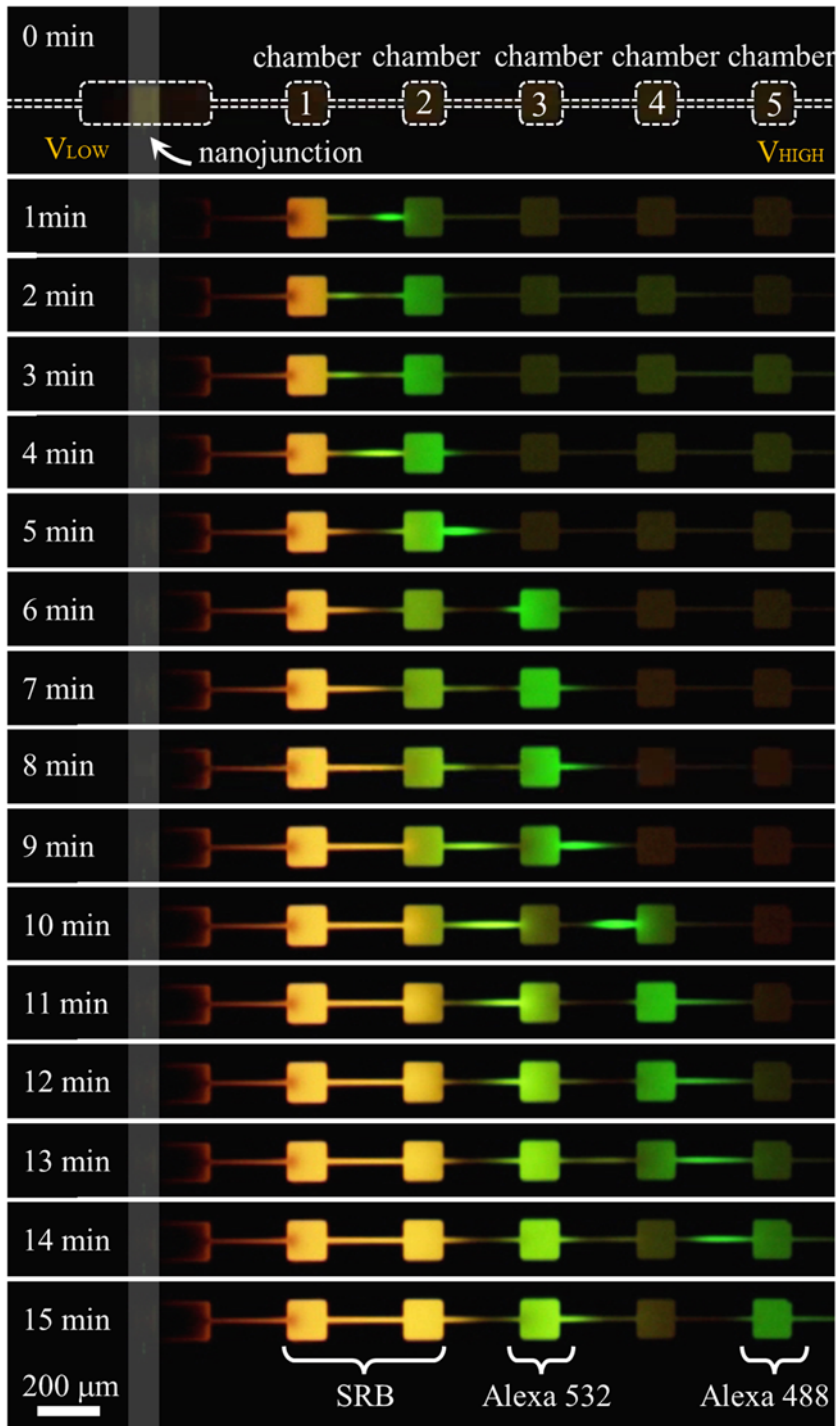


Figure 3.12 Time-lapse images showing the selective preconcentration of SRB, Alexa 532 and Alexa 488. Three different dyes were simultaneously preconcentrated and separated.

was separated from SRB and moved to chamber 2. In this point, the chamber 2 was occupied with Alexa 488 and Alexa 532. Around 5 minutes, Alexa 488 in the chamber 2 started to move to chamber 3 while Alexa 532 stayed still in the chamber 2. Consequently, three different dyes were successfully separated while the concentration of each preconcentrated plug was increased. As separated three plugs moved toward the reservoir with high voltage due to electrophoretic mobility, the plugs were not mixed over time.

The concentration ratio of each dye was quantitatively investigated through examining pixel intensities. In the case of Alexa only green pixel intensity was examined as shown in Figure 3.13. Alexa 488 was preconcentrated up to nearly 30-fold in chamber 1. However, as Alexa 488 dye moved to the next chambers, the concentration of preconcentrated plug became decreased. Also, the slope of the pixel intensity decreased, which means that the preconcentrated plug dispersed along with the movement. Figure 3.14 represents green pixel intensity with the reference line of Alexa 532. It showed that the concentration of Alexa 532 increased as it moves to the next chambers. Although the initial concentration of Alexa 488 and Alexa 532 was the same in the main channel solution, the tendency turned out to be completely different. As it was in the case of Alexa 488, the plug of Alexa 532 was also dispersed as it moved but the concentration ratio became increased and exceeded 100 times of initial concentration ratio after 20 min. It is interesting phenomenon requiring further investigation. In the case of SRB, only red pixel intensity was examined as shown in Figure 3.15 other than green and blue pixel intensity. Before moving to the chamber 2, the concentration of SRB was increased almost 50-fold. Also, the concentration of SRB became gradually increased even after propagating to the next chamber. This means that dyes from the reservoir with high voltage were continuously preconcentrated in the first order over time even with the existence of the other two dyes.

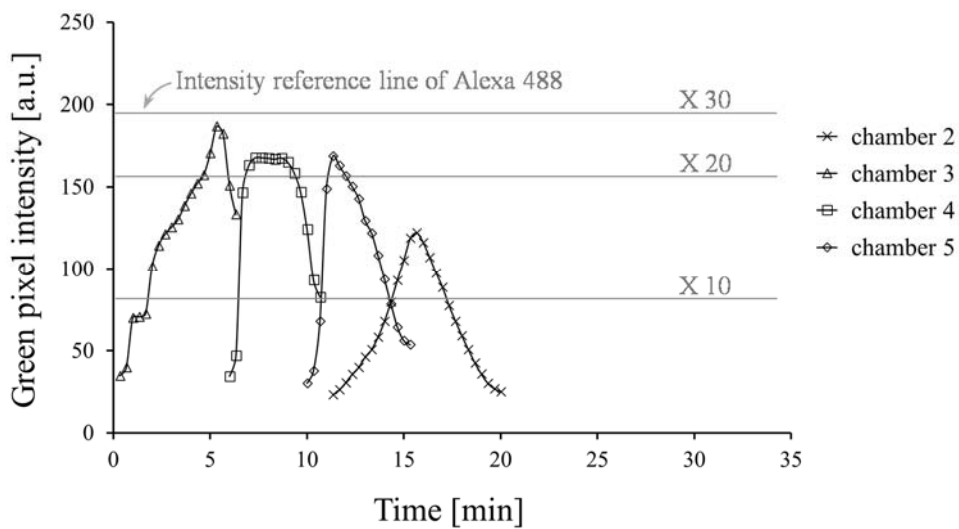


Figure 3.13 Green pixel intensity tracked in each microchamber as a function of time with the intensity reference line of Alexa 532. A triangular marker, a rectangular marker, and a diamond marker, and x marker represent the green pixel intensity in microchamber 2, microchamber 3, microchamber 4, and microchamber 5, respectively.

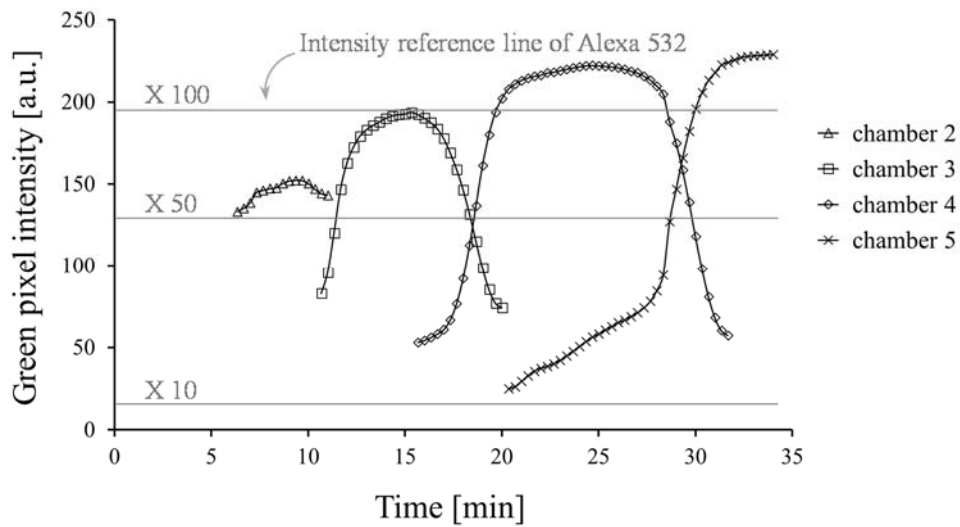


Figure 3.14 Red pixel intensity tracked in each microchamber as a function of time with the intensity reference line of SRB. A circular marker, a triangular marker, a rectangular marker, and a diamond marker represent the red pixel intensity in microchamber 1, microchamber 2, microchamber 3, and microchamber 4, respectively.

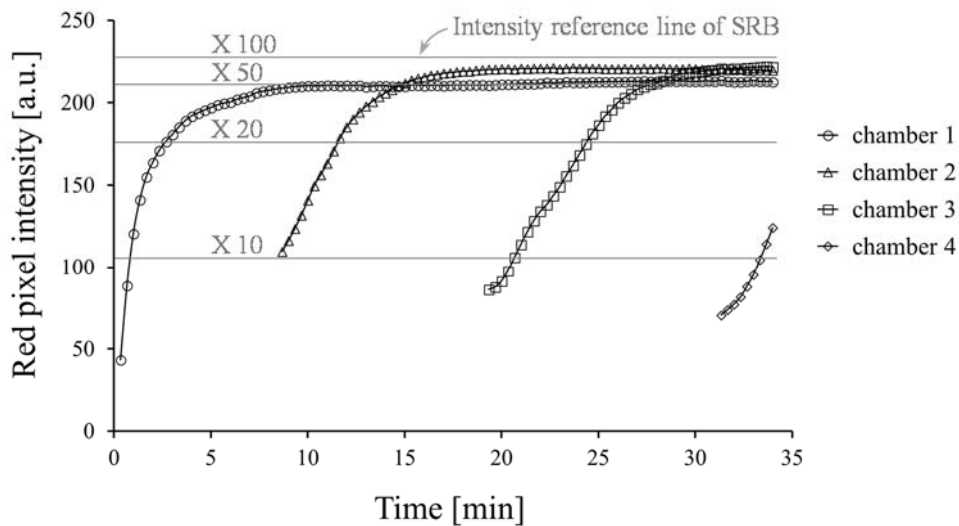


Figure 3.15 Green pixel intensity tracked in each microchamber as a function of time with the intensity reference line of Alexa 488. A triangular marker, a rectangular marker, and a diamond marker, and x marker represent the green pixel intensity in microchamber 2, microchamber 3, microchamber 4, and microchamber 5, respectively.

3.2.6 Correlation between voltage configuration and separation time

When different molecules are selectively preconcentrated, time to take for separation determines separation efficiency as well as separation resolution does. It is difficult to optimize voltage configuration for separating negatively charged molecules near cation-selective membrane to be fast with sharp separation resolution since increasing electric field reversely enhances the magnitude of electrophoretic force and electroosmotic force in an opposite direction. Therefore, investigation with different voltage values of V_{HIGH} and V_{LOW} is required to find optimal condition.

In this part, 20 V, 30V and 40V were taken for V_{LOW} , and 80 V, 90 V, 100 V, 110 V, and 120 V were taken for V_{HIGH} in order to find optimal condition by measuring time for separation and the extent of dispersion. Figure 3.16 showed representative three results among those voltage configurations. The difference (ΔV) between V_{HIGH} and V_{LOW} is 100 V, 80 V, and 80 V for each but V_{HIGH} which dominates the generation of depletion zone is 120 V, 100 V, and 110 V for each as shown in Figure 3.16(A) (case 1), (B) (case 2), and (C) (case 3). The fastest elapsed time was found in the case 1 with the voltage configuration of 20 V for V_{LOW} and 120 V for V_{HIGH} and the lowest elapsed time was found in the case 2 with the voltage configuration of 30 V for V_{LOW} and 110 V for V_{HIGH} .

Different condition between the case 1 and case 2 only came from the fact that V_{HIGH} in case 1 was higher than V_{HIGH} in case 2. As shown in Figure 3.16(A) and (B), the separation speed of case 1 was faster than that of case 2, and the case 1 had lesser dispersion than the case 2 had. This result can be explained by conventionally known theories as mentioned in chapter 2. As the V_{HIGH} increased, electrophoretic force and electroosmotic force on Alexa 488 simultaneously increased. Therefore, each magnitude of those two forces must have been greater in the case 1 than in the case 2. The result of the case 1 revealed that the increase of the magnitude in electrophoretic force was dominant over that of the magnitude in electroosmotic force in those cases. This was evidenced by empirical phenomenon. Alexa 488

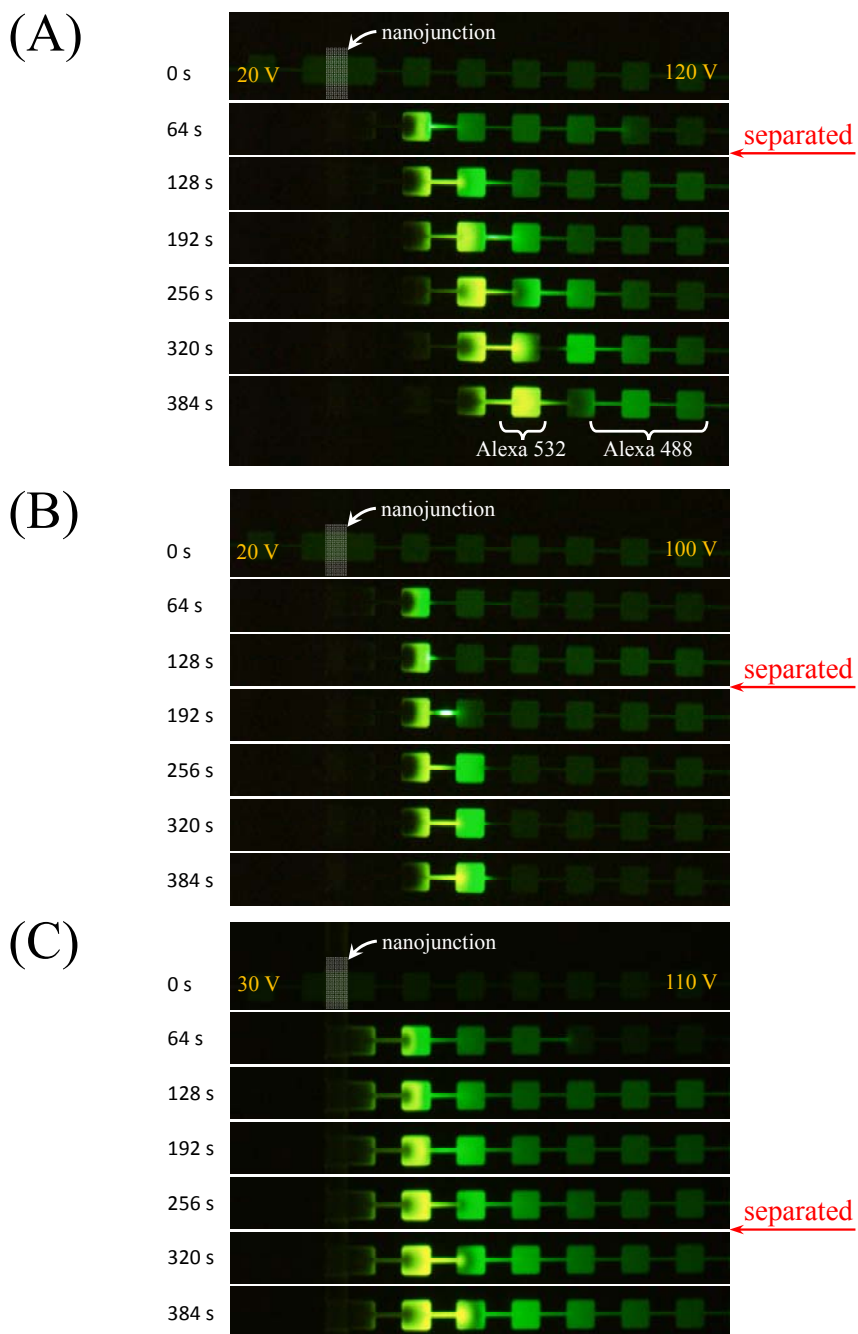


Figure 3.16 Time-lapse images of selective preconcentration of Alexa 488 and Alexa 532 with the voltage configuration of (A) V_{LOW} for 20 V, V_{HIGH} for 120 V, (B) V_{LOW} for 20 V, V_{HIGH} for 100 V and V_{LOW} for 30 V, V_{HIGH} for 110 V, respectively. The separation time of Alexa 488 from Alexa 532 takes longer in order of (A) to (C), respectively.

moved towards the reservoir with anodic electrodes faster in the case 1 than in the case 2. Consider the anodic channel as two parts divided by the location of nanojunction: a channel on V_{HIGH} side and a channel on V_{LOW} side. On the V_{HIGH} side, significantly large voltage drop occurred in depletion zone which is very short-sized region comparing to the entire length of the V_{HIGH} side. Therefore, considering average electroosmotic flow, the electroosmotic flow generated by the field on the V_{HIGH} side in the case 1 and the case 2 would not much different from each other. On the V_{LOW} side, the case 1 and the case 2 had almost the same electroosmotic flow since their values of V_{LOW} are the same. The superposition of these two flows would give similar net electroosmotic flow in the case 1 and the case 2. In this point, the movement of equilibrium position in the case 1 comparing to the case 2, according to the theory in chapter 2, resulted from the increased magnitude of electrophoretic force on molecules. Secondly, other than the location of equilibrium point, dispersion tells the dominant effect of electrophoretic force.

In the comparison of the case 2 and the case 3, however, it is not simply explained with the mechanisms mentioned in the chapter 2. In these two cases, increased V_{HIGH} led the plugs dispersed as expected, but the separation speed became, surprisingly, slowed down, which is distinct aspect from the case 1 and case 2. To investigate which results this peculiar aspect, operation map was drawn of various kinds of voltage configuration as shown in Table 3.2. Figure 3.17 describes the map of the time for Alexa 488 to separate from Alexa 532 under each V_{LOW} and V_{HIGH} according to the voltage configuration in Table 3.2. It was shown that the difference between voltages of each reservoir in anodic side did not have typical tendency other than some optimal points such as the maximum and the minimum. This can be interpreted as another evidence that the selective preconcentration occurred under nonlinear regime under ion concentration polarization system. For now, it seems to be an utmost efforts to obtain operation map and search the optimum point between separation time and the extent of dispersion if one wants to find the optimal condition

V_{LOW} [V]	V_{HIGH} [V]	Separation time [s]
20	80	252.8
	90	236.8
	100	201.6
	110	118.4
	120	86.4
30	80	224.0
	90	256.0
	100	256.0
	110	288.0
	120	256.0
40	80	224.0
	90	256.0
	100	256.0
	110	256.0
	120	224.0

Table 3.2 Separation time values of Alexa 488 from Alexa 532 in a repeated-chamber channel with different voltage configuration.

Separation time of Alexa 488 from Alexa 532

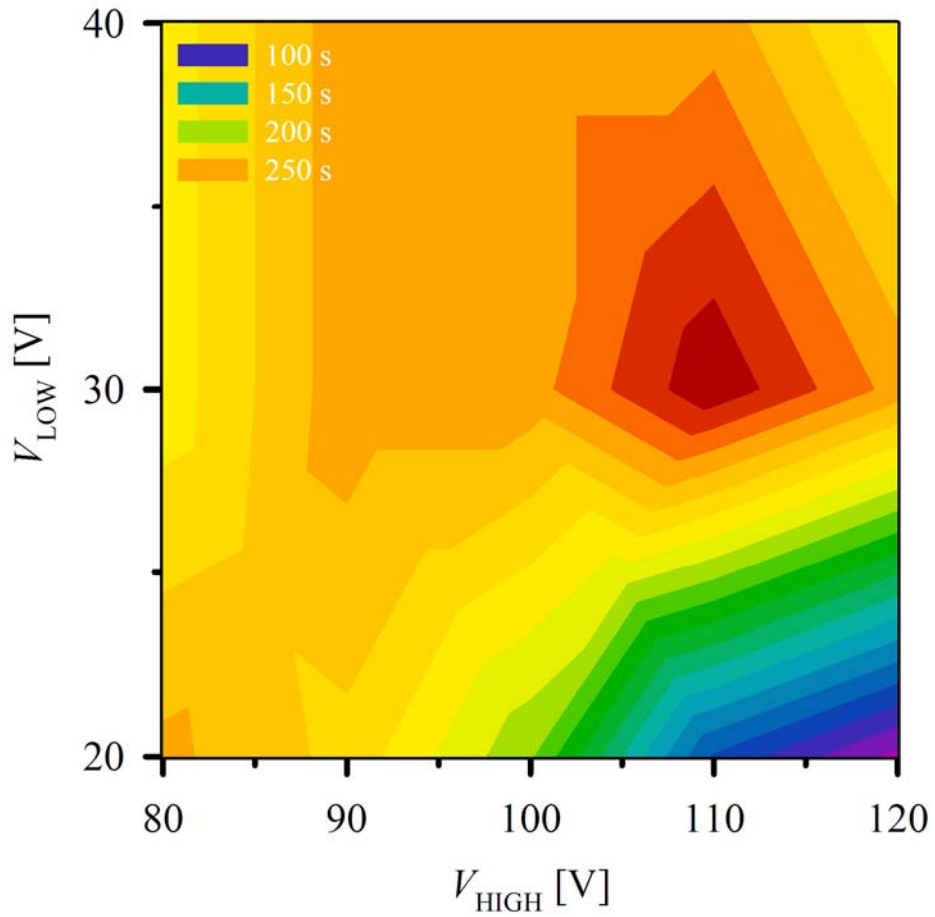


Figure 3.17 Operation map of the time for Alexa 532 to separate from Alexa 488 under each V_{LOW} and V_{HIGH} . There exists the maximum point and the minimum point.

for efficient separation.

3.2.7 Mobility-dependent preconcentration dynamics

Considering the aspect of separation as shown in Figure 3.6 and Figure 3.16(B), it is evident that the preconcentrated location kept moving after enough time scale for the development of ion depletion zone. If only electroosmotic force and electrophoretic force are effective on the separation, two different molecules must have been preconcentrated at different location. However, the results above all showed that the preconcentration of different dyes occurred at the same location and one of them was separated later over time. To figure out unknown factor which can determine the equilibrium point of selective preconcentration, we adopted a simple device with a straight channel as shown in Figure 3.18.

It was found that preconcentrated molecules interact with each other and this interaction affects the separation of the preconcentrated plugs. Figure 3.19 describes this phenomenon. SRB and Alexa 532 were used for confirming this mechanism in 1mM KCl solution. 15 V was applied for low voltage and 30 V was applied for high voltage. As denoted in Figure 3.19(A) and (B), each preconcentrated plug had its own equilibrium point over time. Also, SRB began to preconcentrate right next to the depletion zone and was stacked over time while the preconcentration plug of Alexa 532 propagates to the reservoir of high voltage side. When these two dyes were mixed in a solution and preconcentrated under ICP as denoted in Figure 3.19(C), SRB was preconcentrated as it was in Figure 3.19(A). However, Alexa 532 appeared in a different way. Comparing to the preconcentration in Figure 3.19(B), Alexa 532 in a mixed solution was preconcentrated backward to the reservoir with high voltage. Due to the existence of SRB, it seemed that Alexa 532 was pushed away by the preconcentrated plug of SRB. Since the net electric charge of SRB is -1 and that of Alexa 532 is -2, the electrophoretic mobility of Alexa 532 is greater than that of SRB. Although this cannot explain why SRB stacks near the boundary of depletion

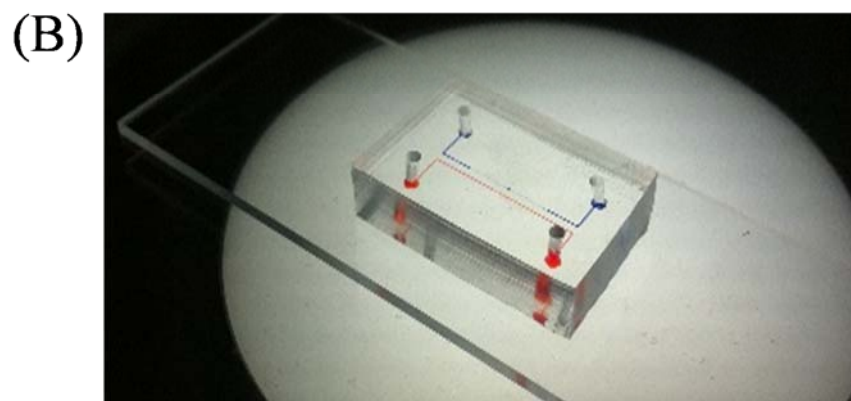
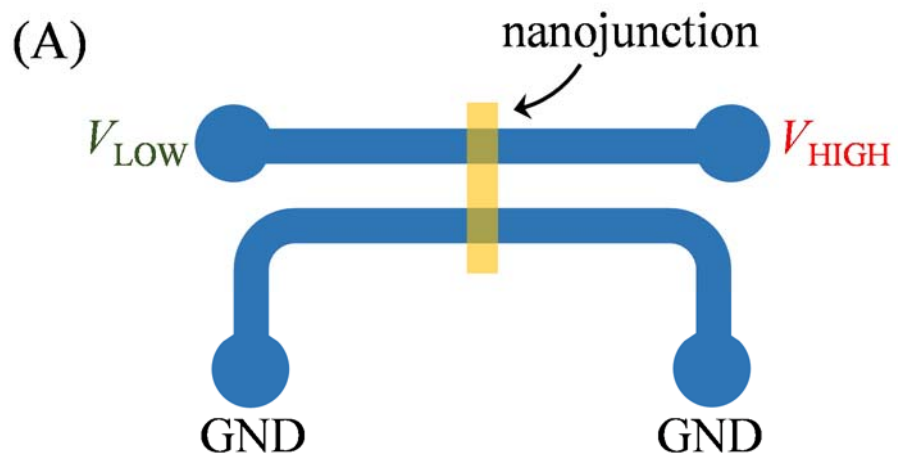


Figure 3.18 (A) Schematic of device with straight channel. The length of main channel is ~ 6 mm. (B) Microscopic view of the device with straight channel.

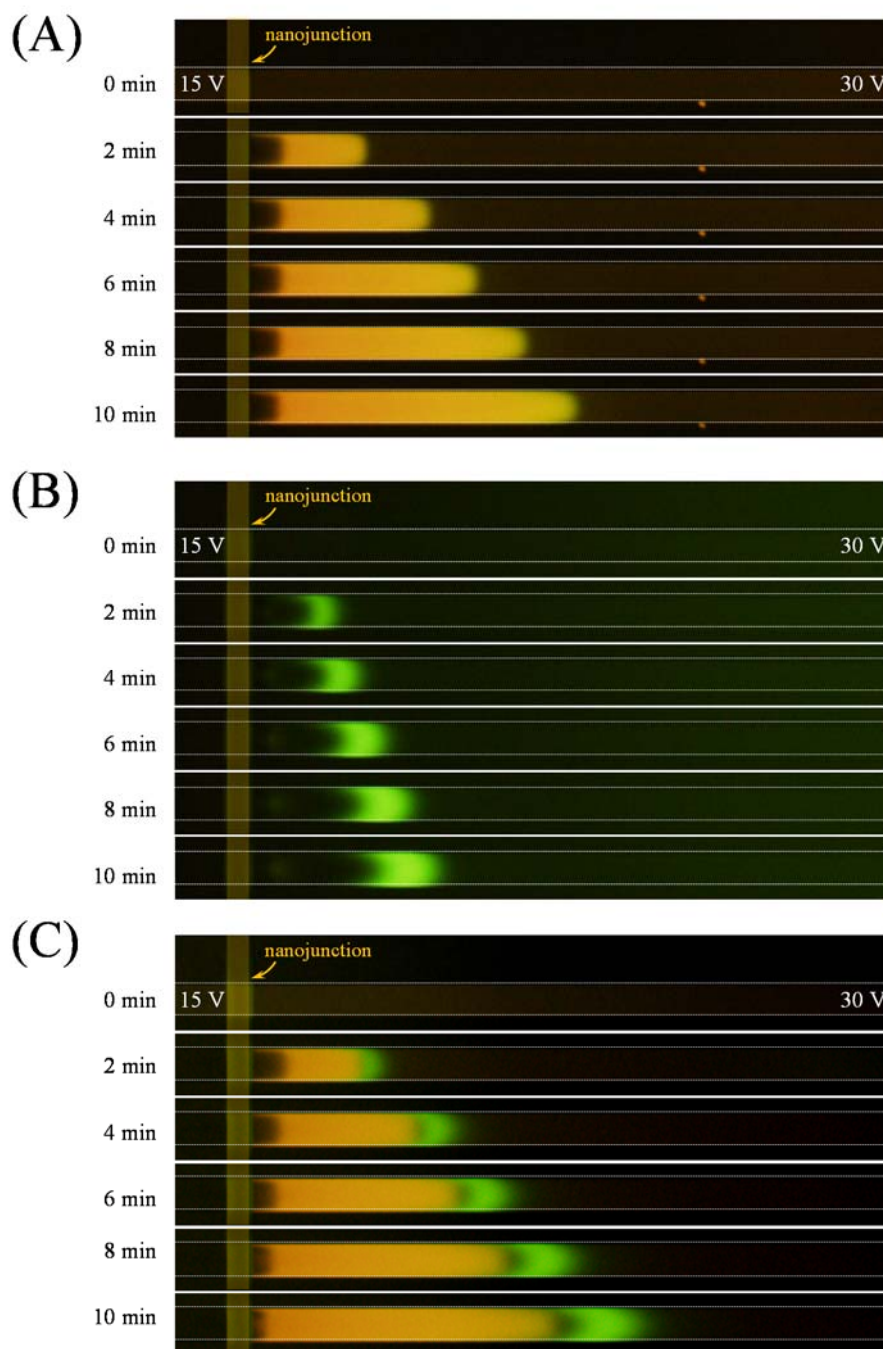


Figure 3.19 (A) Time-lapse images of selective preconcentration of (A) SRB, (B) Alexa 532 and (C) SRB and Alexa 532 together as a function of time. The location of each plug along time scale in (C) differs from that of single kind plug in (A) and (B).

zone and Alexa 532 propagates far from the depletion zone, the order of preconcentration plugs can be explained with a new model depending on electrophoretic mobility. In other words, when two different molecules are mixed and preconcentrated under ICP, molecules with different electrophoretic mobility compete with each other for satisfying local electroneutrality in order to preconcentrate at the original location which is the same location in a solution with single molecules. Over time, molecules with lower electrophoretic mobility wins molecules with higher electrophoretic mobility, and preoccupies the location near the depletion zone, expelling the molecules with higher electrophoretic mobility.

In order to investigate the new model more carefully, another dye named CoroNa Green which has neutral net electric charge was adopted. Figure 3.20(A) showed the normal preconcentration of CoroNa Green in the same condition with SRB and Alexa 532. As in SRB, this dye was also preconcentrated right next to the depletion zone and was stacked over time. Since the net charge of CoroNa Green is zero, it could be expected that SRB should lose in the competition and pushed toward the reservoir side with high voltage. In Figure 3.20(B), the experiment of mixed solution of SRB and CoroNa Green concurred with the expectation. The red image in Figure 3.20(B) only detected SRB. It can be shown in the image that CoroNa Green preoccupied the location right next to the depletion zone and pushed SRB to the reservoir side in order to satisfy the local electroneutrality.

In the light of the new model, the preconcentration of three different molecules as in Figure 3.12 can be analyzed. In the result, SRB, Alexa 532 and Alexa 488 were preconcentrated, and separated in this sequence. Considering the net charge of each dye, -1, -1, and -2, respectively, the order of Alexa 488 seems to makes sense. However, SRB and Alexa 532 were separated although their net charges are the same. When particles are polarized, the electrophoretic mobility under nonuniform electric field depends on the dipole moment of the particles.³⁴ However, the permittivities of this two dyes are smaller than that of water, which means that it is

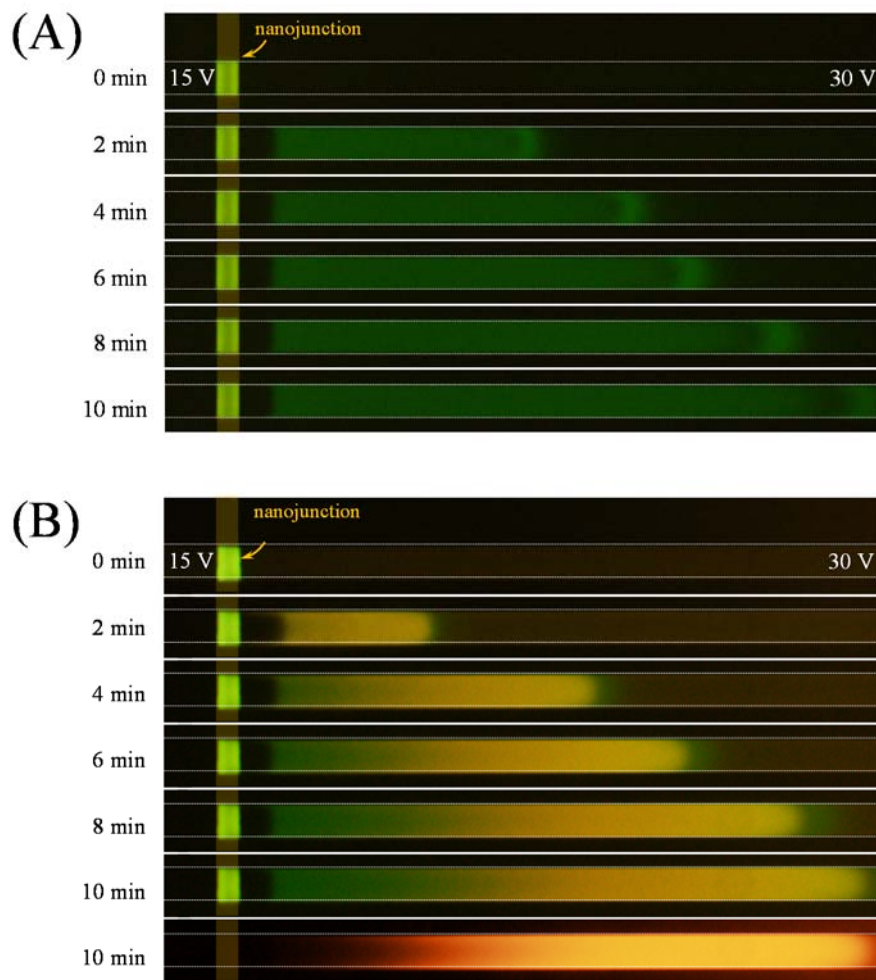


Figure 3.20 Time-lapse images of selective preconcentration of (A) CoroNa Green and (B) CoroNa Green and SRB together as a function of time. The location of each plug along time scale in (C) differs from that of single kind plug in (A) and (B).

not high enough to be effectively polarized. Therefore, the separation cannot be explained by induced charge interaction. In consideration of dielectrophoresis, dipole interaction between dye molecules can be also ignored since the size of molecules is $O(1)$ nm.³⁵ Thus, it might be caused by the nonlinear interaction between particle transport and ambient flow field.

Chapter 4

Conclusions

This thesis presented and characterized a multilayer micro/nanofluidic device for selective preconcentration. The operating principle of the device was based on the high electric field gradient induced by ICP phenomenon. In the main channel, two opposing electrophoretic force and electroosmotic drag force exerted on the charged molecules were balanced depending on the physicochemical properties of the molecules. Importantly, the repeated microchamber structure suppressed the undesirable instability of the ICP operation, pinning the location where the preconcentrated plug was formed. With this device, SRB and Alexa were simultaneously separated and preconcentrated at the separation resolution of 1.75. By introducing pneumatic microvalves, dispersion due to the high concentration gradient was prevented, and Alexa plugs preconcentrated at 100-fold was able to be isolated from the main channel without the loss of the ratio during the cyclic valve operations. After all, 30-fold of Alexa was able to be collected in the measurement window. RGB signals from the preconcentrated analytes were rigorously analyzed for quantitative and qualitative separation efficiency, while previous researches

relied only on the position tracking of the molecules. Three different dyes were also pre-concentrated and separated simultaneously. Through investigating the pre-concentration of each dye, additional mechanism for pre-concentration was revealed that interactions between different kinds of molecules affected the location of pre-concentrated plugs for satisfying local electroneutrality depending on their mobility. Given the importance of extracting selective pre-concentrated analytes, we expect that this mechanism and structure of the micro/nanofluidic device would be a powerful tool for lab on a chip applications.

Bibliography

1. Dolník, V.; Liu, S.; Jovanovich, S., Capillary electrophoresis on microchip. *Electrophoresis* **2000**, *21* (1), 41-54.
2. Jung, B.; Bharadwaj, R.; Santiago, J. G., On-chip millionfold sample stacking using transient isotachophoresis. *Analytical chemistry* **2006**, *78* (7), 2319-2327.
3. Rubinstein, I.; Shtilman, L., Voltage against current curves of cation exchange membranes. *Journal of the Chemical Society, Faraday Transactions 2: Molecular and Chemical Physics* **1979**, *75*, 231-246.
4. Kim, S. J.; Li, L. D.; Han, J., Amplified electrokinetic response by concentration polarization near nanofluidic channel. *Langmuir* **2009**, *25* (13), 7759-7765.
5. Song, H.; Wang, Y.; Garson, C.; Pant, K., Nafion-film-based micro–nanofluidic device for concurrent DNA preconcentration and separation in free solution. *Microfluidics and nanofluidics* **2014**, *17* (4), 693-699.
6. Kim, S. J.; Wang, Y.-C.; Lee, J. H.; Jang, H.; Han, J., Concentration polarization and nonlinear electrokinetic flow near a nanofluidic channel. *Physical review letters* **2007**, *99* (4), 044501.
7. Kim, S. J.; Ko, S. H.; Kwak, R.; Posner, J. D.; Kang, K. H.; Han, J., Multi-vortical flow inducing electrokinetic instability in ion concentration polarization layer. *Nanoscale* **2012**, *4* (23), 7406-7410.
8. Chen, C.-H.; Sarkar, A.; Song, Y.-A.; Miller, M. A.; Kim, S. J.; Griffith, L. G.; Lauffenburger, D. A.; Han, J., Enhancing protease activity assay in droplet-based

- microfluidics using a biomolecule concentrator. *Journal of the American Chemical Society* **2011**, *133* (27), 10368-10371.
9. Santiago, J. G., Thousandfold signal increase using field-amplified sample stacking for on-chip electrophoresis. *Electrophoresis* **2003**, *24*, 3476-3483.
 10. Kohlheyer, D.; Besselink, G. A.; Schlautmann, S.; Schasfoort, R. B., Free-flow zone electrophoresis and isoelectric focusing using a microfabricated glass device with ion permeable membranes. *Lab on a Chip* **2006**, *6* (3), 374-380.
 11. Cheow, L. F.; Sarkar, A.; Koltitz, S.; Lauffenburger, D.; Han, J., Detecting kinase activities from single cell lysate using concentration-enhanced mobility shift assay. *Analytical chemistry* **2014**, *86* (15), 7455-7462.
 12. Wang, Y.-C.; Han, J., Pre-binding dynamic range and sensitivity enhancement for immuno-sensors using nanofluidic preconcentrator. *Lab on a Chip* **2008**, *8* (3), 392-394.
 13. (a) Auroux, P.-A.; Iossifidis, D.; Reyes, D. R.; Manz, A., Micro total analysis systems. 2. Analytical standard operations and applications. *Analytical chemistry* **2002**, *74* (12), 2637-2652; (b) Reyes, D. R.; Iossifidis, D.; Auroux, P.-A.; Manz, A., Micro total analysis systems. 1. Introduction, theory, and technology. *Analytical chemistry* **2002**, *74* (12), 2623-2636.
 14. Lin, C.-C.; Hsu, J.-L.; Lee, G.-B., Sample preconcentration in microfluidic devices. *Microfluidics and nanofluidics* **2011**, *10* (3), 481-511.
 15. Kim, S. J.; Song, Y.-A.; Han, J., Nanofluidic concentration devices for biomolecules utilizing ion concentration polarization: theory, fabrication, and applications. *Chemical Society Reviews* **2010**, *39* (3), 912-922.
 16. Kim, P.; Kim, S. J.; Han, J.; Suh, K. Y., Stabilization of ion concentration polarization using a heterogeneous nanoporous junction. *Nano letters* **2009**, *10* (1), 16-23.
 17. (a) Ko, S. H.; Kim, S. J.; Cheow, L. F.; Li, L. D.; Kang, K. H.; Han, J., Massively parallel concentration device for multiplexed immunoassays. *Lab on a Chip* **2011**,

- II* (7), 1351-1358; (b) Green, Y.; Shloush, S.; Yossifon, G., Effect of geometry on concentration polarization in realistic heterogeneous permselective systems. *Physical Review E* **2014**, *89* (4), 043015; (c) Green, Y.; Yossifon, G., Effects of three-dimensional geometric field focusing on concentration polarization in a heterogeneous permselective system. *Physical Review E* **2014**, *89* (1), 013024; (d) Nam, S.; Cho, I.; Heo, J.; Lim, G.; Bazant, M. Z.; Moon, D. J.; Sung, G. Y.; Kim, S. J., Experimental Verification of Overlimiting Current by Surface Conduction and Electro-Osmotic Flow in Microchannels. *Physical review letters* **2015**, *114* (11), 114501.
18. Cho, I.; Sung, G. Y.; Kim, S. J., Overlimiting current through ion concentration polarization layer: hydrodynamic convection effects. *Nanoscale* **2014**, *6* (9), 4620-4626.
19. (a) Jia, M.; Kim, T., Multiphysics Simulation of Ion Concentration Polarization Induced by a Surface-Patterned Nanoporous Membrane in Single Channel Devices. *Analytical chemistry* **2014**, *86* (20), 10365-10372; (b) Jia, M.; Kim, T., Multiphysics Simulation of Ion Concentration Polarization Induced by Nanoporous Membranes in Dual Channel Devices. *Analytical chemistry* **2014**, *86* (15), 7360-7367.
20. (a) Unger, M. A.; Chou, H.-P.; Thorsen, T.; Scherer, A.; Quake, S. R., Monolithic microfabricated valves and pumps by multilayer soft lithography. *Science* **2000**, *288* (5463), 113-116; (b) Hong, J. W.; Studer, V.; Hang, G.; Anderson, W. F.; Quake, S. R., A nanoliter-scale nucleic acid processor with parallel architecture. *Nature biotechnology* **2004**, *22* (4), 435-439.
21. (a) Russel, W. B.; Saville, D. A.; Schowalter, W. R., *Colloidal dispersions*. Cambridge university press: 1992; (b) Schoch, R. B.; Han, J.; Renaud, P., Transport phenomena in nanofluidics. *Reviews of Modern Physics* **2008**, *80* (3), 839.
22. (a) Rubinstein, I.; Zaltzman, B., Electro-osmotically induced convection at a

- permselective membrane. *Physical Review E* **2000**, 62 (2), 2238; (b) Dydek, E. V.; Zaltzman, B.; Rubinstein, I.; Deng, D.; Mani, A.; Bazant, M. Z., Overlimiting current in a microchannel. *Physical review letters* **2011**, 107 (11), 118301.
23. Kim, S. J.; Ko, S. H.; Kang, K. H.; Han, J., Direct seawater desalination by ion concentration polarization. *Nature Nanotechnology* **2010**, 5 (4), 297-301.
24. Levich, V. G.; Technica, S., *Physicochemical hydrodynamics*. Prentice-hall Englewood Cliffs, NJ: 1962; Vol. 689.
25. Wang, Y.-C.; Stevens, A. L.; Han, J., Million-fold preconcentration of proteins and peptides by nanofluidic filter. *Analytical chemistry* **2005**, 77 (14), 4293-4299.
26. Lee, S.-H.; Lee, H.; Jin, T.; Park, S.; Yoon, B. J.; Sung, G. Y.; Kim, K.-B.; Kim, S. J., Sub-10 nm transparent all-around-gated ambipolar ionic field effect transistor. *Nanoscale* **2015**, 7 (3), 936-946.
27. Masliyah, J. H.; Bhattacharjee, S., *Electrokinetic and colloid transport phenomena*. John Wiley & Sons: 2006.
28. Kirby, B. J.; Hasselbrink, E. F., Zeta potential of microfluidic substrates: 2. Data for polymers. *Electrophoresis* **2004**, 25 (2), 203-213.
29. Lee, J. H.; Cosgrove, B. D.; Lauffenburger, D. A.; Han, J., Microfluidic concentration-enhanced cellular kinase activity assay. *Journal of the American Chemical Society* **2009**, 131 (30), 10340-10341.
30. Giddings, J. C., *Unified Separation Science* John Wiley & Sons. *New York* **1991**, 189.
31. Cheow, L. F.; Han, J., Continuous signal enhancement for sensitive aptamer affinity probe electrophoresis assay using electrokinetic concentration. *Analytical chemistry* **2011**, 83 (18), 7086-7093.
32. (a) Happel, J.; Brenner, H., *Low Reynolds number hydrodynamics - with special applications to particulate media*. **1983**; (b) Sangae, K.; Seppo, J. K., *Microhydrodynamics: Principles and Selected Applications*. In *Dover Publications*, 2013.

33. Druzgalski, C.; Andersen, M.; Mani, A., Direct numerical simulation of electroconvective instability and hydrodynamic chaos near an ion-selective surface. *Physics of Fluids (1994-present)* **2013**, *25* (11), 110804.
34. Squires, T. M.; Bazant, M. Z., Induced-charge electro-osmosis. *Journal of Fluid Mechanics* **2004**, *509*, 217-252.
35. (a) Jones, T. B.; Jones, T. B., *Electromechanics of particles*. Cambridge University Press: 2005; (b) Yoon, B. J., Electrophoretic motion of spherical particles with a nonuniform charge distribution. *Journal of colloid and interface science* **1991**, *142* (2), 575-581.

국문 초록

이온 분극 현상을 이용하여 물리화학적 성질이 다른 전하를 띤 입자를 선택적 분리 및 농축, 압출하는 다중층 마이크로/나노수력학 장치를 제시하였다. 입자에 대한 전기삼투 마찰 힘과 전기 영동 힘의 균형을 이용하여 sulforhodamine B와 Alexa Fluor 488 형광물질이 섞인 샘플을 높은 농도로 선택적으로 농축하였다. 반복적으로 연결된 마이크로챔버 구조의 마이크로채널은 형광입자를 원하는 위치로의 농축을 가능하게 하였다. 농축된 물질의 칩(chip) 상의 혹은 칩 외부에서의 연속적인 사용을 위하여, 마이크로 공압밸브가 결합되었고, 주기적인 밸브 작동을 통하여 원하는 입자만 선택적으로 압출할 수 있었다. 이러한 통합 시스템을 이용하여 sulforhodamine B가 섞인 수용액으로부터 Alexa Fluor 488이 압출되었고, 1.75의 분리 분해능과 30배의 농축비를 달성하였다. 또한 ICP 현상으로 일어나는 농축 매커니즘을 탐구하여 모빌리티에 따른 분자간 부분적 전기중성을 만족하고자하는 상호작용이 농축 플러그의 위치에 영향을 미친다는 것을 밝혀내었다. 본 장치는 랩온어칩(Lab on a chip)의 응용에 있어 향후 중요한 요소로서 역할을 할 것이라 예상된다.

주요어 : 선택적 농축, 이온선택성 투과막, 이온분극현상, 마이크로 공압 밸브, 나노전기수력학

학번 : 2014-21644



저작자표시-비영리-변경금지 2.0 대한민국

이용자는 아래의 조건을 따르는 경우에 한하여 자유롭게

- 이 저작물을 복제, 배포, 전송, 전시, 공연 및 방송할 수 있습니다.

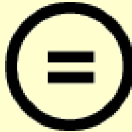
다음과 같은 조건을 따라야 합니다:



저작자표시. 귀하는 원저작자를 표시하여야 합니다.



비영리. 귀하는 이 저작물을 영리 목적으로 이용할 수 없습니다.



변경금지. 귀하는 이 저작물을 개작, 변형 또는 가공할 수 없습니다.

- 귀하는, 이 저작물의 재이용이나 배포의 경우, 이 저작물에 적용된 이용허락조건을 명확하게 나타내어야 합니다.
- 저작권자로부터 별도의 허가를 받으면 이러한 조건들은 적용되지 않습니다.

저작권법에 따른 이용자의 권리는 위의 내용에 의하여 영향을 받지 않습니다.

이것은 [이용허락규약\(Legal Code\)](#)을 이해하기 쉽게 요약한 것입니다.

[Disclaimer](#)

M.S. THESIS

NANOELECTROKINETIC SELECTIVE
PRECONCENTRATION OF CHARGED
MOLECULES AND ITS DYNAMICS

전하를 띤 입자의 나노전기동역학적 선택적 농축 및
역학 관계

BY

JIHYE CHOI

FEBRUARY 2016

DEPARTMENT OF ELECTRICAL AND COMPUTER ENGINEERING
COLLEGE OF ENGINEERING
SEOUL NATIONAL UNIVERSITY

NANOELECTROKINETIC
SELECTIVE PRECONCENTRATION
OF CHARGED MOLECULES AND ITS
DYNAMICS

지도교수 김 성 재

이 논문을 공학석사 학위논문으로 제출함

2015 년 11 월

서울대학교 대학원

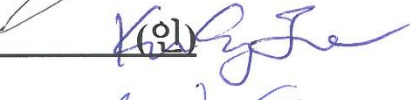
전기정보 공학부

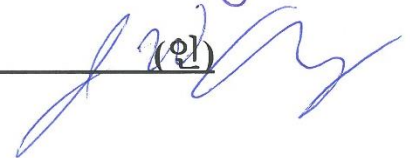
최 지 혜

최지혜의 공학석사 학위논문을 인준함

2016 년 2 월

위 원 장 이 종 호 (인) 

부위원장 김 성 재 (인) 

위 원 홍 종 욱 (인) 

Abstract

NANOELECTROKINETIC SELECTIVE PRECONCENTRATION OF CHARGED MOLECULES AND ITS DYNAMICS

JIHYE CHOI

DEPARTMENT OF ELECTRICAL AND
COMPUTER ENGINEERING

COLLEGE OF ENGINEERING

SEOUL NATIONAL UNIVERSITY

A multilayer micro/nanofluidic device was presented for the selective preconcentration and online collection of charged molecules with different physicochemical properties based on ion concentration polarization phenomena (ICP). With a balance of electroosmotic drag force and electrophoretic force on the molecules, a sample mixture of sulforhodamine B and Alexa Fluor 488 could be highly preconcentrated and separated simultaneously. A repeated microchamber structure was employed to capture each dye at a desirable position. For subsequent on-chip or off-chip application, pneumatic microvalves were integrated and selectively collected the target dyes with cyclic valve operations. Using the integrated system, Alexa Fluor 488 was solely collected (with a separation resolution of 1.75) out of the mixture at a 30-fold preconcentration ratio. Furthermore,

investigating the mechanism of preconcentration under ICP revealed that molecular interactions affected the location of preconcentrated plugs for satisfying local electroneutrality depending on their mobility. This integrated device would be a key component for lab on a chip applications.

Keywords : selective preconcentration, permselective membrane, ion concentration polarization, micro pneumatic valve, nanoelectrokinetics

Student Number : 2014-21644

Contents

Abstract	i
Contents	iii
List of Tables	v
List of Figures	vi
Chapter 1. Introduction	1
Chapter 2. Theoretical background	8
2.1 Characteristics of ICP phenomenon	8
2.2 Conventional models for ion concentration polarization	10
2.3 Simple model for preconcentration based on force balance	16
2.3.1 Preconcentration at the boundary of depletion zone	16
2.3.2 Simultaneous separation and preconcentration	19
Chapter 3. Selective preconcentration with micro pneumatic valve system	21
3.1 Experimental setup	21

3.1.1 Strategies for selective preconcentration and online collection	21
3.1.2 Preparation of PDMS microchips	26
3.1.3 Materials and reagents	29
3.1.4 System operation method	32
3.2 Results and discussions	34
3.2.1 Demonstration of selective preconcentration	34
3.2.2 Stabilization of selective preconcentration	37
3.2.3 Quantitative analysis for separation and preconcentration efficiency	37
3.2.4 Collection of preconcentrated plugs by valve system	40
3.2.5 Three kinds of analyte	46
3.2.6 Correlation between voltage configuration and separation time	52
3.2.7 Mobility-dependent preconcentration dynamics	57
Chapter 4. Conclusion and Future Work	63
Bibliography	65
Abstract in Korean	70

List of Tables

Table 3.1 Chemical and physical properties of Sulforhodamine B, Alexa Fluor 488, Alexa Fluor 532, and CoroNa Green.	22
Table 3.2 Separation time values of Alexa 488 from Alexa 532 in a repeated-chamber channel with different voltage configuration.	22

List of Figures

- Figure 1.1** (A) Capillary electrophoresis chip design¹ and (B) Schematic of on-chip Field-amplified sample stacking in the absence of Electroosmotic force. Gray shading is used to show conductivity field, with lighter shading corresponding to low-conductivity buffer.⁹.....22
- Figure 1.2** (A) Schematic of isotachopheresis and capillary electrophoresis assay protocol.² (B) Free-flow zone electrophoresis of fluorescein and rhodamine B. Potential was not applied in a) and 250 V cm⁻¹ across the separation area.¹⁰.....22
- Figure 1.3** (A) Fluorescence snapshots of DNA versus time. The fluorescence intensity increases with time, indicating concentration of the DNA sample. The exclusion zone moves away from the Nafion film interface (shown in dashed white lines) due to the dynamic equilibration process of ICP.⁵ (B) The phosphorylated substrates and the unphosphorylated substrates are simultaneously preconcentrated and separated.¹¹.....22
- Figure 1.4** (A) Schematic representation of the integrated nanofluidic biomolecule concentrator and microfluidic droplet generator chip. The enzyme molecules were accumulated by a concentrator into a plug that was mixed with the substrate and then encapsulated into monodisperse microdroplets for time-dependent observation. The reaction to turn over the fluorogenic substrate was monitored as a function of time in the

droplets.⁸ (B) Immunosensing using preconcentration under ion concentration polarization procedure. One can locally increase the sample concentration and facilitate the binding kinetics and the sensitivity without changing the binding pair or detection system.¹²...22

Figure 2.1 (A) Schematic configuration of micro-nano hybrid device for ion concentration polarization phenomenon and (B) Schematic diagram of ion concentration distribution near cation-selective membrane.....22

Figure 2.2 (A) The basic ion-enrichment and ion-depletion behavior and (B) characteristic curve of voltage against ionic current of a cation-exchange membrane, showing ohmic, limiting, and overlimiting regime⁶.....22

Figure 2.3 In situ measurement of local electric field inside an outside the ion depletion zone using microelectrodes integrated along the microchannel.⁴.....22

Figure 2.4 (A) The linear velocity and angular velocity of the vortex as a function of applied voltage. (B) Fast vortex at steady state in single gate device. (C) Four independent strong vortices in double gate device.⁶.....22

Figure 2.5 Schematic diagrams of the concentration profile inside ICP layer and ohmic/limiting/overlimiting current behavior when (A) only diffusion and drift were considered, (b) electroconvection was added to (A) and (C) multiple vortices were formed (inducing step-wise discrete concentration distribution).⁷.....22

Figure 2.6 The effect of bulk charge.³ (A) Calculated voltage against current curves for different values of parameter e where i_L is each limiting current. The zero value of e corresponds to the classical theory. (B) Calculated ion concentration profiles at different voltages V for $e = 10^{-4}$. Solid lines represents cation concentration at dimensionless voltage V while dashed lines do anion concentration.....22

Figure 2.7 (A) Preconcentration at the boundary of depletion zone and (B) schematic

of microchannel and nanojunction represented by resistors, where I denotes current, c denotes ion concentration, σ denotes conductance, and E denotes electric field.22

Figure 2.8 Schematic diagram of selective preconcentration mechanism with different mobility. The separation was drawn by the equilibrium between electroosmotic drag force and electrophoretic force exerted on molecules.22

Figure 3.1 Preconcentration operation in (A) straight microchannel, (B) funnel microchannel and (C) narrow microchannel.22

Figure 3.2 Numerically simulated ICP layer for (A) concentration distribution, (B) electrical field and (C) flow field. (D) Schematic illustration for electric potential near the microchamber.22

Figure 3.3 (A) Microscopic view of the selective preconcentration device. The microchannels in the ICP layer were indicated with blue and the microchannels in the valve layer were indicated red. (B) An exploded view of the device with (i) a valve layer, (ii) an ICP layer and (iii) a Nafion patterned slide glass. (C) Assembled multilayered online selective preconcentration device.22

Figure 3.4 Chemical structure of (A) Sulforhodamine B, (B) Alexa Fluor 488, (C) Alexa Fluor 532, and (D) CoroNa Green.22

Figure 3.5 Microscopic images of 3-step valve control sequence: Step1 - ICP preconcentration to form a highly concentration plug, Step 2 - isolation of a highly preconcentrated plug at specific microchamber, and Step 3 - collection of the highly preconcentrated plug into upward channel.22

Figure 3.6 Time-lapse images of selective preconcentration of SRB and Alexa 488. High Concentration ratio was represented by the brightness of fluorescence. Since the physicochemical properties of two dyes were different, they were preconcentrated at different locations.22

- Figure 3.7** Overall fluorescence intensity tracked in each microchamber as a function of time. Dotted line, dashed line and solid line represented the mixture of SRB with Alexa 488, only SRB and only Alexa 488, respectively. Three different colors indicated the pixel intensity of each microchamber (black for microchamber 1, red for microchamber 2 and blue for microchamber 3). The concentration ratio of selectively preconcentrated Alexa 488 in microchamber 3 exceeded 100-fold, maintaining the preconcentration factor high enough in repeated valve operations.22
- Figure 3.8** Red/green color profile in microchamber 3, showing the microchamber 3 only had Alexa 488.....22
- Figure 3.9** Red/green color profile in microchamber 1, showing the microchamber 1 only had SRB. Fluctuations after 30 minutes in all plots showed that the preconcentration factor maintains over 50-fold along the cyclic valve operations. While the error bars were omitted for clear visibility, the tests were conducted at least 10 times with different devices for the repeatability and reliability.....22
- Figure 3.10** Time-lapse images showing the dispersion of isolated plug when the valves were (A) OFF and (B) ON.22
- Figure 3.11** (A) Snapshots of repeated valve operations collecting selectively preconcentrated plugs. Compared to the initial state, the measurement window was being filled with green dye (Alexa 488) over several valve operations. (B) Average intensity change in the measurement window over number of repetition of valve operations. The average intensity exceeded 10-fold in a single valve operation, and 30-fold after nine operations. Note that there was no SRB in the measurement window. 22
- Figure 3.12** Time-lapse images showing the selective preconcentration of SRB, Alexa 532 and Alexa 488. Three different dyes were simultaneously

preconcentrated and separated.	22
Figure 3.13 Green pixel intensity tracked in each microchamber as a function of time with the intensity reference line of Alexa 532. A triangular marker, a rectangular marker, and a diamond marker, and x marker represent the green pixel intensity in microchamber 2, microchamber 3, microchamber 4, and microchamber 5, respectively.	22
Figure 3.14 Red pixel intensity tracked in each microchamber as a function of time with the intensity reference line of SRB. A circular marker, a triangular marker, a rectangular marker, and a diamond marker represent the red pixel intensity in microchamber 1, microchamber 2, microchamber 3, and microchamber 4, respectively.	22
Figure 3.15 Green pixel intensity tracked in each microchamber as a function of time with the intensity reference line of Alexa 488. A triangular marker, a rectangular marker, and a diamond marker, and x marker represent the green pixel intensity in microchamber 2, microchamber 3, microchamber 4, and microchamber 5, respectively.	22
Figure 3.16 Time-lapse images of selective preconcentration of Alexa 488 and Alexa 532 with the voltage configuration of (A) V_{LOW} for 20 V, V_{HIGH} for 120 V, (B) V_{LOW} for 20 V, V_{HIGH} for 100 V and V_{LOW} for 30 V, V_{HIGH} for 110 V, respectively. The separation time of Alexa 488 from Alexa 532 takes longer in order of (A) to (C), respectively.	22
Figure 3.17 Operation map of the time for Alexa 532 to separate from Alexa 488 under each V_{LOW} and V_{HIGH} . There exists the maximum point and the minimum point.	22
Figure 3.18 (A) Schematic of device with straight channel. The length of main channel is ~6 mm. (B) Microscopic view of the device with straight channel.	22
Figure 3.19 (A) Time-lapse images of selective preconcentration of (A) SRB, (B)	

Alexa 532 and (C) SRB and Alexa 532 together as a function of time. The location of each plug along time scale in (C) differs from that of single kind plug in (A) and (B).22

Figure 3.20 Time-lapse images of selective preconcentration of (A) CoroNa Green and (B) CoroNa Green and SRB together as a function of time. The location of each plug along time scale in (C) differs from that of single kind plug in (A) and (B).22

Chapter 1

Introduction

Recently, the micro Total Analysis System (mTAS) has been tremendously researched in the fields of analytical chemistry, diagnosis, environmental and nuclear engineering.¹³ The major components in such systems are a separator for multi-component analytes, a preconcentrator for the detection of low abundant molecules, and a sample collector for post processing. These on-chip preconcentration methods have been developed in order to detecting low-abundant analytes, particularly those in bio-samples. Although off-chip sample can solve this this problem prior to analysis, the amount of sample loss and contamination in sample cannot be ignored. Furthermore, the additional preparation steps before analysis are often labor-intensive and time-consuming. In this light, many on-chip sample preconcentration techniques based on different working principles for improving the detection sensitivity have been introduced and implemented in microchips for achieving the goals of automation, enhancement in analytical efficiency, and reductions in sample loss and contamination.¹⁴

A number of researches have been performed on preconcentration or separation of molecules using capillary electrophoresis,¹ microfluidic field-amplified sample stacking,⁹ isoelectric focusing,¹⁰ and isotachopheresis² as shown in Figure 1.1 and

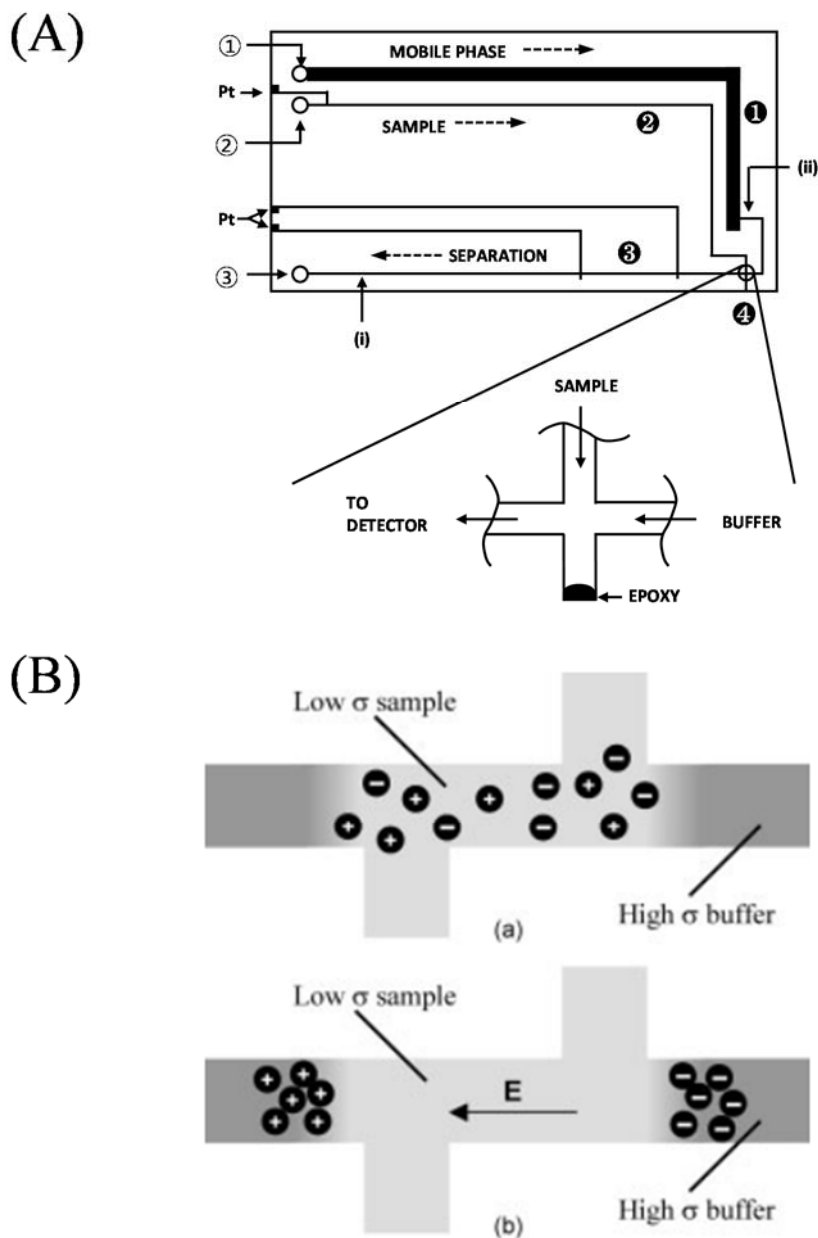


Figure 1.1 (A) Capillary electrophoresis chip design¹ and (B) Schematic of on-chip Field-amplified sample stacking in the absence of Electroosmotic force. Gray shading is used to show conductivity field, with lighter shading corresponding to low-conductivity buffer.⁹

Figure 1.2.² In practical processes, these methods have several difficulties; (1) these methods require the additional extraction system of pre-concentrated and separated molecules because they employ free flow concept (i.e. the target compounds are migrating and concentrating simultaneously along the specific path where the background fluid is flowing.), limiting subsequent processes. (2) Alternating injection of samples that should be isolated one another causes considerable cross contaminations. (3) While the reliability of detection level is enhanced by increasing the concentration of samples, intricate channel geometries or specific chemicals are often demanded for an experimental setting. (4) Even after successful separation and pre-concentration, online detection followed by these operations can still cause an inevitable dispersion. These problems tend to increase complexity of operations or produce false negative and false positive, resulting in unfeasible on-chip processes. Therefore, a new design with simple structure and easy fabrication is demanded for performing fast and accurate separation and pre-concentration. Furthermore, a connection to conventional off-chip analysis systems or an integration with on-chip analysis parts is expected for the ideal platform of mTAS.

As a method to pre-concentrate analytes, nanoscale electrokinetic phenomenon caused by the selective transportation of counter-ions in the electrolyte near a nanoporous membrane, called ion concentration polarization (ICP), has been suggested and the pre-concentration factor reached up to million-fold.¹⁵ The target analytes are concentrated at pinned position, while background fluid is still flowing in ICP operation. Recently, simultaneous separation and pre-concentration (or selective pre-concentration) was successfully performed using ICP, demonstrating the separation of phosphorylated and unphosphorylated substrates¹¹ or tagged and untagged DNA molecules as shown in Figure 1.3.⁵ It indirectly proved that one can utilize the ICP concept not only to pre-concentrate low abundant molecules but also to separate molecules depending on different physicochemical properties. However, these ICP demonstrations still have several limitations. (1) First of all, the

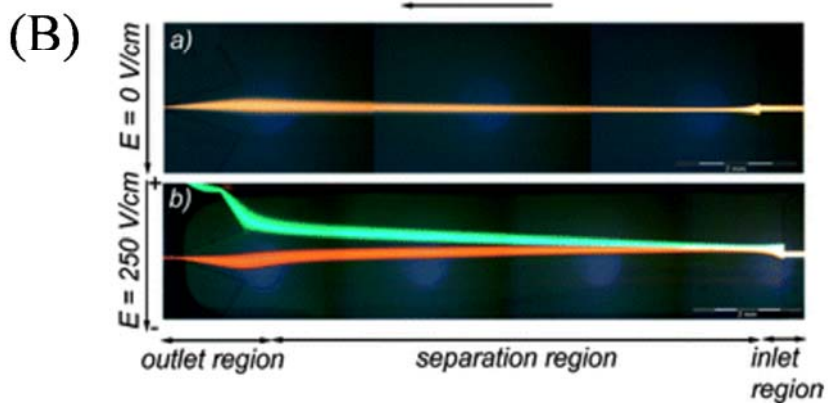
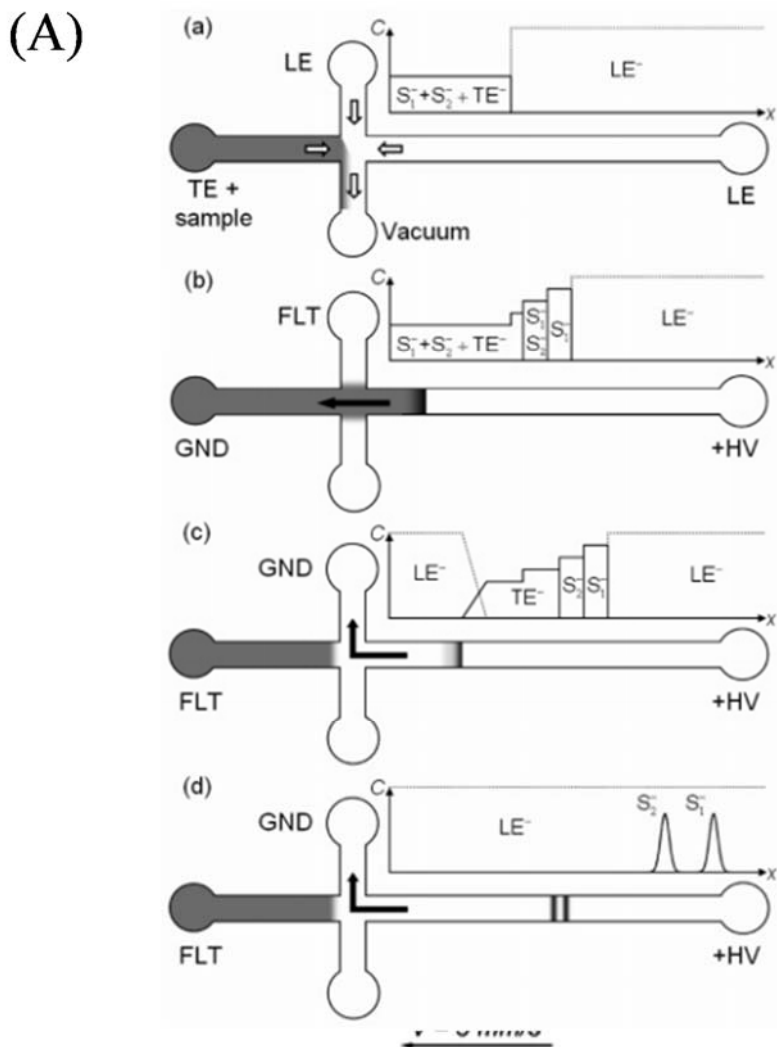


Figure 1.2 (A) Schematic of isotachopheresis and capillary electrophoresis assay protocol.² (B) Free-flow zone electrophoresis of fluorescein and rhodamine B. Potential was not applied in a) and 250 V cm^{-1} across the separation area.¹⁰

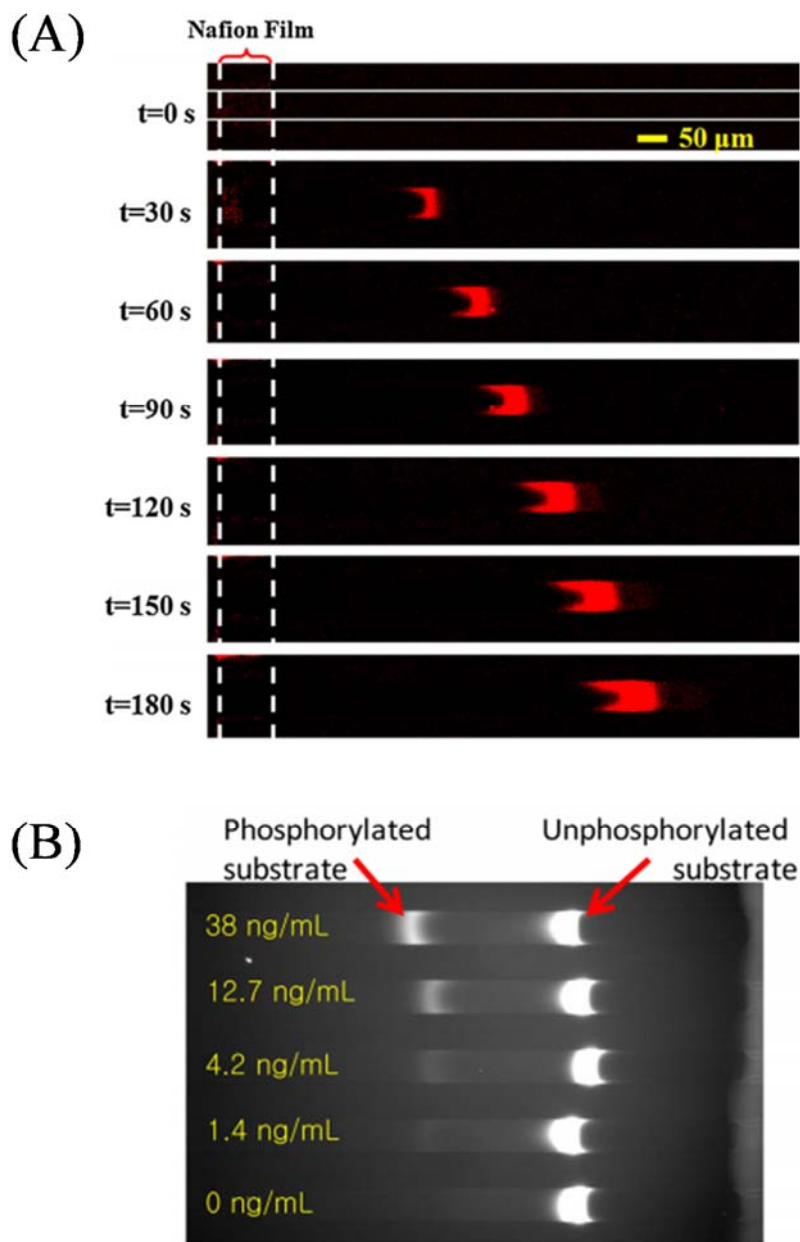


Figure 1.3 (A) Fluorescence snapshots of DNA versus time. The fluorescence intensity increases with time, indicating concentration of the DNA sample. The exclusion zone moves away from the Nafion film interface (shown in dashed white lines) due to the dynamic equilibration process of ICP.⁵ (B) The phosphorylated substrates and the unphosphorylated substrates are simultaneously preconcentrated and separated.¹¹

identification of the location where reactions occur becomes labor-intensive and time-consuming tasks since the location of preconcentrated sample plug keeps uncontrollably fluctuating by the strong instability of electrokinetic flow inside ICP layer.^{7, 16} (2) The extraction of the preconcentrated analytes for post processing without irresistible dispersion still has not been accomplished. Turning off an applied electric field let the highly preconcentrated plugs disperse quickly since there is a huge concentration gradient at the boundary. To resolve this problem, an integration with two-phase droplet generator⁸ or pre-binding on-site reaction¹² were reported as in Figure 1.4, but an additional recovery processes is needed or aggressive washing steps should be excluded, respectively. These factors significantly hinder the commercialization of further engineering developments.

To evolve ICP concept as a practical tool to selectively preconcentrate charged molecules, the integral mechanism is unprecedentedly required of (1) the stable formation of the highly preconcentrated single analyte and (2) on-demand extraction to external systems without undesirable dispersion. In this work, by designing narrow channels between repeated microchambers, the fluidic instability due to amplified electric field inside ICP was able to be suppressed. Limiting the ever-expanding ICP zone by microstructures¹⁷ or by external hydrodynamic flow injection¹⁸ have been reported to restrict the hydrodynamic instability and the role of vortices near the membrane.¹⁹ These narrow microchannels between repeated microchambers presented in this work are expected to perform in the same manner. Subsequently, pneumatic microvalve system²⁰ was employed to isolate the highly concentrated sample from the original sample mixture without further dispersion, and also to collect sample plugs so that they can be further used in conventional analytical systems in either on-chip or off- chip formats.

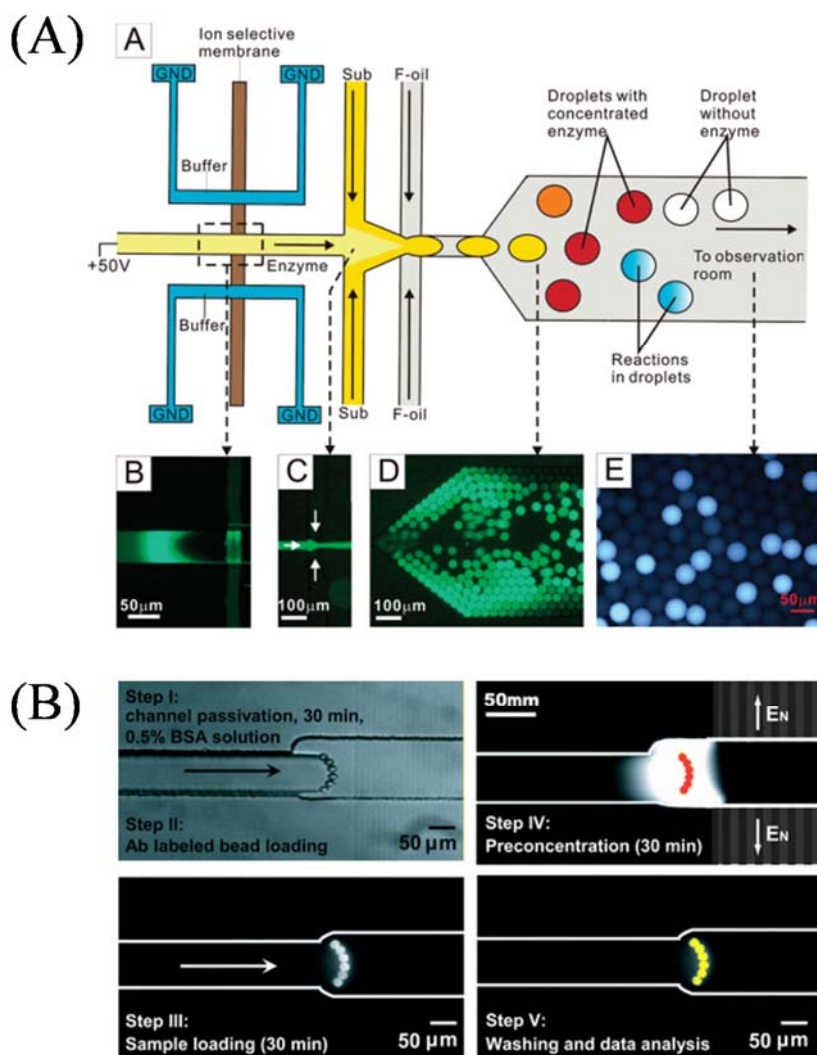


Figure 1.4 (A) Schematic representation of the integrated nanofluidic biomolecule concentrator and microfluidic droplet generator chip. The enzyme molecules were accumulated by a concentrator into a plug that was mixed with the substrate and then encapsulated into monodisperse microdroplets for time-dependent observation. The reaction to turn over the fluorogenic substrate was monitored as a function of time in the droplets.⁸ (B) Immunosensing using preconcentration under ion concentration polarization procedure. One can locally increase the sample concentration and facilitate the binding kinetics and the sensitivity without changing the binding pair or detection system.¹²

Chapter 2

Theoretical background

2.1 Characteristics of ICP phenomenon

When it comes to permselective system in ion concentration polarization phenomenon, micro-nano hybrid platform is considered as shown in Figure 2.1(A). In the platform, two microchannels are connected only with nanojunction which operates as a permselective membrane. In this work, only cation-selective membrane is discussed below under microchannel surface with negative zeta potential.

A nanochannel thinner than $O(100)$ nm has permselectivity since in that scale the thickness of Debye layer should be non-negligible and the layer even can be overlapped.²¹ As shown in Figure 2.1(B), only cations pass through cation-selective membrane towards cathodic side while anions cannot under electric field. Due to this preferential cation transport through the nanoporous membrane, ion concentration decreased in anodic side, which is called ion depletion zone, and ion concentration increased in cathodic side, which is called ion enrichment zone. The phenomenon of concentration polarization in either sides of permselective media is called as ion concentration polarization (ICP).^{6, 15} Kim *et al.* observed this phenomenon of nonlinear characteristics in current according to the applied voltage

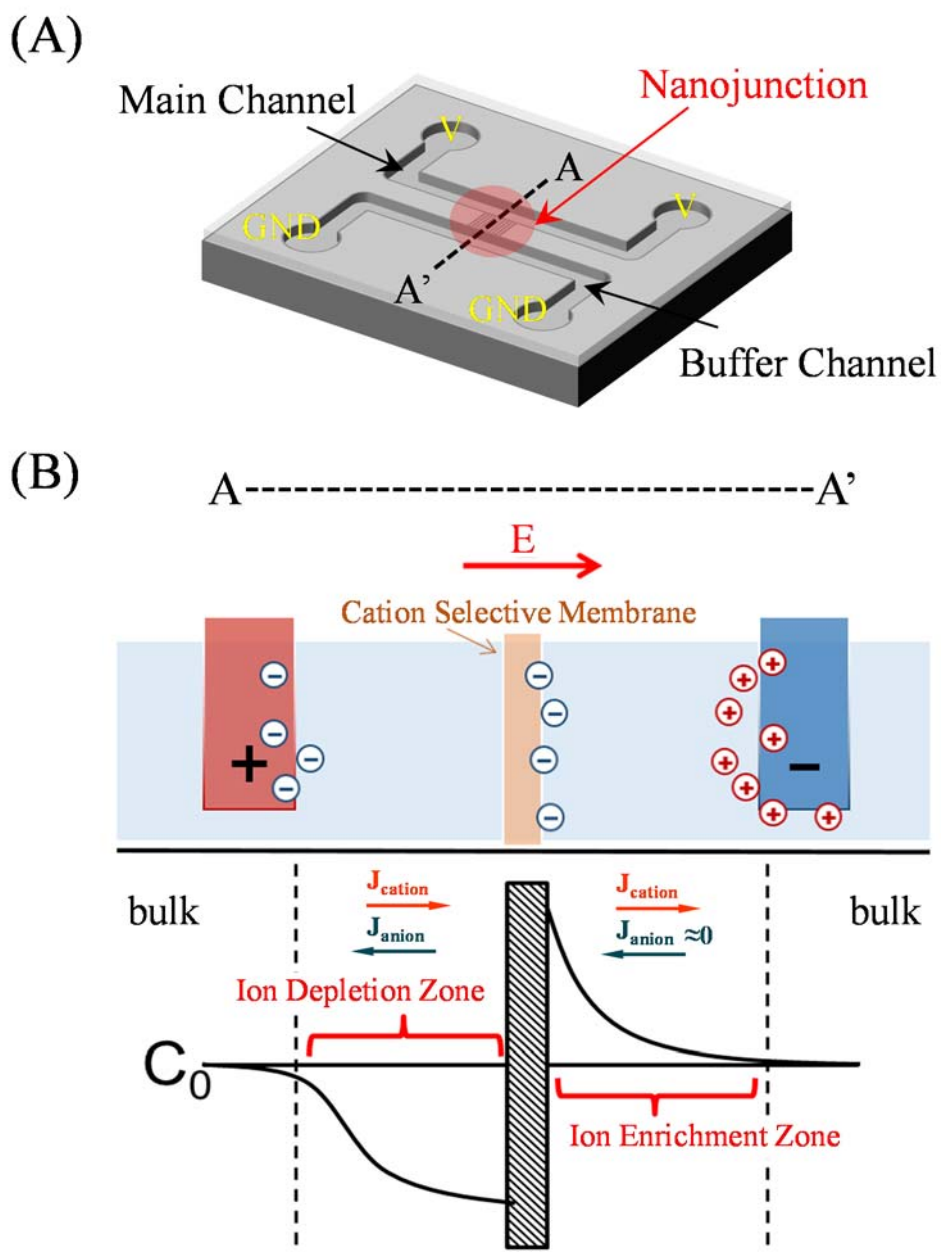


Figure 2.1 (A) Schematic configuration of micro-nano hybrid device for ion concentration polarization phenomenon and (B) Schematic diagram of ion concentration distribution near cation-selective membrane.

as shown in Figure 2.2(A) and (B). As applied voltage increases, there exists three regimes: ohmic regime in low current followed by limiting regime of a plateau with much lower slope, and overlimiting regime where the slope of current increased again but still lower than that of ohmic regime.⁶

The depletion zone, which is unique region adjacent to permselective membrane, has three distinctive properties: low ion concentrations,^{3,22} strengthened electric field intensity,⁴ and strong vortices^{6, 15, 22a} adjacent to the nanoporous membrane. As the cation selective membrane is impermeable for anions, only cations are permitted to pass through the membrane when voltage is applied. Locally broken electroneutrality in anodic side of the membrane lets anions repulse each other, forming depletion zone with ion concentration even below one hundredth of bulk concentration.^{3, 23} Due to depletion of ions as charge carriers, electrical conductivity in ion depletion zone becomes very small. Since current density should be uniform through the longitudinal direction along the microchannel, the magnitude of electric field happens to become extremely amplified. This was experimentally confirmed as denoted in Figure 2.3.⁴ In addition, strong and fast vortices are generated in depletion zone near the membrane.¹⁵ Rubinstein *et al.* theoretically suggested nonequilibrium electro-osmotic slip, at a flat permselective membrane, proportional to the square of electric field.^{22a} This relationship denotes the formation of vortices is nonlinear phenomenon. Figure 2.4(A) shows the velocity of the vortices which is at least $O(10)$ times faster than that of primary electroosmotic flow under the same electric potential. At steady state, Kim *et al.* observed fast vortices in each single and double gate device as shown in Figure 2.4(B).⁶

2.2 Conventional models for ion concentration polarization

As described in Figure 2.5(A),⁷ classical models based on Nernst-Planck equations considering ion transport only due to diffusion and electromigration predict the linear concentration profile inside the ion depletion zone.²⁴

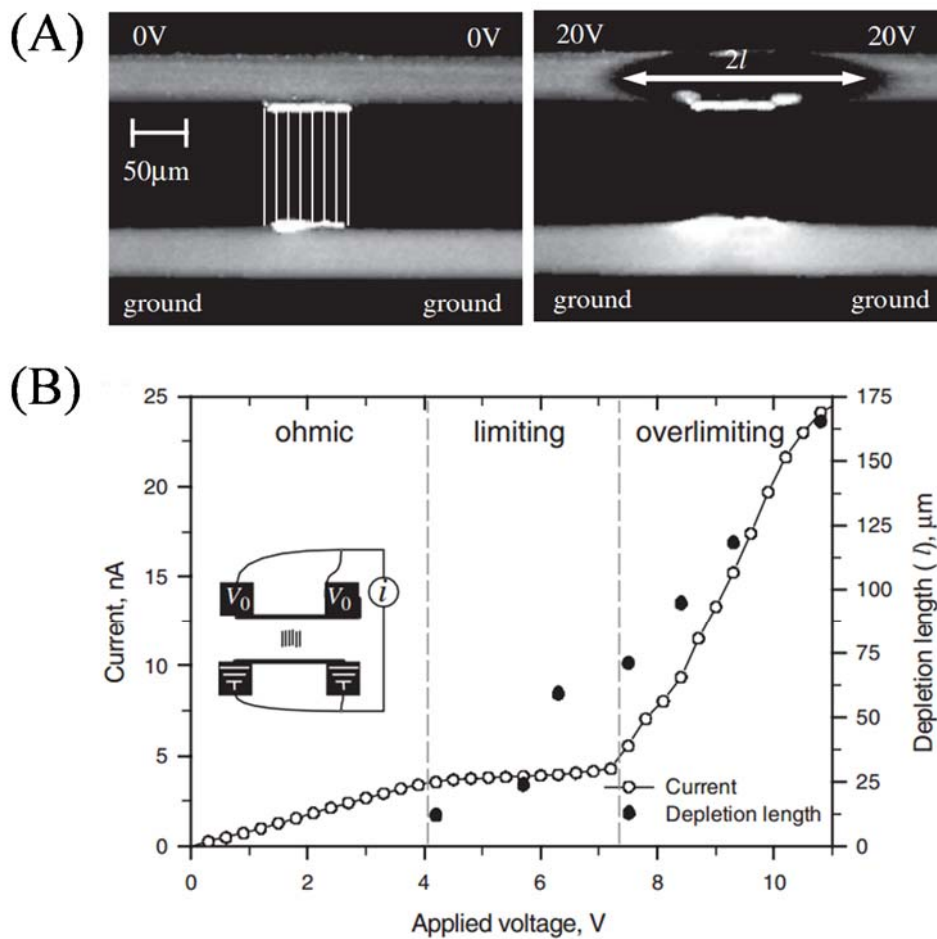


Figure 2.2 (A) The basic ion-enrichment and ion-depletion behavior and (B) characteristic curve of voltage against ionic current of a cation-exchange membrane, showing ohmic, limiting, and overlimiting regime⁶

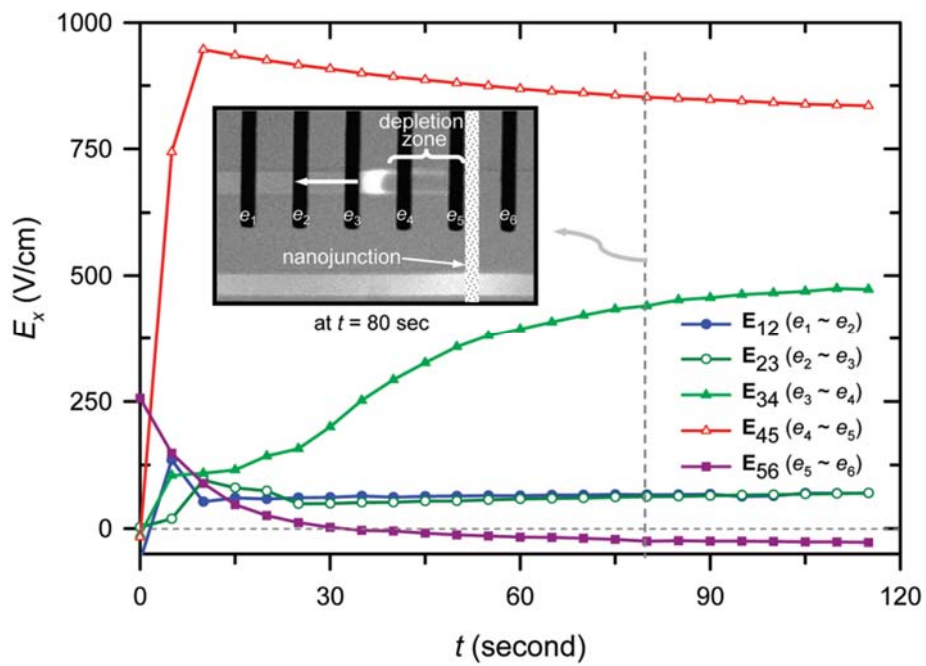


Figure 2.3 In situ measurement of local electric field inside and outside the ion depletion zone using microelectrodes integrated along the microchannel.⁴

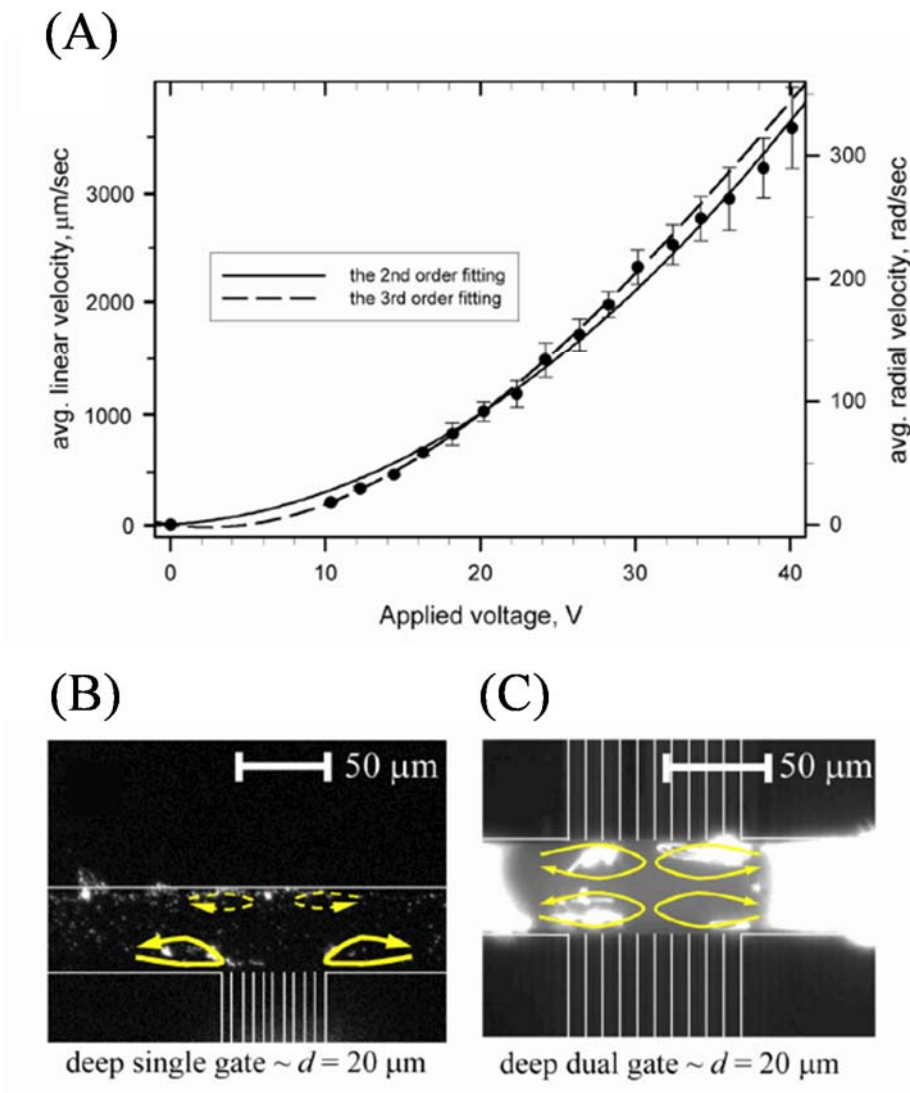


Figure 2.4 (A) The linear velocity and angular velocity of the vortex as a function of applied voltage. (B) Fast vortex at steady state in single gate device. (C) Four independent strong vortices in double gate device.⁶

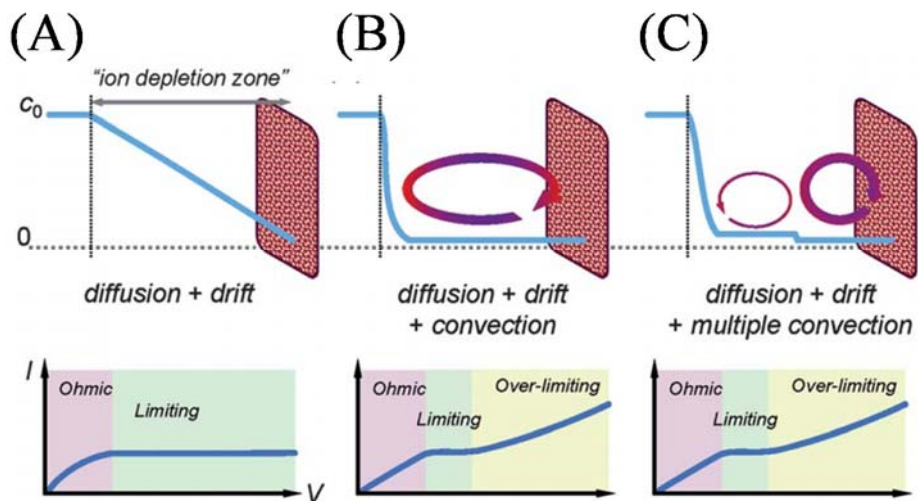


Figure 2.5 Schematic diagrams of the concentration profile inside ICP layer and ohmic/limiting/overlimiting current behavior when (A) only diffusion and drift were considered, (b) electroconvection was added to (A) and (C) multiple vortices were formed (inducing step-wise discrete concentration distribution).⁷

Tracing the connection with the classical model, Rubinstein *et al.*³ developed a model expressing overlimiting current as in Figure 2.5(B) by considering the role of bulk charge. A steady current was considered to pass through an ideally permselective membrane immersed in a stirred solution of 1:1 valent electrolyte. They assumed there is an ‘unstirred’ layer of thickness δ near the membrane, which does not depend on the magnitude of applied voltage V . Also, it was assumed that the ions within the unstirred layer are distributed by means of electrodiffusion only. Identifying the x-axis where $x = 0$ with the outer boundary of the ‘unstirred’ layer, governing equations and boundary conditions are as in the following.

$$\frac{d^2\psi}{dx^2} = -\frac{4\pi F}{\varepsilon} (c_+ - c_-) \quad (2.1)$$

$$\frac{d}{dx} \left(\frac{dc_+}{dx} + \frac{Fc_+}{RT} \frac{d\psi}{dx} \right) = 0 \quad (2.2)$$

$$\frac{d}{dx} \left(\frac{dc_-}{dx} - \frac{Fc_-}{RT} \frac{d\psi}{dx} \right) = 0 \quad (2.3)$$

$$\psi|_{x=0} = 0, \quad c_+|_{x=0} = c_-|_{x=0} = c_0 \quad (2.4)$$

$$\psi|_{x=\delta} = -V, \quad c_+|_{x=\delta} = N, \quad \left(\frac{dc_-}{dx} - \frac{Fc_-}{RT} \frac{d\psi}{dx} \right)|_{x=\delta} = 0 \quad (2.5)$$

where ψ is the electric potential, F is the Faraday constant, ε is the dielectric permittivity, c_+ and c_- is the ion concentration of each ionic species, R is the gas constant, c_0 is the bulk concentration, and N is the fixed charge concentration within the membrane. The Poisson equation is represented by equation (2.1). The Nernst-Planck equations (2.2) and (2.3) describe the mass transport of charged species under consideration of the diffusion and the electromigration. Since they assumed an ‘unstirred’ layer near the membrane, Stokes equations and continuity equation were not solved. Equation (2.4) represents the boundary condition of bulk reservoir and equation (2.5) represents the boundary condition near the cation selective membrane.

Due to the equations, the effect of bulk charge of ICP layer could be described in the overlimiting regime. In their definition, parameter δ is dimensionlessly defined by

$$\varepsilon = \frac{\lambda_D^2}{\delta^2} \quad (2.6)$$

where λ_D is the Debye length. In the Levich's model, ε is zero due to the assumption of local electroneutrality. With this zero value, ionic current becomes saturated to the limiting value as denoted in Figure 2.5(A). Considering the effect of bulk charge, ionic current could be increased beyond limiting current with different conductance comparing with ohmic regime as shown in Figure 2.6(A) and (B).

2.3 Simple model for preconcentration based on force balance

2.3.1 Preconcentration at the boundary of depletion zone

It has been known that nanofluidic channels can support ion-selective ion currents. When an electric field is applied across the nanojunction, the electrical double layer began to be overlapped in each nanojunction, letting counterions migrate across the nanojunction. This results in decrease of ion concentrations at the anodic side, generating the ion depletion zone. The ion depletion near the nanoporous membrane will thicken the Debye layer, and thus, make the layer overlap more significantly in the nanofluidic channel. This enhances ion concentration polarization. Above a certain threshold value of electric field, the ion transport across the nanojunction enters a new, nonlinear regime. In this regime, the counterions are depleted from the nanofluidic channel, and the extended space charge layer is formed near the nanojunction in the anodic bulk side. Within this induced layer, electroneutrality is locally broken and co-ions or other charged molecules are rejected to pass the depletion zone.²⁵ Meanwhile, electroosmotic flow generated by applying different voltage at each reservoir can extend the depletion zone to one side of the reservoir as shown in Figure 2.7(A). Due to electroosmotic flow, depletion zone is stretched to the reservoir with low voltage.

Negatively charged molecules are preconcentrated at the boundary of the depletion zone. As denoted in Figure 2.7(B), each part of the solution in the

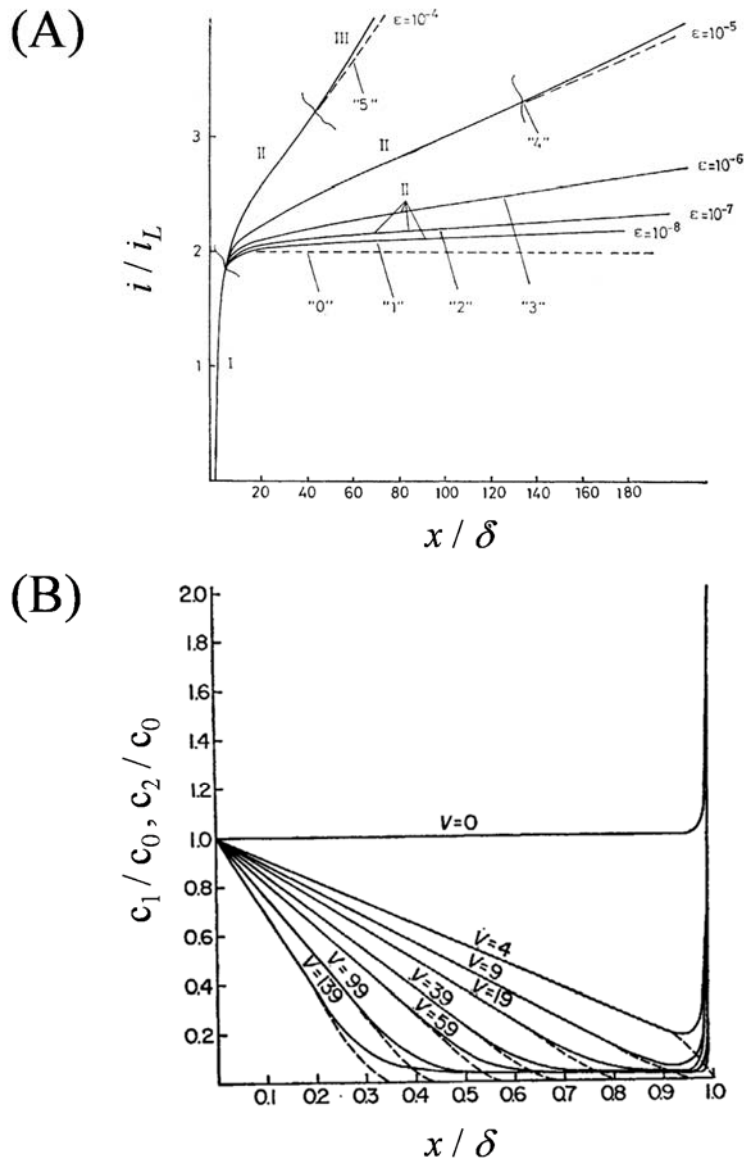


Figure 2.6 The effect of bulk charge.³ (A) Calculated voltage against current curves for different values of parameter ϵ where i_L is each limiting current. The zero value of ϵ corresponds to the classical theory. (B) Calculated ion concentration profiles at different voltages V for $\epsilon = 10^{-4}$. Solid lines represents cation concentration at dimensionless voltage V while dashed lines do anion concentration.

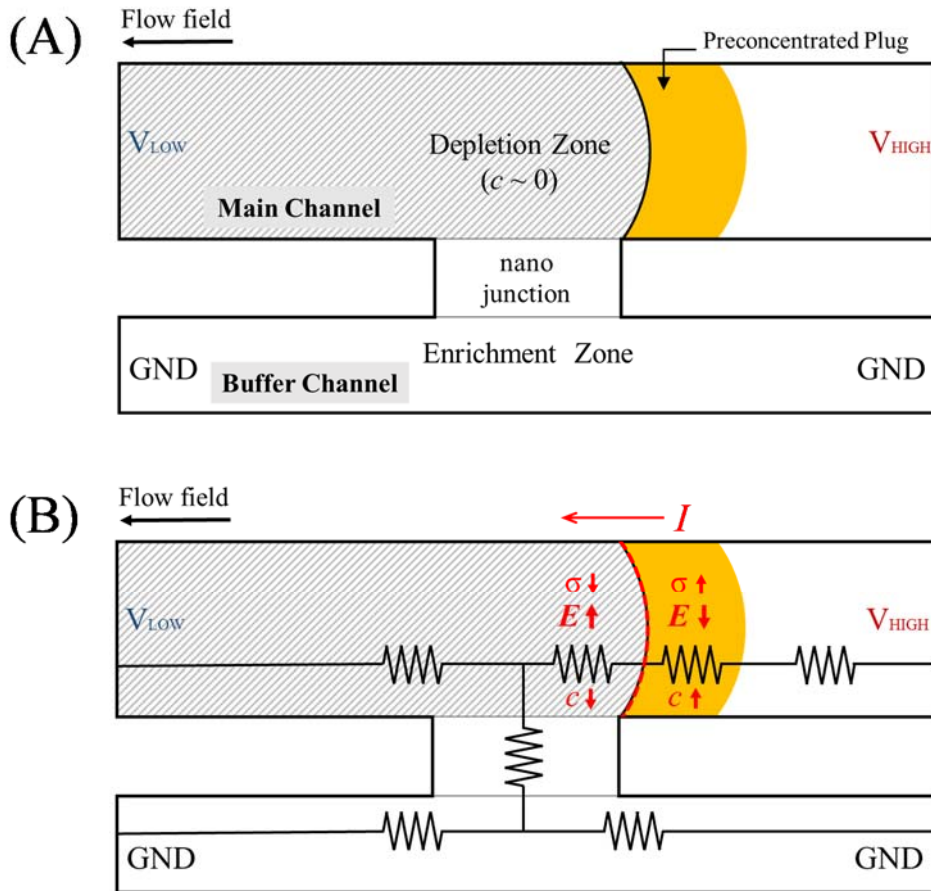


Figure 2.7 (A) Preconcentration at the boundary of depletion zone and (B) schematic of microchannel and nanojunction represented by resistors, where I denotes current, c denotes ion concentration, σ denotes conductance, and E denotes electric field.

microchannel and nanojunction can be interpreted as a connected resistor. Since current along the vicinity of the boundary of depletion zone should be uniform in a microchannel, different value of conductance leads different magnitude of electric field. Conductance is low on the depletion side of the boundary due to low concentration of electrolytes, and high on the other side of the boundary due to high concentration of electrolytes as that in the bulk side. This results in relatively higher magnitude of electric field in the depletion side of the boundary than that in the other side of the boundary. As far as negatively charged molecules are concerned, this electric barrier makes them pre-concentrated at the vicinity of the boundary.

2.3.2 Strategies for selective pre-concentration and online collection

In an environment with low Reynolds number, the flow in the microchannel is described as Stokes flow where inertia is ignored. Charged molecules in the microchannel are influenced by two different forces: electroosmotic force and electrophoretic force. Since the molecules are in the Stokes flow, electroosmotic force is equal to Stokes drag force, $6\pi\mu\mathbf{u}_{EO}R$, where μ is the dynamic viscosity, \mathbf{u}_{EO} is the electroosmotic velocity of bulk which is independent from molecule's properties, and R is the radius of the spherical object. Therefore, the electroosmotic force does not dominantly affect the separation of the pre-concentrated molecules since the size of the molecules in this work is similar (~ 1 nm). On the other hand, electrophoretic force by electrostatic drift exerted on the molecules can be expressed as qE where q is a net electric charge and E is an electric field. Corresponding to the electrophoretic force, another drag force is formed with the magnitude of $6\pi\mu\mathbf{u}_{EPH}R$ where \mathbf{u}_{EPH} is the electrophoretic velocity, in the opposite direction of the electrophoretic force. Since the electrophoretic drag force and electrophoretic force by electrostatic drift should be the same, electrophoretic velocity, \mathbf{u}_{EPH} , is proportional to the net electric charge and electric field. Considering the electric field is almost the same along the area where molecules are pre-concentrated, electric

charge places a key role in the separation of the molecules. As denoted in Figure 2.8, two different kinds of molecules have different equilibrium points due to their electrophoretic mobility. The molecules with higher electrophoretic mobility are preconcentrated towards the reservoir with high voltage while the preconcentrated molecules with low mobility stay near the nanojunction.

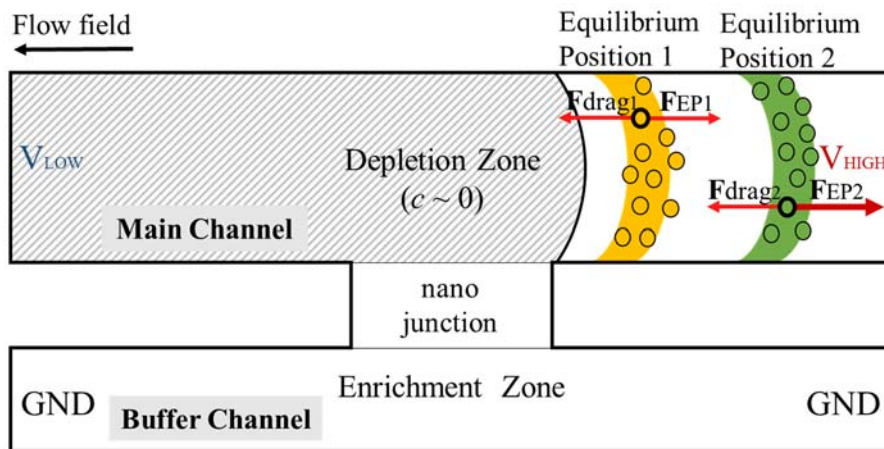


Figure 2.8 Schematic diagram of selective preconcentration mechanism with different mobility. The separation was drawn by the equilibrium between electroosmotic drag force and electrophoretic force exerted on molecules.

Chapter 3

Selective preconcentration with micro pneumatic valve system

3.1 Experimental setup

3.1.1 Strategies for selective preconcentration and online collection

In this work, repeated microchamber structures have been employed, since (1) they can suppress unexpected expansion of the ion depletion zone and vortices, (2) the electric field varies strong/weak repeatedly for easy trapping and (3) they can cut the tail of preconcentrated plugs for clear visualization. Both experimental and numerical analysis for supporting this structure are as following.

We analyzed the preconcentration behavior for various microchannel geometries. As shown in Figure 3.1(A), molecules were highly preconcentrated near the boundary of the ion depletion zone in a straight channel, while the preconcentrated plug kept propagating toward the reservoir along the boundary of the depletion zone. Because of the following extraction system, pinning the location of plugs was critical issue in our system and we had tried to resolve this by manipulating the strength of electrical field using various microchannel geometries such as funnel and narrow

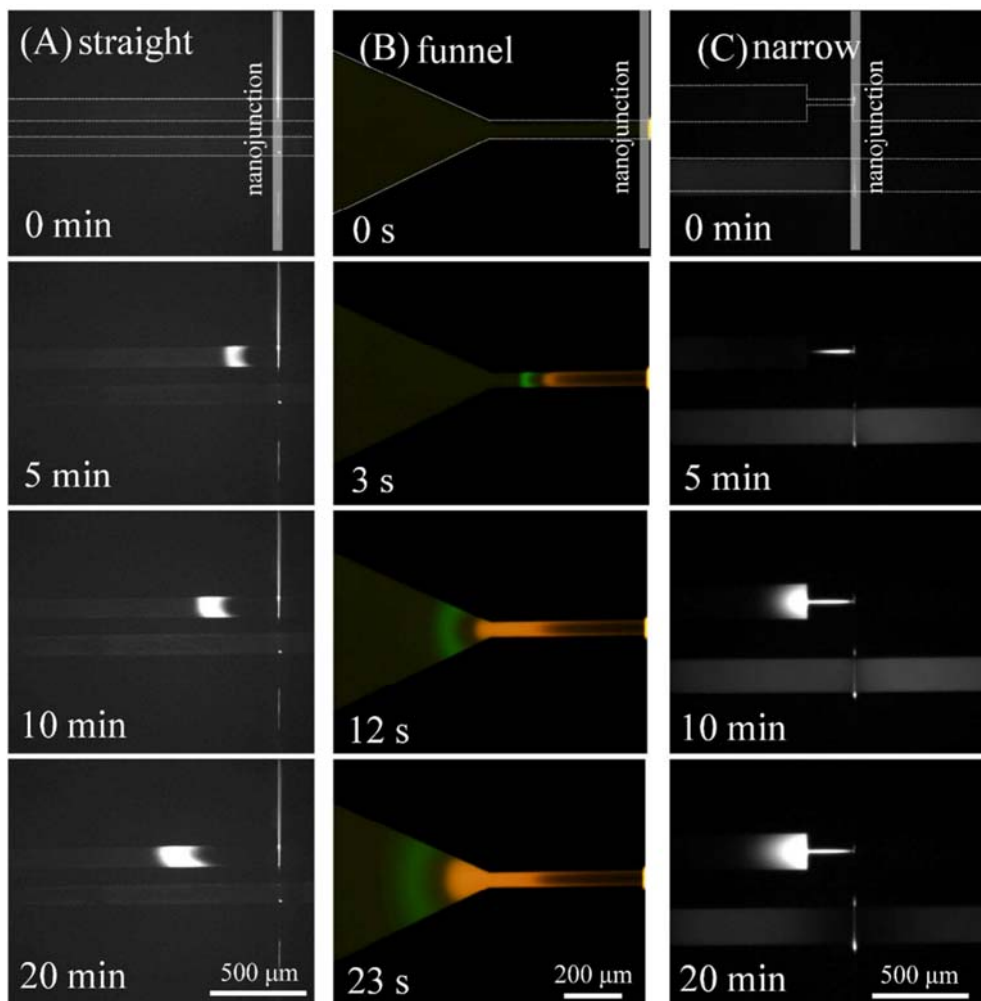


Figure 3.1 Preconcentration operation in (A) straight microchannel, (B) funnel microchannel and (C) narrow microchannel.

shape. In a funnel channel, a pre-concentrated plug was arrested at the boundary of the depletion zone which stopped expanding at the site where the channel starts to diverge. However, the second pre-concentrated plug dispersed significantly as shown in Figure 3.1(B).

In order to obtain steeper gradient an electric field,²⁶ a narrow structure was designed as shown in Figure 3.1(C). It was found that a narrow channel close to the nanojunction curbed the ever-expanding depletion zone, i.e. stabilizing (or pinning) the depletion zone. Therefore the pre-concentrated plug, which moved along the expanding depletion zone otherwise, pinned at each balanced site since the depletion zone was confined. Also, repeating narrow and wide channels impeded the dispersion and diffusion of the pre-concentrated plug. To be specific, the difference of electric field in a narrow and a wide channel engendered the difference of velocity in each channel, which facilitated the efficiency of separation.

Therefore the repeated chamber structure is supposed to have superior performance in terms of stability, cutting off tails out of Gaussian distributed plugs and helping extraction strategy. Following theoretical analysis showed that the electrical field formed at narrow section was significantly amplified so that it can act as an energy barrier to distinguish dyes. In addition, the chamber structure can effectively prohibit the expanding depletion zone by restricting vortices in the chamber.

For investigating the effect of repeated chamber structures, numerical simulations were conducted by COMSOL Multiphysics 4.4 as a commercial FEM (finite element method) tool. Because the ICP layer is highly nonlinear region, it is difficult to ensure the convergence and the stability of numerical solutions. To resolve the critical problem, the local electroneutrality (cation concentration is equal to anion concentration in whole domain) was adopted.^{22a} Namely, thin double layer approximation and ideally cation-selective membrane were chosen to reduce the computational cost. Under the local electroneutrality constraint, independent

variables such as ion concentration (c), electric potential (ψ), pressure (p), and flow fields (\mathbf{u}) were governed by the diffusion-convection equation, the current conservation, the continuity equation, and the Stokes equations.^{22b} ICP phenomena in a straight channel (4 mm in length and 150 μm in height) and a repeated chamber structure (using same geometry of experiments) were analyzed by the governing equations. For the numerical stability, the voltage configurations at inlet and outlet were set to be 5 V and 3.3 V which were enough to generate the ICP phenomena inside the microchannels. The concentrations at inlet and outlet were fixed to the bulk concentration. The flow conditions at the boundaries were set to be a zero-flow rate due to pressure balance between two reservoirs.²⁷ We assumed that the microchannel walls have uniform zeta potential of -100 mV of which value is usual condition on PDMS surface.²⁸

The simulation results were depicted in Figure 3.2. First of all, the repeated chamber structures are able to effectively confine the ion depletion zone (dark blue region) in comparison to the straight channel as shown in Figure 3.2(A). This means that the ICP layer in the repeated chamber would be stabilized because the flow instability generated by concentration fluctuation⁴ occurs only inside the first chamber where nanojunction was installed. This is helpful to obtain the stable preconcentrated plug after the first chamber. As depicted in Figure 3.2(B), the strength of electric field was changed monotonically in the longitudinal direction of the straight channel while the strength was altered pseudo-periodically for the repeated chambers. Electric potentials obtained from the electrical field strength were schematically illustrated in Figure 3.2(D). While monotonically increased electric potentials were observed in straight microchannel (red line), there was a (almost) plateau inside microchamber with steep changes in narrow regions (blue line). A charged species would be immobilized in this plateau region. Due to the pseudo-periodic electric field and the plateau of electric potential, the preconcentrated plug would be easily trapped in each chamber. Lastly, fast vortices

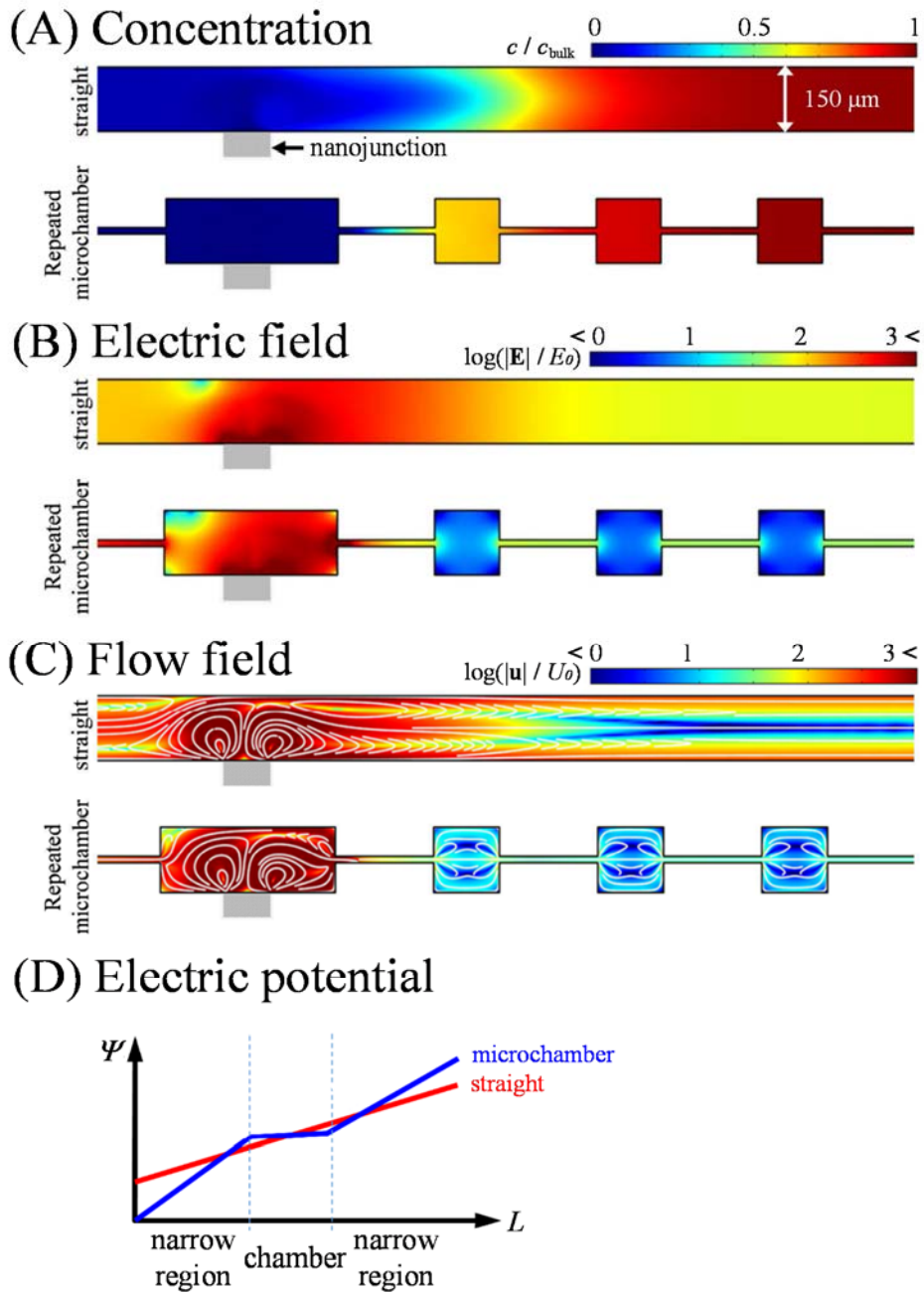


Figure 3.2 Numerically simulated ICP layer for (A) concentration distribution, (B) electrical field and (C) flow field. (D) Schematic illustration for electric potential near the microchamber.

were confined in the first chamber so that stable flow fields were generated beyond the chamber (Figure 3.2(C)). Thus, the alterations of ICP layer by the repeated chambers would provide effective mechanisms for a stable selective preconcentration.

3.1.2 Preparation of PDMS microchips

Figure 3.3(A) showed the microscopic image of the multilayered selective preconcentration device with pneumatic valve system. We implemented microchamber structures repeatedly to suppress fluidic instability and differentiate the flow velocity within a single channel. Buffer channel was connected to the main channel with a perm-selective Nafion membrane. The depth of all microchannels was fixed to 15 μm and three microchambers (150 μm X 150 μm) were connected by 15 μm X 225 μm microchannel as shown in Figure 3.3(A). At the right most microchamber, a microchamber with the same size was upwardly connected to collect isolated preconcentration plugs. There were fundamental and practical reasons to set the narrow height as 15 μm . In current design, the microchamber structure has the repeated height of 150 μm (wide height) and 15 μm (narrow height) in order to keep 10 : 1 ratio. The numerical simulation taught us that 10 : 1 was enough to focus the electric field and keep the position of the plug. Here, the wide height over 150 μm would give disperse preconcentrated plug so that we set the maximum wide height as 150 μm . The practical reason was that a mask resolution under 15 μm cost 5 times more expensive than the mask resolution over 15 μm , leading to a hurdle for commercialization. By both reasons, we kept 150 μm : 15 μm in current design. A rib-shaped channel was also subsequently connected to be used as a measurement window. Microvalves (the width and height were 290 μm each) were designed to cover 4 locations as indicated with red ink in Figure 3.3(A). Note that each microchamber could have its own collection channel depending on the

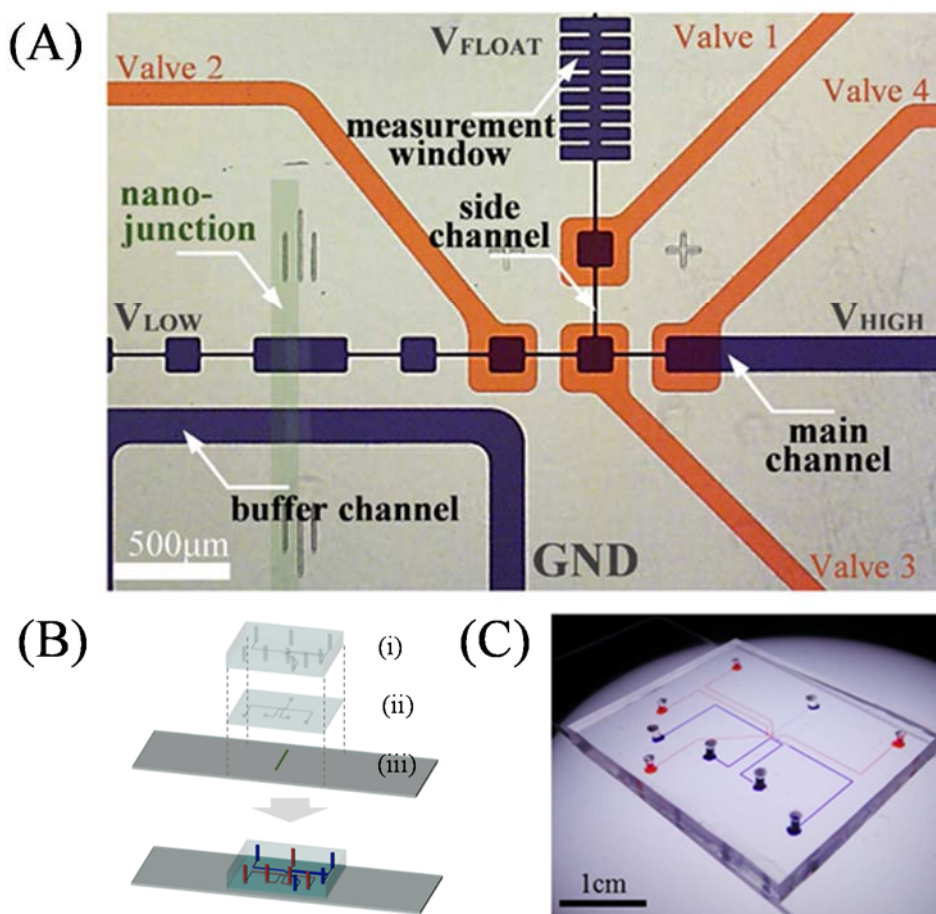


Figure 3.3 (A) Microscopic view of the selective preconcentration device. The microchannels in the ICP layer were indicated with blue and the microchannels in the valve layer were indicated red. (B) An exploded view of the device with (i) a valve layer, (ii) an ICP layer and (iii) a Nafion patterned slide glass. (C) Assembled multilayered online selective preconcentration device.

location where target analytes were preconcentrated. However, in this work, we designed the device with only one collection channel to show the possibility of achieving the collection of selectively preconcentrated dyes. If one would like to collect dyes from different microchambers, one could install additional collection channels to the microchamber.

The first layer as shown in Figure 3.3(B)-(ii) is an ICP layer where selective preconcentration occurred. This thin layer is followed by valve layer as shown in Figure 3.3(B)-(i) which blocks the ICP layer pneumatically. The thickness of the layer between an ICP channel and a valve channel is 10 μ m and it is thin and elastic enough to block the ICP layer when air comes in. Fabrication methods were described as follows. A 4-inch wafer was spun to coat 15 μ m layer of SU-8 2015 photoresist (MicroChem. Inc, USA) at 500 rpm of 10 seconds (pre-spinning) and at 3250 rpm for 30 seconds (spinning). After 3 minutes of soft bake at 95 °C, the layer was exposed two times to ultraviolet (UV) of 365 nm wavelength for 23.3 seconds (400 mW) using a mask aligner. Post bake was for 4 minutes at 95 °C, then was soaked in isopropyl alcohol (IPA) for 3 minutes. For easy detachment of the PDMS device, trichloro(1,1,2,2- perfluorooctyl)silane was applied to the master wafer with a vacuum assisted deposition desiccator. PDMS base and curing agent (Sylgard 184 Silicone elastomer kit, Dow Corning, USA) were mixed at 10 : 1 ratio and desiccated in a vacuum pump for 1 hour to remove air bubbles. The mixed solution was poured onto the master and cured in room temperature overnight for the valve layer (Figure 3.3(B)-(i)), preventing alignment error due to thermal shrinkage. For the ICP layer, the mixed solution was poured onto the patterned 4-inch wafer and spun at 1500 rpm for 300 seconds (JSP4A, JD Tech, Korea) to coat 25 μ m PDMS layer (Figure 3.3(B)-(ii)). Then, the coated wafer was placed on a hot plate for 30 minutes at 95 °C. The PDMS replicas were peeled off from the master and the inlet and outlet holes were punched out. A polymeric nanoporous material, Nafion (20 wt% resin, Sigma Aldrich, USA), was used for the nanojunction between the microchannels. A single

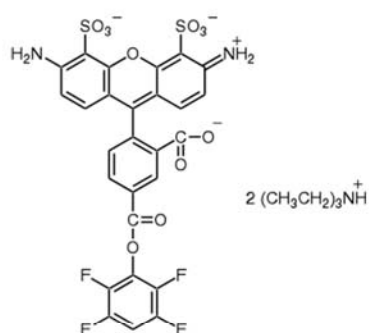
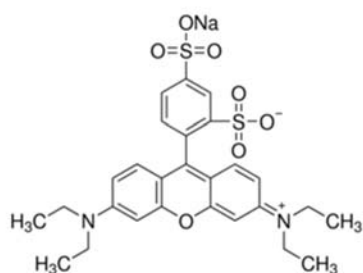
strip of Nafion (100 μm wide and 1 cm long) was patterned on a slide glass using a PDMS piece that has a single straight microchannel and was heated at 95 $^{\circ}\text{C}$ for evaporating solvent after removing the PDMS piece (Figure 3.3(B)-(iii)).¹⁸ Then, each layer was bonded to the Nafion patterned slide glass by oxygen plasma bonder (Femto Science, Korea) under an alignment through the stereo microscope (SZ61, Olympus, Japan) creating a multilayer device. Final assembled micro/nanofluidic device is shown in Figure 3.3(C).

3.1.3 Materials and reagents

Fluorescent dyes were used for observing preconcentration efficiently, which is Sulforhodamine B (Sigma Aldrich, USA), Alexa Fluor 488 (Invitrogen, USA), Alexa Fluor 532 (Invitrogen, USA), and CoroNa Green (Invitrogen, USA). Figure 3.4 describes chemical structure of each molecule. As shown in Table 3.1, sulforhodamine B (SRB) has -1 net charge, and its color is orange color because its maximum absorption wavelength is 565 nm and its maximum emission wavelength is 586 nm. In the case of Alexa Fluor 488 (Alexa 488) and Alexa Fluor 532 (Alexa 532), they have the same -2 net charge but each color is different since they have different absorption wavelength (~ 495 nm and ~ 532 nm for each) and emission wavelength (~ 519 nm and 554 nm for each). CoroNa Green has zero net charge and it absorbs light near 492 nm wavelength and emits cyan-green color light with 516 nm wavelength.

In the experiment of selective preconcentration and online collection, 5 mM KCl solution (Sigma Aldrich, USA) was used with addition of fluorescent dyes for a main channel solution. Their separation and preconcentration dynamics were able to be measured and identified with two different fluorescent colors of orange (SRB) and green (Alexa 488). The concentration of sulforhodamine B was 24.14 nM and that of Alexa 488 was 0.90 μM . For a buffer channel solution, 100 mM KCl was used to minimize a voltage drop in the buffer channel. The ICP operation has been

(A) Sulforhodamine B (B) Alexa Fluor 488



(C) Alexa Fluor 532 (D) CoroNa Green

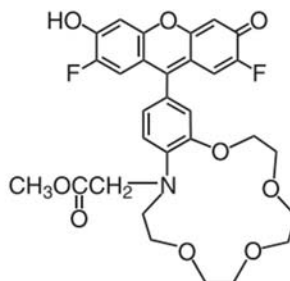
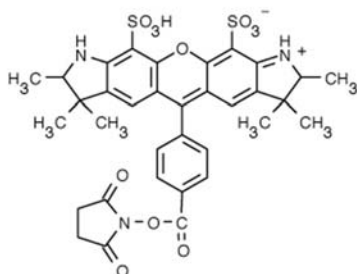


Figure 3.4 Chemical structure of (A) Sulforhodamine B, (B) Alexa Fluor 488, (C) Alexa Fluor 532, and (D) CoroNa Green.

Dye	Color	Absorb [nm]	Emit [nm]	Net charge
Sulforhodamine B	orange	565	586	-1
Alexa Flour 488	cyan-green	495	519	-2
Alexa Fluor 532	green	532	554	-1
CoroNa Green	cyan-green	492	516	0

Table 3.1 Chemical and physical properties of Sulforhodamine B, Alexa Fluor 488, Alexa Fluor 532, and CoroNa Green.

well performed in high salinity samples over 100 mM.^{23,29} In this work, 5 mM KCl was chosen under assumption that the real sample could be post-processed such as removing large molecules and cells (dilution). In such case, the solution of 5 mM concentration would be a proper standard model.

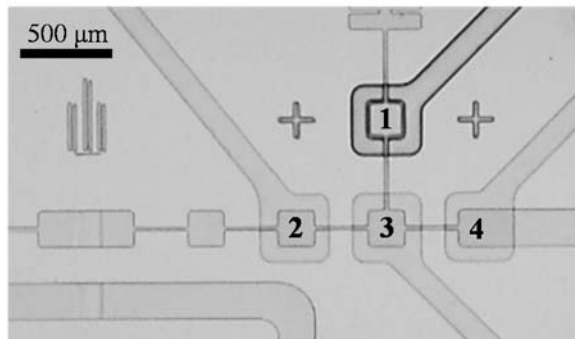
In the experiment of dynamics in preconcentration mechanism, 1 mM KCl solution was used for each main channel and buffer channel. The concentration of sulforhodamine B, Alexa 532, and CoroNa Green was 25 nM, 0.5 μ M, and 34 μ M for each.

3.1.4 System operation method

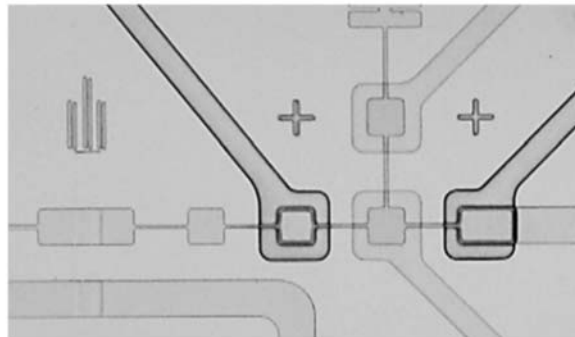
Chemical samples were loaded into the main and buffer microchannel by applying positive pressure from each inlet reservoir. Ag/AgCl electrodes were inserted into the inlet and buffer reservoirs on the device and connected to a power supply (Keithley 6517 and Keithley 238, Keithley Instruments, USA). For applying the electric field, an independent voltage control was required on each of the four reservoirs. For the continuation on separation and preconcentration, 60 V and 90 V were applied to the left and the right reservoir of the main channel, respectively, while the reservoir of the buffer channel was grounded. The motions of fluorescent dyes were tracked by an inverted fluorescence microscope (IX53, Olympus, Japan) and recorded by CellSens (Olympus, Japan) computer program.

A compressor (Gfrog, Stylex, Korea) as a pressure source was connected to 4 mini solenoid valves (SY 3120, SMC pneumatic, Korea) and a polystyrene tube connected a solenoid valve and an inlet of valve layer in the PDMS device. Before the connection, DI water was filled into the microchannels of valve layer to reject air bubbles into the ICP layer. In order to manipulate the pneumatic microvalves automatically, a customized LabVIEW code (National Instrument, USA) and a DAQ board (USB-DAQ 6341, National Instrument, USA) were used. The valve operation consisted 3 steps as shown in Figure 3.5. Step 1 (ICP preconcentration): valve 1 was

(A) Step1 : ICP precon.



(B) Step2 : Isolate



(C) Step3 : Collect

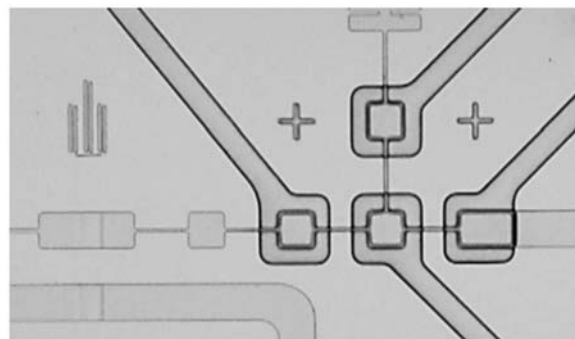


Figure 3.5 Microscopic images of 3-step valve control sequence: Step1 - ICP preconcentration to form a highly concentration plug, Step 2 - isolation of a highly preconcentrated plug at specific microchamber, and Step 3 - collection of the highly preconcentrated plug into upward channel.

closed when selective preconcentration was in process. Step 2 (isolation): when the targeted preconcentration plug reached the microchamber which was connected to the side channel, valve 1 was opened and valve 2 and 4 were closed to isolate the sample plug from the main channel. Step 3 (collection): then, by closing valve 1 and 3 while valve 2 and 4 were still closed, the isolated plug was squeezed into the measurement window. Fluorescent dyes diffused into a larger area and the fluorescence intensity was analyzed without being saturated. By leaving valve 1 closed and others opened, the whole 3-step process cyclically repeated for further collections. One can control the duration of Step 1 to obtain a different preconcentration ratio. Three microchambers with valves were basic building blocks under our current system. If more than 2 analytes are needed to be preconcentrated and separated, the number of microchambers and valves could be added. To do this, the number of microchamber should be larger than the number of analyte. For a different kind of dyes rather than SRB and Alexa, one can tune the electric field to fill targeted microchamber at one's discretion. Here the three-microchamber system was enough for selective preconcentration of 2 dyes regardless of the types of dye.

3.2. Experimental setup

3.2.1 Demonstration of selective preconcentration

Figure 3.6 demonstrated that two different dyes were simultaneously preconcentrated and separated over time. Without electric field along the nanojunction, no fluorescent dyes were observed in the channel because the initial concentrations of dyes were too low to be detected. As we applied 90 V for V_{HIGH} and 60 V for V_{LOW} on each end of the main channel with grounded buffer channel, ICP was triggered nearby the membrane. Micro air bubbles could be generated at the electrode surface with $O(10)$ nA operation currents. Even with these relatively high applied voltages, most of electrical potential was dropped inside the ion depletion zone. In addition, because the electrodes were inserted at the reservoirs

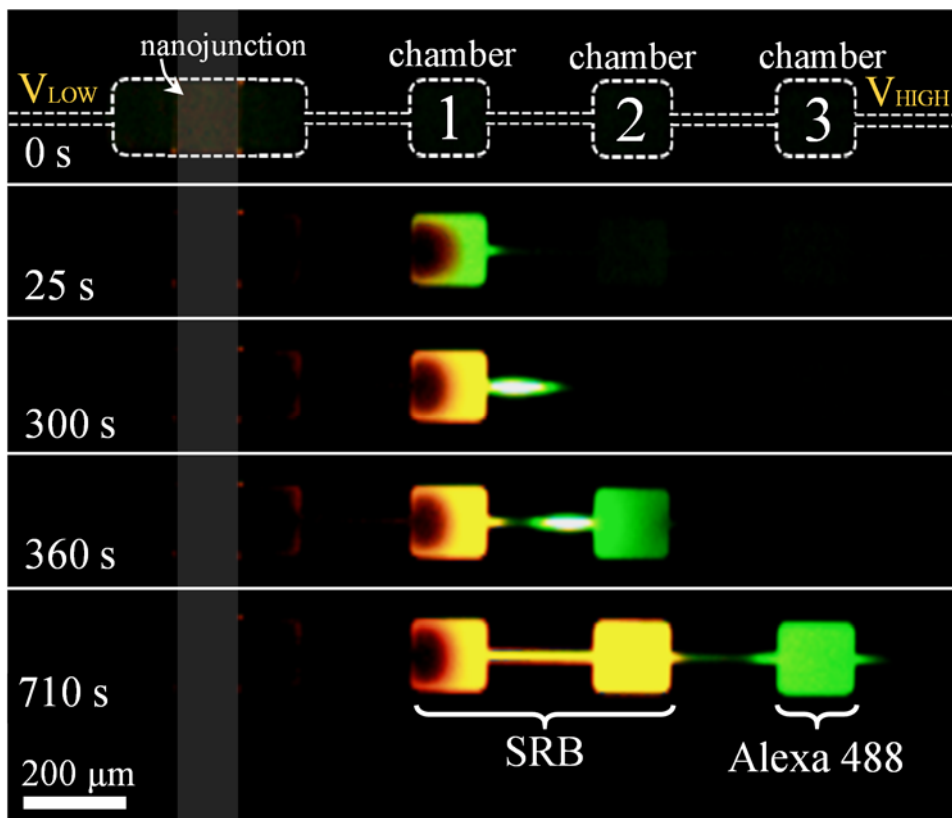


Figure 3.6 Time-lapse images of selective pre-concentration of SRB and Alexa 488. High Concentration ratio was represented by the brightness of fluorescence. Since the physicochemical properties of two dyes were different, they were pre-concentrated at different locations.

which located far from the nanojunction and the reservoirs were opened to ambient atmospheric pressure, the bubble at the electrode surface can float and disappear into the air so that the selective preconcentration operation was not interfered by the bubbles. As reported in previous researches,⁴ the ion depletion zone caused significant and dynamic perturbation in a local ion concentration and in an amplified electric field near the membrane along with the generation of strong electrokinetic flow. The high electric field gradient at the boundary of depletion zone rejected the penetration of charged molecules into the ion depletion zone so that both dyes stacked and detected at the boundary.¹⁵ At the beginning of selective preconcentration, both dyes were preconcentrated in the microchamber 1. After the ion depletion zone became stabilized over time, the preconcentrated plugs of two dyes with different mobility were separated with a separation resolution³⁰ of 1.75. We have adopted the definition of the separation resolution as $R_s = (\text{peak to peak distance})/(\text{average width of bands})$ leading to R_s of 1.75 ($525 \text{ nm}/((450 \text{ nm} + 150 \text{ nm})/2)$). This number indicates a perfect separation (i.e. no overlap) in case of Gaussian distribution. While there has been no exhaustive theoretical analysis on this selective preconcentration process, the mechanism of selective preconcentration was empirically analyzed using force balance.^{11, 31} The force is mobility times particle velocity³² so that we would like to discuss the balance in terms of force rather than mobility, since the size of molecules ($\sim 1 \text{ nm}$) were similar. This separation was drawn by the equilibrium between an electroosmotic drag force and an electrophoretic force as described in Figure 5.¹¹ According to an experimental observation shown in Figure 3.6, Alexa 488 (green) moved toward the right reservoir, while SRB (orange) stayed near the depletion zone boundary. Since F_{drag} is mainly determined by R which is almost the same for SRB and Alexa 488, the value of net charge played a key role in determining the equilibrium positions balanced by F_{drag} and F_{EP} . This argument was in line with the experimental result since the net charge of SRB and Alexa 488 is -1 and -2, respectively.

3.2.2 Stabilization of selective preconcentration

While the phenomenon of different equilibrium positions of molecules with different mobility has been already reported in previous researches,^{11, 31} one strong plug and one smaller plug in parabolic shape were reported and the locations of preconcentrated plugs were always unpredictable due to the strong instability by local amplified electric field near the nanojunction,⁴ instead of stably generated plugs with high concentration. Therefore, it was important to control the positions of the concentrated sample plugs and to stabilize the ion depletion zone. In our system, the repeated narrow and wide channels were able to stabilize the depletion zone by restricting the expansion of vortices and strong electrokinetic flows in the ion depletion zone,^{17b-d, 19, 26} thereby forming a plug at desirable positions. The repeated microchamber structures were able to effectively confine the ion depletion zone in comparison to the straight channel. This meant that the ICP layer in the repeated chamber would be stabilized since the flow instability was generated by concentration fluctuation³³ only inside the first chamber nearby nanojunction. Also, due to the pseudo-periodic electric field and the plateau of electric potential, the preconcentrated plug would be easily trapped in each chamber. Consequently the control of each accumulated molecules' location became simple and tailing effect was reduced. This alternating geometry also differentiated the velocity of the fluidic flow at the boundary between the narrow and the wide channel, and therefore, it increased the efficiency of separation and helped the membrane microvalve system for further blocking and squeezing of the analytes.

3.2.3 Quantitative analysis for separation and preconcentration efficiency

The selective preconcentration was quantitatively analyzed by measuring pixel intensity with fixed exposure time. The intensities of the original sample and reference solutions at different concentrations were compared to accurately measure

the preconcentration ratio, since the pixel intensity was not linearly proportional to the concentration of dyes. As shown in Figure 3.7, the average pixel intensities of dyes increased in each microchamber in order. The both dyes (Alexa 488 + SRB) were rapidly preconcentrated in the microchamber 1 from the initial to 10 minutes. From 10 minutes to 25 minutes, the green plug (Alexa 488) moved to the microchamber 2 while the intensities of the plugs simultaneously increased. This agreed with the microscopic image in Figure 3.6 that the orange plug (SRB) stayed in the microchamber 1, while the green plug (Alexa 488) moved to the microchamber 2. After 25 minutes, the green plug (Alexa 488) moved to the microchamber 3, while the average pixel intensity of the microchamber 2 sharply diminished. In this point, the average pixel intensity of the microchamber 2 did not decrease to zero. This was because the orange plug (SRB) was saturated in the first microchamber so that it went on to the microchamber 2. In the microchamber 3, the average pixel intensity reached up to 98.2, which denoted that the green plug (Alexa 488) was preconcentrated above 100-fold since the average pixel intensities of 10X, 50X, and 100X concentrations of Alexa Fluor 488 were 12.9, 58.9, and 95.3 respectively. After 30 minutes, the repeated microvalve operations were started, showing severe fluctuations and this part will be discussed later. In previous researches, the two separated plugs have been distinguished only by their positions since only one dye was tagged for two or more different kinds of molecules.^{11, 31} Compared to these works, RGB color profile was rigorously investigated to validate the separation of two molecules. Since the emission from SRB has both red and green color, it was efficient to measure color intensities from microchamber 3 as the indicator of separation, where only Alexa 488 dye was preconcentrated. Since the pixel intensities of blue and red were almost the same, only red and green colors were discussed. The color profile of 100-fold reference solution of Alexa 488 at 0.90 mM was 33.28 in red and 219.76 in green under the exposure time of 300 ms. As shown

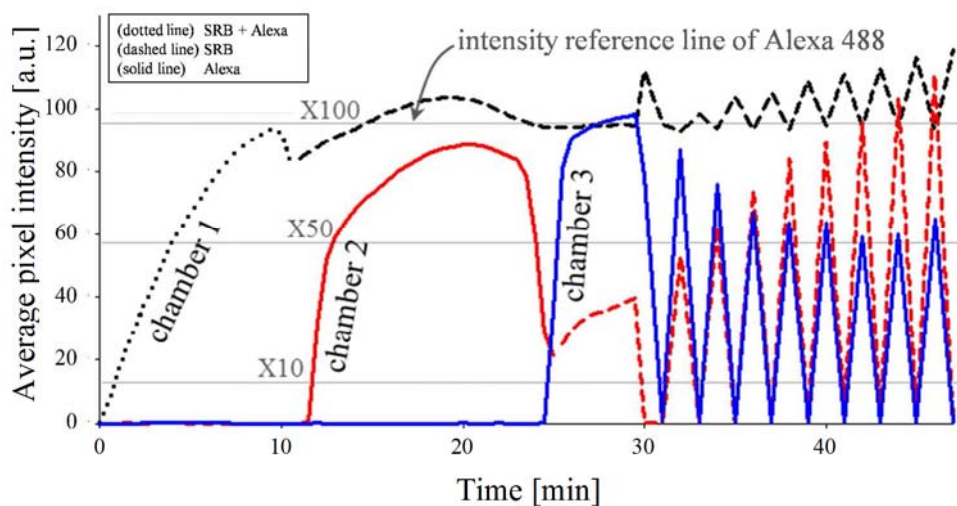


Figure 3.7 Overall fluorescence intensity tracked in each microchamber as a function of time. Dotted line, dashed line and solid line represented the mixture of SRB with Alexa 488, only SRB and only Alexa 488, respectively. Three different colors indicated the pixel intensity of each microchamber (black for microchamber 1, red for microchamber 2 and blue for microchamber 3). The concentration ratio of selectively preconcentrated Alexa 488 in microchamber 3 exceeded 100-fold, maintaining the preconcentration factor high enough in repeated valve operations.

in Figure 3.8, the pixel intensity of the microchamber 3 in the main channel was 223.20 in green and 31.17 in red at the operation time from 25 minutes to 30 minutes, which agreed with the reference values of the 100-fold, meaning that the majority occupying the microchamber 3 was only Alexa 488 dye. In addition to this, the color profile of the microchamber 1 (Figure 3.9) contained high value of red color which was not found in the microchamber 3 as shown in Figure 3.8. The ratio of red and green color was reversed at 10 minutes and maintained around 2 : 1 from 25 minutes to 30 minutes in the microchamber 1. Since SRB was dominant in the original solution (SRB at 24.14 nM + Alexa 488 at 0.90 μ M) and its red/green ratio was 2 : 1, we concluded that the microchamber 1 was solely occupied by SRB after 25 minutes. This color profile measurement provided an accurate platform to measure the separation efficiency between two dyes with different mobility.

3.2.4 Collection of preconcentrated plugs by valve system

As the operation continued further, the preconcentration factor increased accordingly. However, subsequent process using selectively preconcentrated analytes was difficult since the selective preconcentration was performed while the background solution freely flows in a single channel. Besides, a subsequent on-chip process which should exclude electrical operation was inapplicable because the plug drastically dispersed as shown in Figure 3.10(A) when the applied voltage was turned off. To resolve this problem, a plug was required to be isolated and transported to another site, while the preconcentration ratio maintained without loss for either on-chip or off-chip applications. This was able to be realized using pneumatic microvalve system. To guarantee the role of valves to block the plug from the original sample channel, the extent of dispersion was compared between the cases of valve OFF and valve ON as described in Figure 3.10(A) and (B).

The valves were operated in a repeated cycle as described in Figure 3.5 to collect the selectively preconcentrated plug into the side channel. In a cycle, the plug was

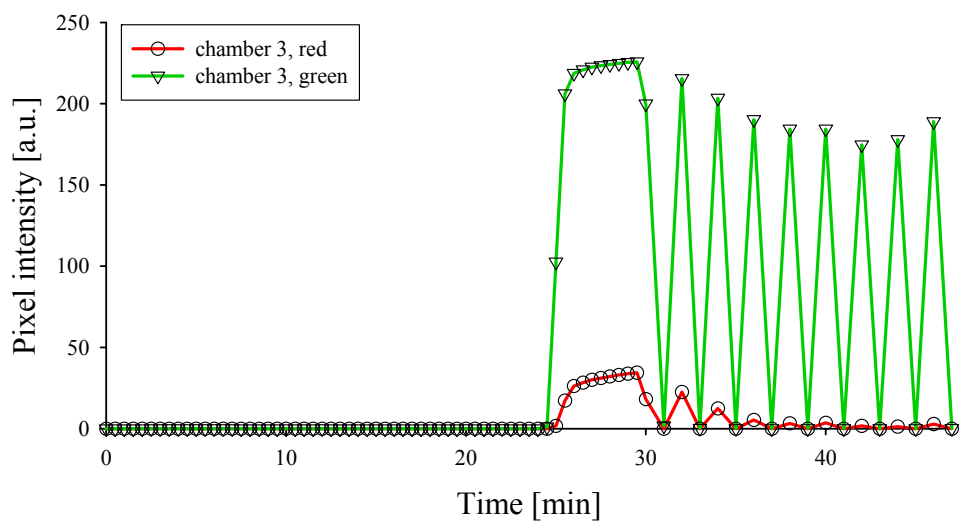


Figure 3.8 Red/green color profile in microchamber 3, showing the microchamber 3 only had Alexa 488.

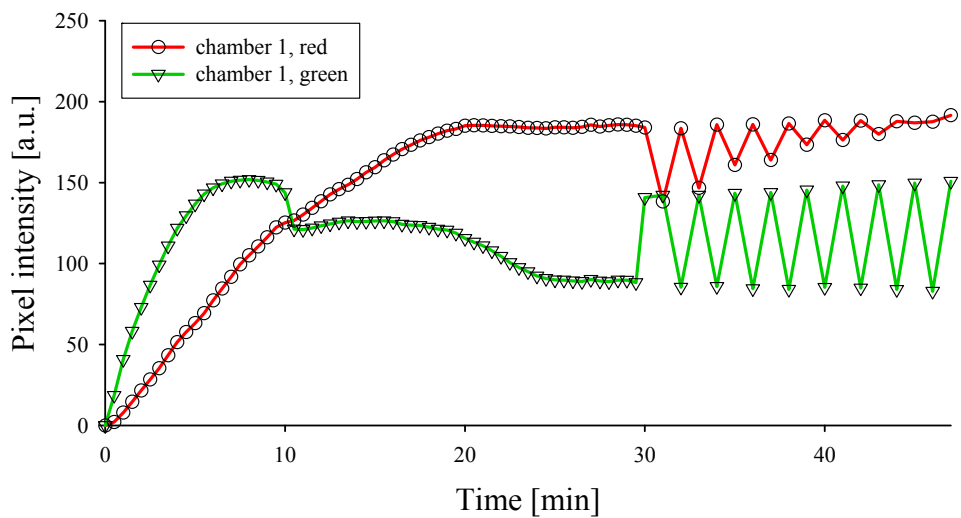


Figure 3.9 Red/green color profile in microchamber 1, showing the microchamber 1 only had SRB. Fluctuations after 30 minutes in all plots showed that the preconcentration factor maintains over 50-fold along the cyclic valve operations. While the error bars were omitted for clear visibility, the tests were conducted at least 10 times with different devices for the repeatability and reliability.

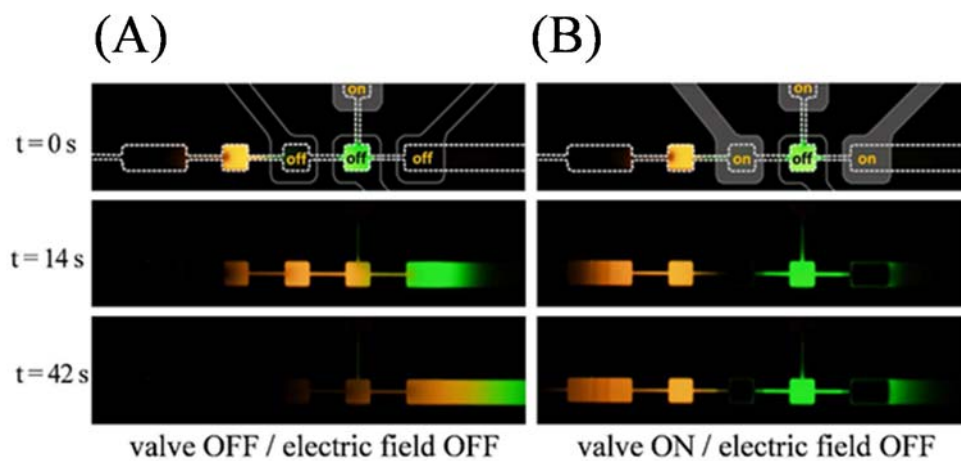


Figure 3.10 Time-lapse images showing the dispersion of isolated plug when the valves were (A) OFF and (B) ON.

isolated from the original sample solution and squeezed up into the side channel. To analyze the preconcentration factor achieved from the process, a rib-shaped measurement window was installed in the middle of the side channel. This measurement window was designed for metering how high the preconcentration ratio would be achieved through the process. In the meantime, the measurement window had larger area than the side channel itself so that it had low fluidic resistance and the side channel connected to an open reservoir to atmospheric pressure, allowing subsequent processes without any disturbance. As shown in Figure 3.11(A), no fluorescence intensity was observed in the measurement window at $t = 0$, because the measurement window was initially filled with sample solution. By the first valve operation, the pixel intensity of measurement window already exceeded 10-fold of the initial concentration of Alexa 488 as plotted in Figure 3.11(B). With repeated valve operations, the concentration of collected plugs in the measurement window continuously increased so that the concentration reached over 30 times of the initial concentration after the sixth operation. After the ninth collection, it was observed that the measurement window was fully filled with green dyes. After this point, a diffusive mixing would not occur anymore. The error bars decreased and the signal saturated according to the number of valve operation, since we measured area averaged fluorescent intensity in whole measurement window. It led largest error bar at the 1st collection because the window was not fully filled with the dye.

The preconcentration factors of each Step 1 in repeated cycles were maintained high enough to continuously increase the pixel intensity of the measurement window. Figure 3.7 also supported this result. In the Figure, the valves were repeatedly operated in the same cycle with the interval of 2 minutes after 30 minutes of selectively preconcentrating operation. When the analytes in the microchamber 3 were isolated by valves and moved up into the side channel, the pixel intensity of the microchamber 3 was zero. The intensity of microchamber 3 increased again with the

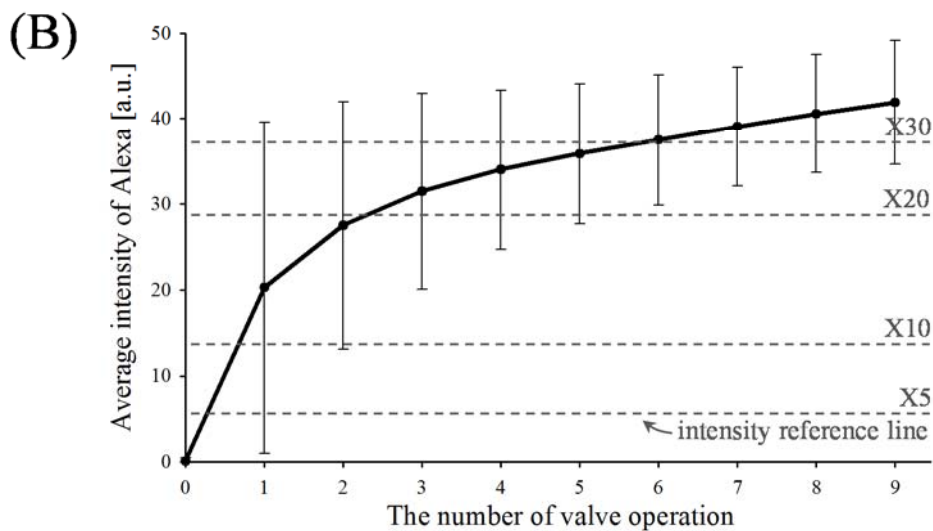
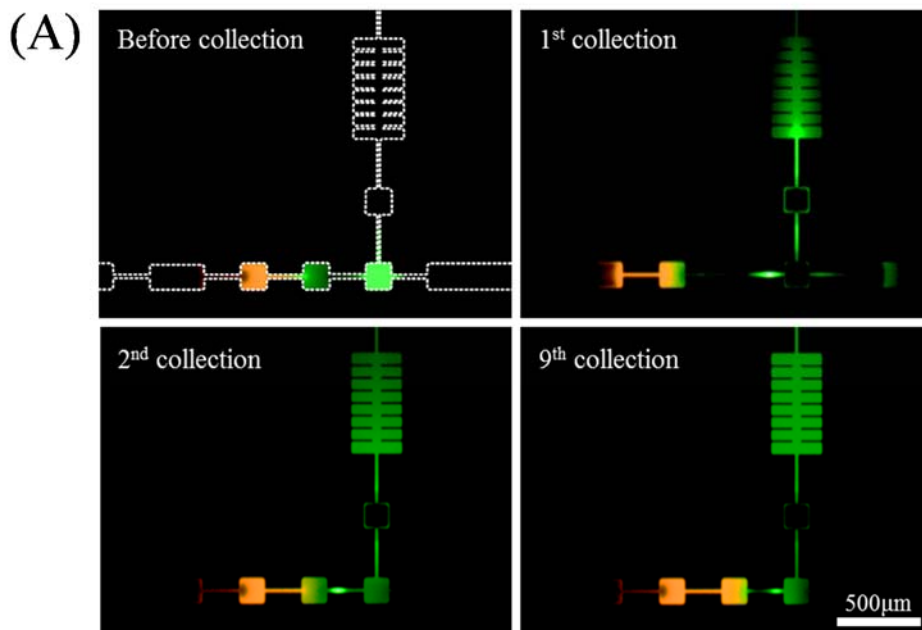


Figure 3.11 (A) Snapshots of repeated valve operations collecting selectively preconcentrated plugs. Compared to the initial state, the measurement window was being filled with green dye (Alexa 488) over several valve operations. (B) Average intensity change in the measurement window over number of repetition of valve operations. The average intensity exceeded 10-fold in a single valve operation, and 30-fold after nine operations. Note that there was no SRB in the measurement window.

next preconcentration operation for 2 minutes. The concentration of Alexa in the microchamber 3 was maintained over 50-fold for all valve operations. The upheld high preconcentration ratio of collected sample was led by stable and reproducible valve operations. Since microvalve systems squeezed the preconcentrated plugs by mechanical force, the mechanism of the collection process barely agitated the external electric field.

3.2.5 Three kinds of analyte

For being used in practical applications, solutions mixed with various kinds of molecules should be considered. Therefore, it is need to confirm that multiple components with different physicochemical properties in solution can be simultaneously preconcentrated and separated under ion concentration polarization. Note that molecules dealt with in this experiment are negatively charged since only cation-selective membrane was used. In conventional methods using ion concentration polarization, there are few demonstrations reported which selectively preconcentrated more than two kinds of analyte.^{5, 11} However, in the studies, separated plugs were observed but it is not confirmed whether each plug is composed of single kind and the order is from high mobility to low mobility. Thus, it is need to investigate more in to confirm that multiple components can be simultaneously preconcentrated and separated under ion concentration polarization in order of the magnitude of mobility.

Figure 3.12 shows simultaneous preconcentration and separation of three different kinds of analyte, which are SRB, Alexa 488, and Alexa 532. Tangential electric field was generated with 45 V and 70 V for each low voltage and high voltage. This voltage configuration was empirically adjusted for effective selective preconcentration. When the voltage was applied, ion depletion zone was developed and three dyes were preconcentrated at chamber 1. After 70 s, only the preconcentrated plug of Alexa 488 propagates to chamber 2. After 160 s, Alexa 532

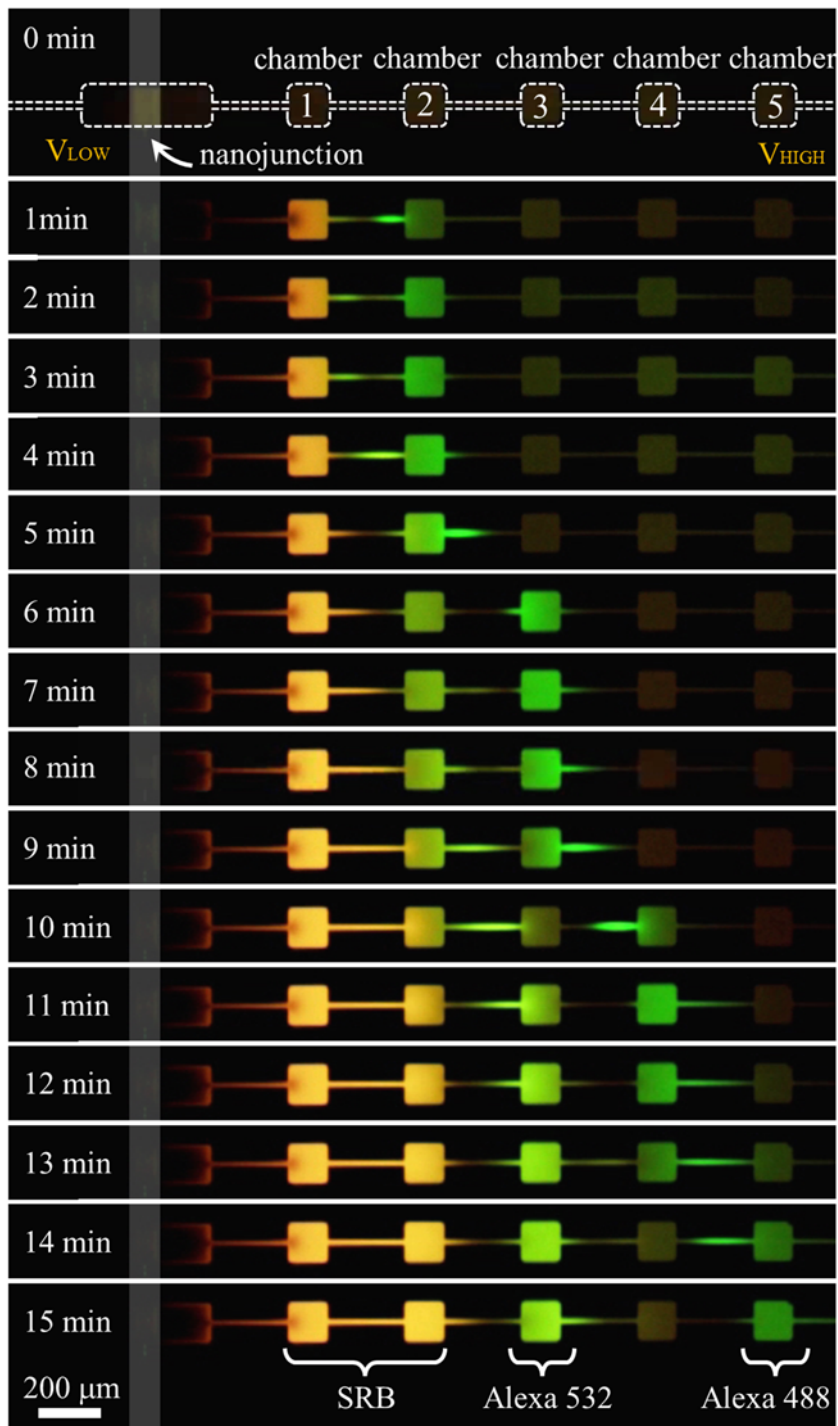


Figure 3.12 Time-lapse images showing the selective preconcentration of SRB, Alexa 532 and Alexa 488. Three different dyes were simultaneously preconcentrated and separated.

was separated from SRB and moved to chamber 2. In this point, the chamber 2 was occupied with Alexa 488 and Alexa 532. Around 5 minutes, Alexa 488 in the chamber 2 started to move to chamber 3 while Alexa 532 stayed still in the chamber 2. Consequently, three different dyes were successfully separated while the concentration of each preconcentrated plug was increased. As separated three plugs moved toward the reservoir with high voltage due to electrophoretic mobility, the plugs were not mixed over time.

The concentration ratio of each dye was quantitatively investigated through examining pixel intensities. In the case of Alexa only green pixel intensity was examined as shown in Figure 3.13. Alexa 488 was preconcentrated up to nearly 30-fold in chamber 1. However, as Alexa 488 dye moved to the next chambers, the concentration of preconcentrated plug became decreased. Also, the slope of the pixel intensity decreased, which means that the preconcentrated plug dispersed along with the movement. Figure 3.14 represents green pixel intensity with the reference line of Alexa 532. It showed that the concentration of Alexa 532 increased as it moves to the next chambers. Although the initial concentration of Alexa 488 and Alexa 532 was the same in the main channel solution, the tendency turned out to be completely different. As it was in the case of Alexa 488, the plug of Alexa 532 was also dispersed as it moved but the concentration ratio became increased and exceeded 100 times of initial concentration ratio after 20 min. It is interesting phenomenon requiring further investigation. In the case of SRB, only red pixel intensity was examined as shown in Figure 3.15 other than green and blue pixel intensity. Before moving to the chamber 2, the concentration of SRB was increased almost 50-fold. Also, the concentration of SRB became gradually increased even after propagating to the next chamber. This means that dyes from the reservoir with high voltage were continuously preconcentrated in the first order over time even with the existence of the other two dyes.

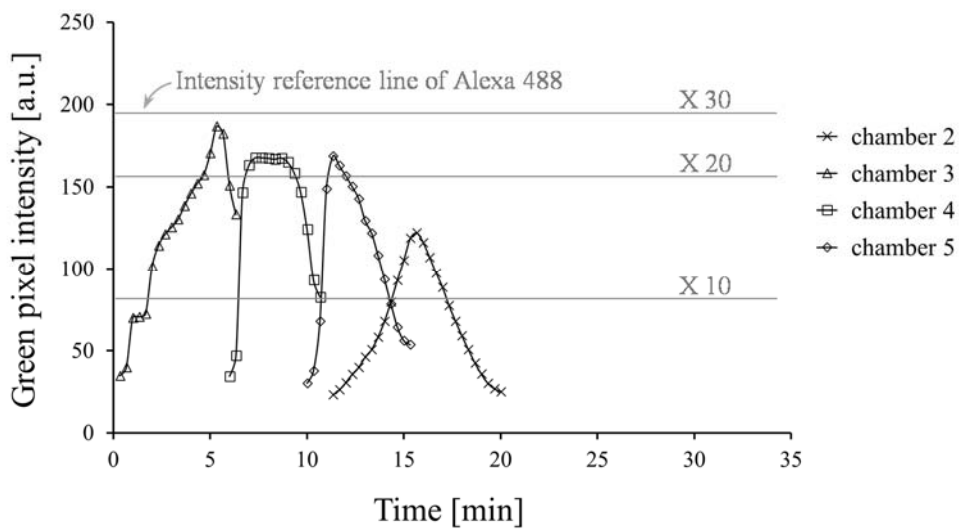


Figure 3.13 Green pixel intensity tracked in each microchamber as a function of time with the intensity reference line of Alexa 532. A triangular marker, a rectangular marker, and a diamond marker, and x marker represent the green pixel intensity in microchamber 2, microchamber 3, microchamber 4, and microchamber 5, respectively.

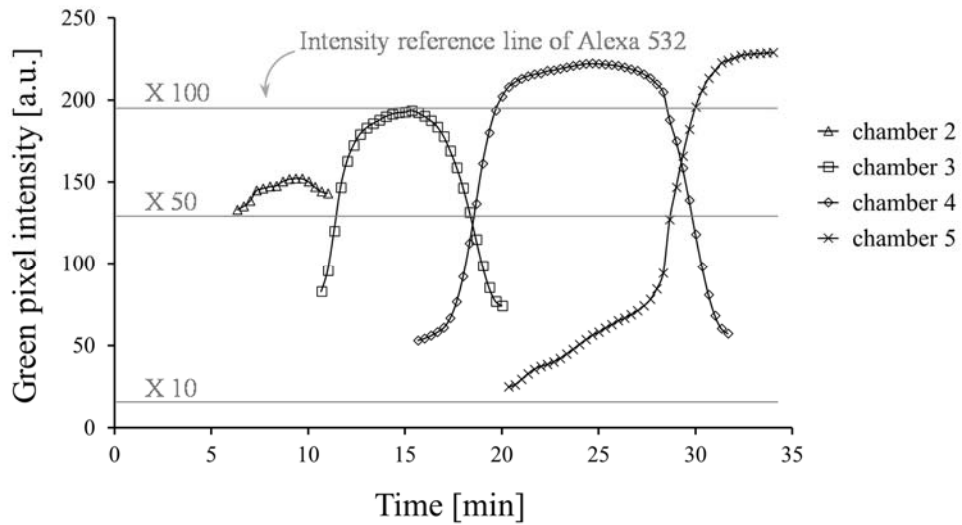


Figure 3.14 Red pixel intensity tracked in each microchamber as a function of time with the intensity reference line of SRB. A circular marker, a triangular marker, a rectangular marker, and a diamond marker represent the red pixel intensity in microchamber 1, microchamber 2, microchamber 3, and microchamber 4, respectively.

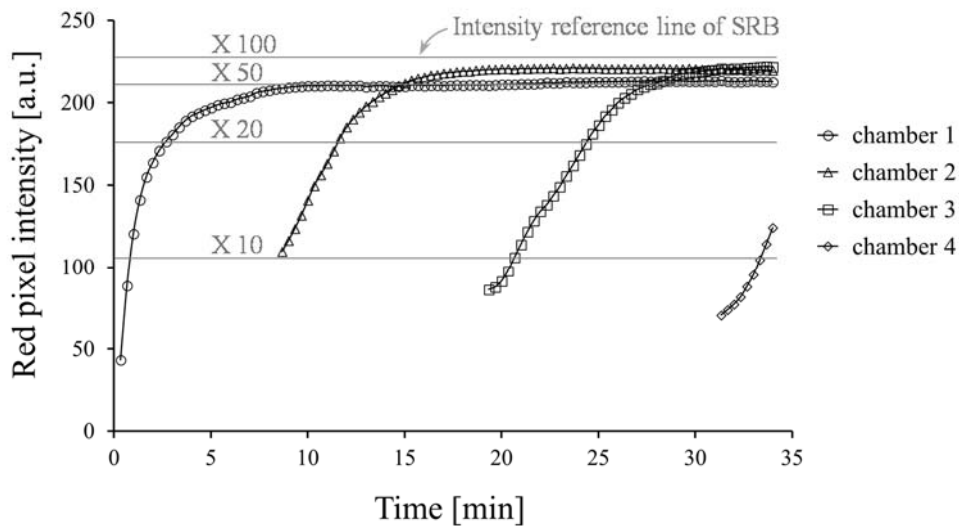


Figure 3.15 Green pixel intensity tracked in each microchamber as a function of time with the intensity reference line of Alexa 488. A triangular marker, a rectangular marker, and a diamond marker, and x marker represent the green pixel intensity in microchamber 2, microchamber 3, microchamber 4, and microchamber 5, respectively.

3.2.6 Correlation between voltage configuration and separation time

When different molecules are selectively preconcentrated, time to take for separation determines separation efficiency as well as separation resolution does. It is difficult to optimize voltage configuration for separating negatively charged molecules near cation-selective membrane to be fast with sharp separation resolution since increasing electric field reversely enhances the magnitude of electrophoretic force and electroosmotic force in an opposite direction. Therefore, investigation with different voltage values of V_{HIGH} and V_{LOW} is required to find optimal condition.

In this part, 20 V, 30V and 40V were taken for V_{LOW} , and 80 V, 90 V, 100 V, 110 V, and 120 V were taken for V_{HIGH} in order to find optimal condition by measuring time for separation and the extent of dispersion. Figure 3.16 showed representative three results among those voltage configurations. The difference (ΔV) between V_{HIGH} and V_{LOW} is 100 V, 80 V, and 80 V for each but V_{HIGH} which dominates the generation of depletion zone is 120 V, 100 V, and 110 V for each as shown in Figure 3.16(A) (case 1), (B) (case 2), and (C) (case 3). The fastest elapsed time was found in the case 1 with the voltage configuration of 20 V for V_{LOW} and 120 V for V_{HIGH} and the lowest elapsed time was found in the case 2 with the voltage configuration of 30 V for V_{LOW} and 110 V for V_{HIGH} .

Different condition between the case 1 and case 2 only came from the fact that V_{HIGH} in case 1 was higher than V_{HIGH} in case 2. As shown in Figure 3.16(A) and (B), the separation speed of case 1 was faster than that of case 2, and the case 1 had lesser dispersion than the case 2 had. This result can be explained by conventionally known theories as mentioned in chapter 2. As the V_{HIGH} increased, electrophoretic force and electroosmotic force on Alexa 488 simultaneously increased. Therefore, each magnitude of those two forces must have been greater in the case 1 than in the case 2. The result of the case 1 revealed that the increase of the magnitude in electrophoretic force was dominant over that of the magnitude in electroosmotic force in those cases. This was evidenced by empirical phenomenon. Alexa 488

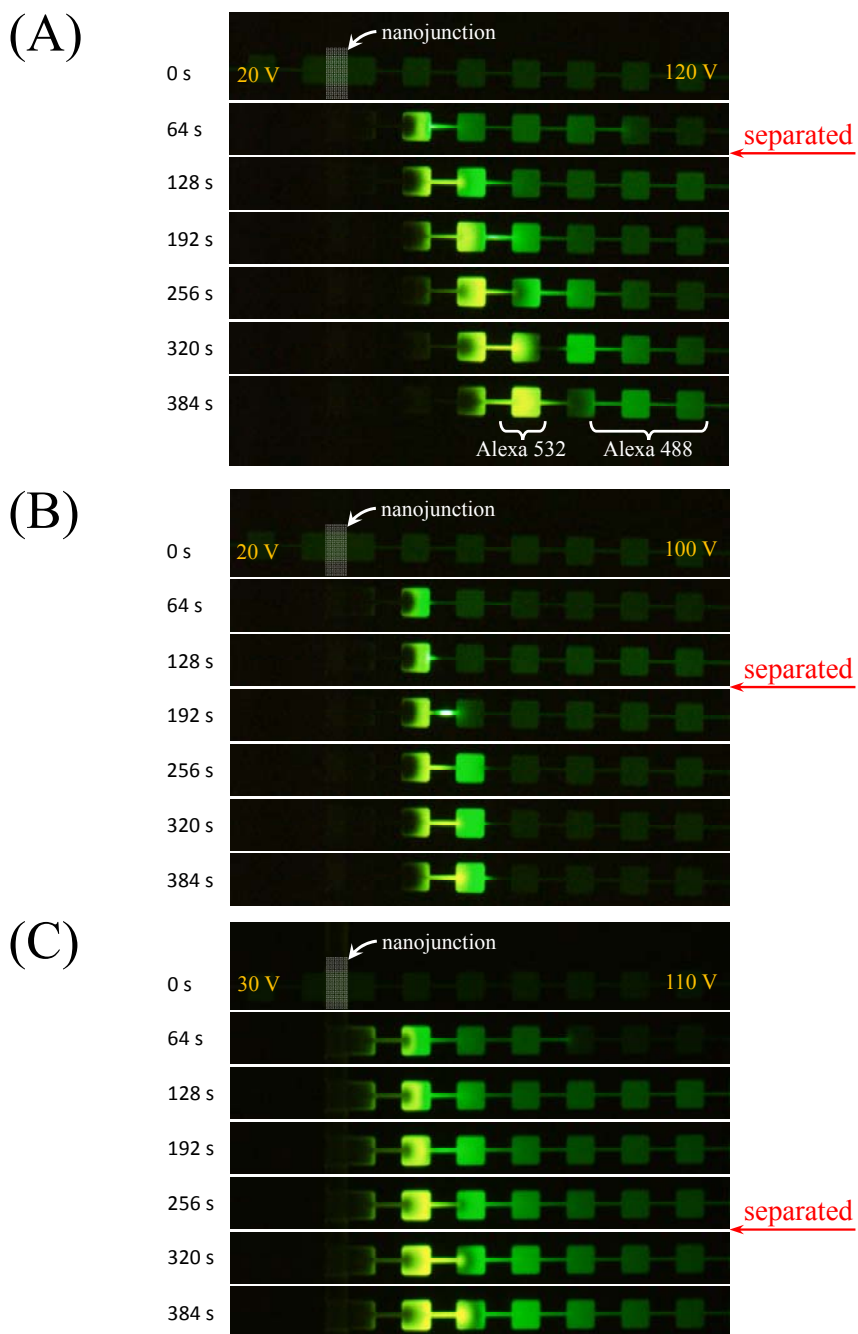


Figure 3.16 Time-lapse images of selective preconcentration of Alexa 488 and Alexa 532 with the voltage configuration of (A) V_{LOW} for 20 V, V_{HIGH} for 120 V, (B) V_{LOW} for 20 V, V_{HIGH} for 100 V and V_{LOW} for 30 V, V_{HIGH} for 110 V, respectively. The separation time of Alexa 488 from Alexa 532 takes longer in order of (A) to (C), respectively.

moved towards the reservoir with anodic electrodes faster in the case 1 than in the case 2. Consider the anodic channel as two parts divided by the location of nanojunction: a channel on V_{HIGH} side and a channel on V_{LOW} side. On the V_{HIGH} side, significantly large voltage drop occurred in depletion zone which is very short-sized region comparing to the entire length of the V_{HIGH} side. Therefore, considering average electroosmotic flow, the electroosmotic flow generated by the field on the V_{HIGH} side in the case 1 and the case 2 would not much different from each other. On the V_{LOW} side, the case 1 and the case 2 had almost the same electroosmotic flow since their values of V_{LOW} are the same. The superposition of these two flows would give similar net electroosmotic flow in the case 1 and the case 2. In this point, the movement of equilibrium position in the case 1 comparing to the case 2, according to the theory in chapter 2, resulted from the increased magnitude of electrophoretic force on molecules. Secondly, other than the location of equilibrium point, dispersion tells the dominant effect of electrophoretic force.

In the comparison of the case 2 and the case 3, however, it is not simply explained with the mechanisms mentioned in the chapter 2. In these two cases, increased V_{HIGH} led the plugs dispersed as expected, but the separation speed became, surprisingly, slowed down, which is distinct aspect from the case 1 and case 2. To investigate which results this peculiar aspect, operation map was drawn of various kinds of voltage configuration as shown in Table 3.2. Figure 3.17 describes the map of the time for Alexa 488 to separate from Alexa 532 under each V_{LOW} and V_{HIGH} according to the voltage configuration in Table 3.2. It was shown that the difference between voltages of each reservoir in anodic side did not have typical tendency other than some optimal points such as the maximum and the minimum. This can be interpreted as another evidence that the selective preconcentration occurred under nonlinear regime under ion concentration polarization system. For now, it seems to be an utmost efforts to obtain operation map and search the optimum point between separation time and the extent of dispersion if one wants to find the optimal condition

V_{LOW} [V]	V_{HIGH} [V]	Separation time [s]
20	80	252.8
	90	236.8
	100	201.6
	110	118.4
	120	86.4
30	80	224.0
	90	256.0
	100	256.0
	110	288.0
	120	256.0
40	80	224.0
	90	256.0
	100	256.0
	110	256.0
	120	224.0

Table 3.2 Separation time values of Alexa 488 from Alexa 532 in a repeated-chamber channel with different voltage configuration.

Separation time of Alexa 488 from Alexa 532

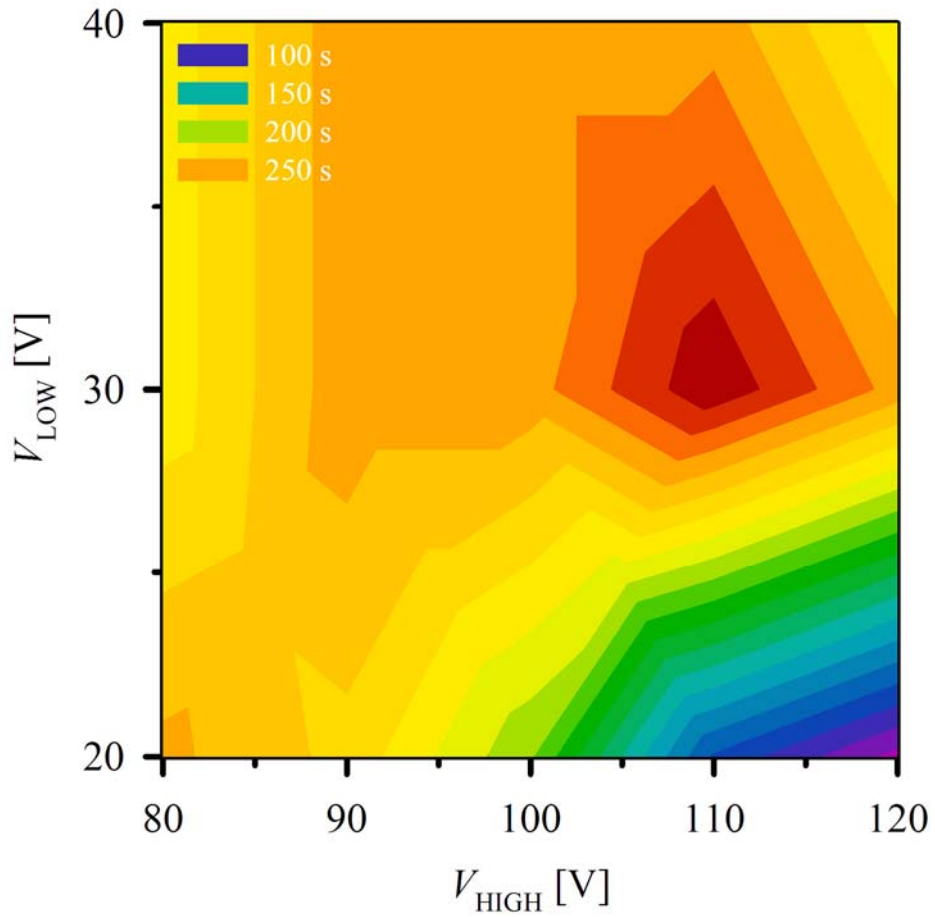


Figure 3.17 Operation map of the time for Alexa 532 to separate from Alexa 488 under each V_{LOW} and V_{HIGH} . There exists the maximum point and the minimum point.

for efficient separation.

3.2.7 Mobility-dependent preconcentration dynamics

Considering the aspect of separation as shown in Figure 3.6 and Figure 3.16(B), it is evident that the preconcentrated location kept moving after enough time scale for the development of ion depletion zone. If only electroosmotic force and electrophoretic force are effective on the separation, two different molecules must have been preconcentrated at different location. However, the results above all showed that the preconcentration of different dyes occurred at the same location and one of them was separated later over time. To figure out unknown factor which can determine the equilibrium point of selective preconcentration, we adopted a simple device with a straight channel as shown in Figure 3.18.

It was found that preconcentrated molecules interact with each other and this interaction affects the separation of the preconcentrated plugs. Figure 3.19 describes this phenomenon. SRB and Alexa 532 were used for confirming this mechanism in 1mM KCl solution. 15 V was applied for low voltage and 30 V was applied for high voltage. As denoted in Figure 3.19(A) and (B), each preconcentrated plug had its own equilibrium point over time. Also, SRB began to preconcentrate right next to the depletion zone and was stacked over time while the preconcentration plug of Alexa 532 propagates to the reservoir of high voltage side. When these two dyes were mixed in a solution and preconcentrated under ICP as denoted in Figure 3.19(C), SRB was preconcentrated as it was in Figure 3.19(A). However, Alexa 532 appeared in a different way. Comparing to the preconcentration in Figure 3.19(B), Alexa 532 in a mixed solution was preconcentrated backward to the reservoir with high voltage. Due to the existence of SRB, it seemed that Alexa 532 was pushed away by the preconcentrated plug of SRB. Since the net electric charge of SRB is -1 and that of Alexa 532 is -2, the electrophoretic mobility of Alexa 532 is greater than that of SRB. Although this cannot explain why SRB stacks near the boundary of depletion

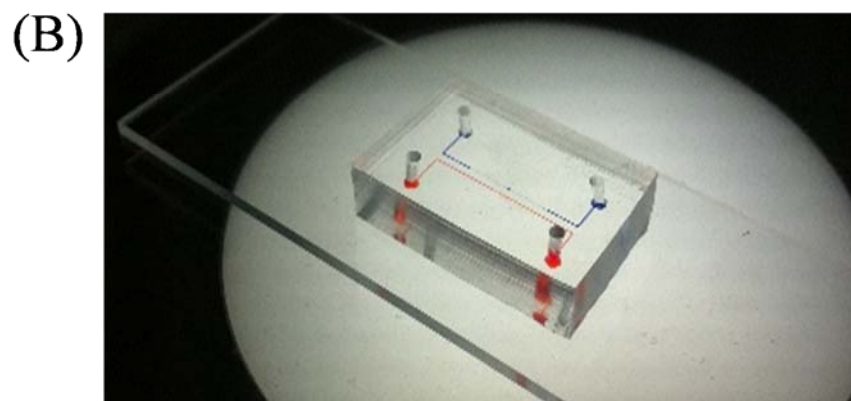
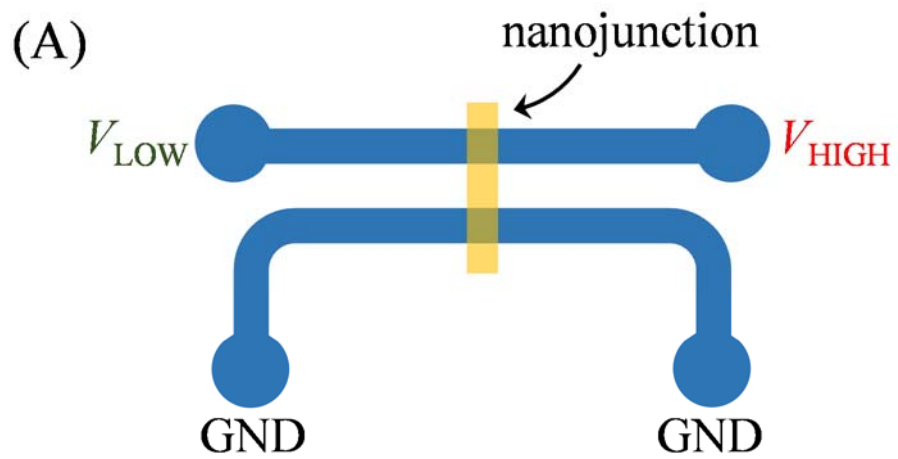


Figure 3.18 (A) Schematic of device with straight channel. The length of main channel is ~ 6 mm. (B) Microscopic view of the device with straight channel.

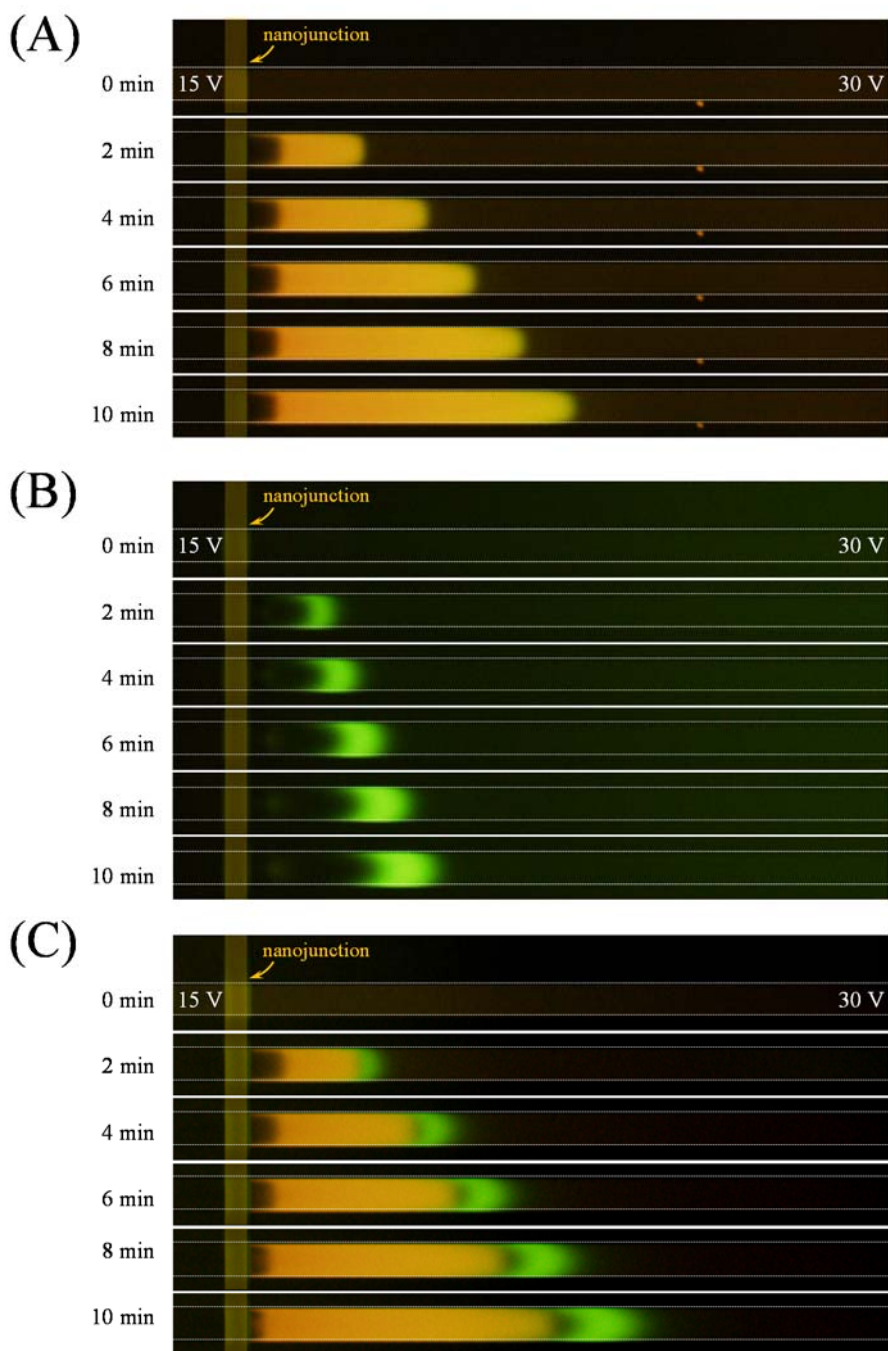


Figure 3.19 (A) Time-lapse images of selective preconcentration of (A) SRB, (B) Alexa 532 and (C) SRB and Alexa 532 together as a function of time. The location of each plug along time scale in (C) differs from that of single kind plug in (A) and (B).

zone and Alexa 532 propagates far from the depletion zone, the order of preconcentration plugs can be explained with a new model depending on electrophoretic mobility. In other words, when two different molecules are mixed and preconcentrated under ICP, molecules with different electrophoretic mobility compete with each other for satisfying local electroneutrality in order to preconcentrate at the original location which is the same location in a solution with single molecules. Over time, molecules with lower electrophoretic mobility wins molecules with higher electrophoretic mobility, and preoccupies the location near the depletion zone, expelling the molecules with higher electrophoretic mobility.

In order to investigate the new model more carefully, another dye named CoroNa Green which has neutral net electric charge was adopted. Figure 3.20(A) showed the normal preconcentration of CoroNa Green in the same condition with SRB and Alexa 532. As in SRB, this dye was also preconcentrated right next to the depletion zone and was stacked over time. Since the net charge of CoroNa Green is zero, it could be expected that SRB should lose in the competition and pushed toward the reservoir side with high voltage. In Figure 3.20(B), the experiment of mixed solution of SRB and CoroNa Green concurred with the expectation. The red image in Figure 3.20(B) only detected SRB. It can be shown in the image that CoroNa Green preoccupied the location right next to the depletion zone and pushed SRB to the reservoir side in order to satisfy the local electroneutrality.

In the light of the new model, the preconcentration of three different molecules as in Figure 3.12 can be analyzed. In the result, SRB, Alexa 532 and Alexa 488 were preconcentrated, and separated in this sequence. Considering the net charge of each dye, -1, -1, and -2, respectively, the order of Alexa 488 seems to makes sense. However, SRB and Alexa 532 were separated although their net charges are the same. When particles are polarized, the electrophoretic mobility under nonuniform electric field depends on the dipole moment of the particles.³⁴ However, the permittivities of this two dyes are smaller than that of water, which means that it is

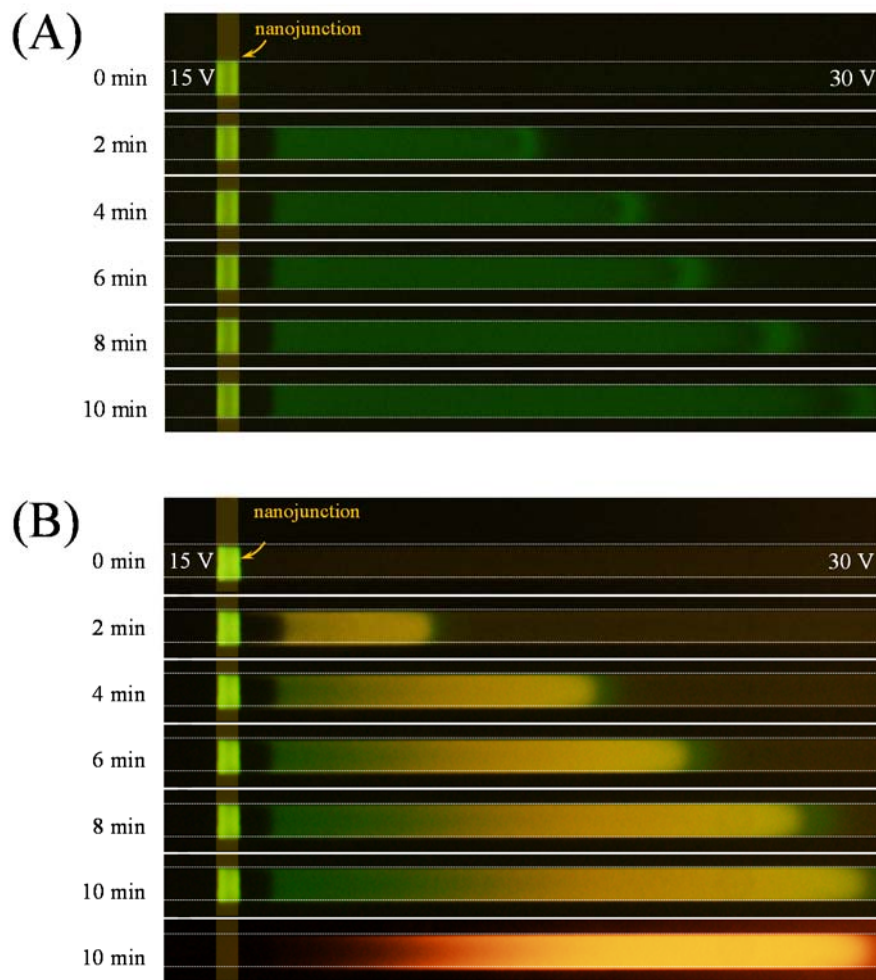


Figure 3.20 Time-lapse images of selective preconcentration of (A) CoroNa Green and (B) CoroNa Green and SRB together as a function of time. The location of each plug along time scale in (C) differs from that of single kind plug in (A) and (B).

not high enough to be effectively polarized. Therefore, the separation cannot be explained by induced charge interaction. In consideration of dielectrophoresis, dipole interaction between dye molecules can be also ignored since the size of molecules is $O(1)$ nm.³⁵ Thus, it might be caused by the nonlinear interaction between particle transport and ambient flow field.

Chapter 4

Conclusions

This thesis presented and characterized a multilayer micro/nanofluidic device for selective preconcentration. The operating principle of the device was based on the high electric field gradient induced by ICP phenomenon. In the main channel, two opposing electrophoretic force and electroosmotic drag force exerted on the charged molecules were balanced depending on the physicochemical properties of the molecules. Importantly, the repeated microchamber structure suppressed the undesirable instability of the ICP operation, pinning the location where the preconcentrated plug was formed. With this device, SRB and Alexa were simultaneously separated and preconcentrated at the separation resolution of 1.75. By introducing pneumatic microvalves, dispersion due to the high concentration gradient was prevented, and Alexa plugs preconcentrated at 100-fold was able to be isolated from the main channel without the loss of the ratio during the cyclic valve operations. After all, 30-fold of Alexa was able to be collected in the measurement window. RGB signals from the preconcentrated analytes were rigorously analyzed for quantitative and qualitative separation efficiency, while previous researches

relied only on the position tracking of the molecules. Three different dyes were also pre-concentrated and separated simultaneously. Through investigating the pre-concentration of each dye, additional mechanism for pre-concentration was revealed that interactions between different kinds of molecules affected the location of pre-concentrated plugs for satisfying local electroneutrality depending on their mobility. Given the importance of extracting selective pre-concentrated analytes, we expect that this mechanism and structure of the micro/nanofluidic device would be a powerful tool for lab on a chip applications.

Bibliography

1. Dolník, V.; Liu, S.; Jovanovich, S., Capillary electrophoresis on microchip. *Electrophoresis* **2000**, *21* (1), 41-54.
2. Jung, B.; Bharadwaj, R.; Santiago, J. G., On-chip millionfold sample stacking using transient isotachophoresis. *Analytical chemistry* **2006**, *78* (7), 2319-2327.
3. Rubinstein, I.; Shtilman, L., Voltage against current curves of cation exchange membranes. *Journal of the Chemical Society, Faraday Transactions 2: Molecular and Chemical Physics* **1979**, *75*, 231-246.
4. Kim, S. J.; Li, L. D.; Han, J., Amplified electrokinetic response by concentration polarization near nanofluidic channel. *Langmuir* **2009**, *25* (13), 7759-7765.
5. Song, H.; Wang, Y.; Garson, C.; Pant, K., Nafion-film-based micro–nanofluidic device for concurrent DNA preconcentration and separation in free solution. *Microfluidics and nanofluidics* **2014**, *17* (4), 693-699.
6. Kim, S. J.; Wang, Y.-C.; Lee, J. H.; Jang, H.; Han, J., Concentration polarization and nonlinear electrokinetic flow near a nanofluidic channel. *Physical review letters* **2007**, *99* (4), 044501.
7. Kim, S. J.; Ko, S. H.; Kwak, R.; Posner, J. D.; Kang, K. H.; Han, J., Multi-vortical flow inducing electrokinetic instability in ion concentration polarization layer. *Nanoscale* **2012**, *4* (23), 7406-7410.
8. Chen, C.-H.; Sarkar, A.; Song, Y.-A.; Miller, M. A.; Kim, S. J.; Griffith, L. G.; Lauffenburger, D. A.; Han, J., Enhancing protease activity assay in droplet-based

- microfluidics using a biomolecule concentrator. *Journal of the American Chemical Society* **2011**, *133* (27), 10368-10371.
9. Santiago, J. G., Thousandfold signal increase using field-amplified sample stacking for on-chip electrophoresis. *Electrophoresis* **2003**, *24*, 3476-3483.
 10. Kohlheyer, D.; Besselink, G. A.; Schlautmann, S.; Schasfoort, R. B., Free-flow zone electrophoresis and isoelectric focusing using a microfabricated glass device with ion permeable membranes. *Lab on a Chip* **2006**, *6* (3), 374-380.
 11. Cheow, L. F.; Sarkar, A.; Koltitz, S.; Lauffenburger, D.; Han, J., Detecting kinase activities from single cell lysate using concentration-enhanced mobility shift assay. *Analytical chemistry* **2014**, *86* (15), 7455-7462.
 12. Wang, Y.-C.; Han, J., Pre-binding dynamic range and sensitivity enhancement for immuno-sensors using nanofluidic preconcentrator. *Lab on a Chip* **2008**, *8* (3), 392-394.
 13. (a) Auroux, P.-A.; Iossifidis, D.; Reyes, D. R.; Manz, A., Micro total analysis systems. 2. Analytical standard operations and applications. *Analytical chemistry* **2002**, *74* (12), 2637-2652; (b) Reyes, D. R.; Iossifidis, D.; Auroux, P.-A.; Manz, A., Micro total analysis systems. 1. Introduction, theory, and technology. *Analytical chemistry* **2002**, *74* (12), 2623-2636.
 14. Lin, C.-C.; Hsu, J.-L.; Lee, G.-B., Sample preconcentration in microfluidic devices. *Microfluidics and nanofluidics* **2011**, *10* (3), 481-511.
 15. Kim, S. J.; Song, Y.-A.; Han, J., Nanofluidic concentration devices for biomolecules utilizing ion concentration polarization: theory, fabrication, and applications. *Chemical Society Reviews* **2010**, *39* (3), 912-922.
 16. Kim, P.; Kim, S. J.; Han, J.; Suh, K. Y., Stabilization of ion concentration polarization using a heterogeneous nanoporous junction. *Nano letters* **2009**, *10* (1), 16-23.
 17. (a) Ko, S. H.; Kim, S. J.; Cheow, L. F.; Li, L. D.; Kang, K. H.; Han, J., Massively parallel concentration device for multiplexed immunoassays. *Lab on a Chip* **2011**,

- II* (7), 1351-1358; (b) Green, Y.; Shloush, S.; Yossifon, G., Effect of geometry on concentration polarization in realistic heterogeneous permselective systems. *Physical Review E* **2014**, *89* (4), 043015; (c) Green, Y.; Yossifon, G., Effects of three-dimensional geometric field focusing on concentration polarization in a heterogeneous permselective system. *Physical Review E* **2014**, *89* (1), 013024; (d) Nam, S.; Cho, I.; Heo, J.; Lim, G.; Bazant, M. Z.; Moon, D. J.; Sung, G. Y.; Kim, S. J., Experimental Verification of Overlimiting Current by Surface Conduction and Electro-Osmotic Flow in Microchannels. *Physical review letters* **2015**, *114* (11), 114501.
18. Cho, I.; Sung, G. Y.; Kim, S. J., Overlimiting current through ion concentration polarization layer: hydrodynamic convection effects. *Nanoscale* **2014**, *6* (9), 4620-4626.
19. (a) Jia, M.; Kim, T., Multiphysics Simulation of Ion Concentration Polarization Induced by a Surface-Patterned Nanoporous Membrane in Single Channel Devices. *Analytical chemistry* **2014**, *86* (20), 10365-10372; (b) Jia, M.; Kim, T., Multiphysics Simulation of Ion Concentration Polarization Induced by Nanoporous Membranes in Dual Channel Devices. *Analytical chemistry* **2014**, *86* (15), 7360-7367.
20. (a) Unger, M. A.; Chou, H.-P.; Thorsen, T.; Scherer, A.; Quake, S. R., Monolithic microfabricated valves and pumps by multilayer soft lithography. *Science* **2000**, *288* (5463), 113-116; (b) Hong, J. W.; Studer, V.; Hang, G.; Anderson, W. F.; Quake, S. R., A nanoliter-scale nucleic acid processor with parallel architecture. *Nature biotechnology* **2004**, *22* (4), 435-439.
21. (a) Russel, W. B.; Saville, D. A.; Schowalter, W. R., *Colloidal dispersions*. Cambridge university press: 1992; (b) Schoch, R. B.; Han, J.; Renaud, P., Transport phenomena in nanofluidics. *Reviews of Modern Physics* **2008**, *80* (3), 839.
22. (a) Rubinstein, I.; Zaltzman, B., Electro-osmotically induced convection at a

- permselective membrane. *Physical Review E* **2000**, 62 (2), 2238; (b) Dydek, E. V.; Zaltzman, B.; Rubinstein, I.; Deng, D.; Mani, A.; Bazant, M. Z., Overlimiting current in a microchannel. *Physical review letters* **2011**, 107 (11), 118301.
23. Kim, S. J.; Ko, S. H.; Kang, K. H.; Han, J., Direct seawater desalination by ion concentration polarization. *Nature Nanotechnology* **2010**, 5 (4), 297-301.
24. Levich, V. G.; Technica, S., *Physicochemical hydrodynamics*. Prentice-hall Englewood Cliffs, NJ: 1962; Vol. 689.
25. Wang, Y.-C.; Stevens, A. L.; Han, J., Million-fold preconcentration of proteins and peptides by nanofluidic filter. *Analytical chemistry* **2005**, 77 (14), 4293-4299.
26. Lee, S.-H.; Lee, H.; Jin, T.; Park, S.; Yoon, B. J.; Sung, G. Y.; Kim, K.-B.; Kim, S. J., Sub-10 nm transparent all-around-gated ambipolar ionic field effect transistor. *Nanoscale* **2015**, 7 (3), 936-946.
27. Masliyah, J. H.; Bhattacharjee, S., *Electrokinetic and colloid transport phenomena*. John Wiley & Sons: 2006.
28. Kirby, B. J.; Hasselbrink, E. F., Zeta potential of microfluidic substrates: 2. Data for polymers. *Electrophoresis* **2004**, 25 (2), 203-213.
29. Lee, J. H.; Cosgrove, B. D.; Lauffenburger, D. A.; Han, J., Microfluidic concentration-enhanced cellular kinase activity assay. *Journal of the American Chemical Society* **2009**, 131 (30), 10340-10341.
30. Giddings, J. C., *Unified Separation Science* John Wiley & Sons. *New York* **1991**, 189.
31. Cheow, L. F.; Han, J., Continuous signal enhancement for sensitive aptamer affinity probe electrophoresis assay using electrokinetic concentration. *Analytical chemistry* **2011**, 83 (18), 7086-7093.
32. (a) Happel, J.; Brenner, H., *Low Reynolds number hydrodynamics - with special applications to particulate media*. **1983**; (b) Sangae, K.; Seppo, J. K., *Microhydrodynamics: Principles and Selected Applications*. In *Dover Publications*, 2013.

33. Druzgalski, C.; Andersen, M.; Mani, A., Direct numerical simulation of electroconvective instability and hydrodynamic chaos near an ion-selective surface. *Physics of Fluids (1994-present)* **2013**, *25* (11), 110804.
34. Squires, T. M.; Bazant, M. Z., Induced-charge electro-osmosis. *Journal of Fluid Mechanics* **2004**, *509*, 217-252.
35. (a) Jones, T. B.; Jones, T. B., *Electromechanics of particles*. Cambridge University Press: 2005; (b) Yoon, B. J., Electrophoretic motion of spherical particles with a nonuniform charge distribution. *Journal of colloid and interface science* **1991**, *142* (2), 575-581.

국문 초록

이온 분극 현상을 이용하여 물리화학적 성질이 다른 전하를 띤 입자를 선택적 분리 및 농축, 압출하는 다중층 마이크로/나노수력학 장치를 제시하였다. 입자에 대한 전기삼투 마찰 힘과 전기 영동 힘의 균형을 이용하여 sulforhodamine B와 Alexa Fluor 488 형광물질이 섞인 샘플을 높은 농도로 선택적으로 농축하였다. 반복적으로 연결된 마이크로챔버 구조의 마이크로채널은 형광입자를 원하는 위치로의 농축을 가능하게 하였다. 농축된 물질의 칩(chip) 상의 혹은 칩 외부에서의 연속적인 사용을 위하여, 마이크로 공압밸브가 결합되었고, 주기적인 밸브 작동을 통하여 원하는 입자만 선택적으로 압출할 수 있었다. 이러한 통합 시스템을 이용하여 sulforhodamine B가 섞인 수용액으로부터 Alexa Fluor 488이 압출되었고, 1.75의 분리 분해능과 30배의 농축비를 달성하였다. 또한 ICP 현상으로 일어나는 농축 매커니즘을 탐구하여 모빌리티에 따른 분자간 부분적 전기중성을 만족하고자하는 상호작용이 농축 플러그의 위치에 영향을 미친다는 것을 밝혀내었다. 본 장치는 랩온어칩(Lab on a chip)의 응용에 있어 향후 중요한 요소로서 역할을 할 것이라 예상된다.

주요어 : 선택적 농축, 이온선택성 투과막, 이온분극현상, 마이크로 공압 밸브, 나노전기수력학

학번 : 2014-21644